A Dissertation

entitled

Antimony Chalcogenide: Promising Material for Photovoltaics

by

Suman Rijal

Submitted to the Graduate Faculty as partial fulfillment of the requirements for the

Doctor of Philosophy Degree in Physics

_____

Dr. Yanfa Yan, Committee Chair

_____

Dr. Randy J. Ellingson, Committee Member

_____

Dr. Nikolas J. Podraza, Committee Member

_____

Dr. Richard Irving, Committee Member

_____

Dr. Ahalapitiya H. Jayatissa, Committee Member

_____

Dr. Scott C. Molitor, Acting Dean
College of Graduate Studies

The University of Toledo
August 2022

An Abstract of

Antimony Chalcogenide: Promising Material for Photovoltaics

by

Suman Rijal

Submitted to the Graduate Faculty as partial fulfillment of the requirements for the Doctor of Philosophy Degree in Physics

The University of Toledo

August 2022

This thesis presents the work performed on antimony chalcogenide i. e., antimony selenide (Sb_2Se_3) and antimony seleno-sulfide ($Sb_2(S, Se)_3$) as promising materials for photovoltaics. In this work, Sb_2Se_3 is deposited by using the closed space sublimation (CSS) method and characterized by using energy-dispersive X-ray spectroscopy (EDX), X-ray diffraction (XRD), scanning electron microscopy (SEM), a UVvis-NIR spectrophotometer (Perkin Elmer Lambda 1050) in the range of 300 to 2000nm., atomic molecular force (AFM), current atomic molecular force (c-AFM), and kelvin probe force microscopy (KPFM). The work is mainly focused on the fabrication and characterization of the absorber layer to optimize the performance of the solar cell.

At first, Sb_2Se_3 film grown using the CSS method is investigated, along with the effects of the selenization temperature on the structural and morphological properties of the absorber layer and photovoltaic performance of the corresponding cell. It is found that proper selenization temperature help to achieve Sb_2Se_3 films with large grains, uniform morphology, high crystallinity, desired crystal orientations, and increased carrier density. After optimizing the selenization temperature, we obtain a power conversion efficiency of 6.43%.

Sb_2Se_3 has a one-dimensional anisotropic crystal structure, which means if it is grown in a vertical direction i.e. (hkl) l≠0 (preferred orientation) there will be efficient transport of photogenerated carriers. An extensive study on the optimization of the seed layer condition is performed to orient the gain in the preferred direction. Controlling the grain orientation and compactness of the absorber layer we increase our baseline efficiency from 6.4% to 7.47%. After controlling the absorber orientation, we work on the post-annealing treatment of the absorber layer in ambient air. Annealing in ambient air further passivates the Sb_2Se_3 absorber and reduces the densities of the defects. After optimization of annealing temperature, our Sb_2Se_3 delivers the photo conversion efficiency (PCE) of 8.5%.

In our second approach, the solution processing of the antimony seleno sulfide, $Sb_2(S, Se)_3$, in solar cells is investigated. The hydrothermal method is used to fabricate the absorber layer as this method helps to improve the film quality, and homogeneity and reduce the production cost. Here, the effects of the annealing temperature on the morphological and structural properties of the $Sb_2(S, Se)_3$ films are studied. It is found that a proper annealing temperature leads to a high-quality $Sb_2(S, Se)_3$ film with large crystal grains, proper stoichiometry, and high crystallinity. After optimizing the process, we obtain $Sb_2(S, Se)_3$ solar cells with an improved power conversion efficiency from 2.04 to 8.48%.

I would like to dedicate my dissertation to my wife Sujana Pathak, my parents, and my family. This accomplishment wouldn't have been possible without their continuous love, support, and encouragement.

Acknowledgements

First and foremost, I would like to express my sincere gratitude to my advisor, Dr. Yanfa Yan, for his continuous guidance, support, and expert ideas which helped me to get good results during my research. I would also like to thank the dissertation committee members, Dr. Randy J. Ellingson, Dr. Nikolas Podraza, Dr. Richard Irving, and Dr. Ahalapitiya H. Jayatissa, for their insightful questions and comments, inspiration, suggestions, and encouragement.

Additionally, I would like to express my sincere appreciation for Dr. Zhaoning Song for his continuous unconditional help and support. I would also like to thank all our group members. I would like to thank Dr. Dengbing Li, Dr. Michael Heben, Dr. Adam Phillips, Dr. Ebin Bastola, and all my other friends working in R1 for their useful discussions, valuable opinions, and great research support. Also, I would like to thank all the faculty, staff, and fellow members of the Department of Physics and Astronomy.

Finally, I want to acknowledge my parents, wife, sister, brother, and other family members for their constant support and encouragement in my tough time. Special thanks to my wife, Sujana Pathak, who was always there for the happiest and darkest of times. Also, I want to thank everyone who directly or indirectly helped me on this journey.

Table of Contents

List of Tables

List of Figures

List of Abbreviations

AC .....Alternating Current
AM1.5G .....Air Mass 1.5 Global Standardized Solar Irradiance Spectrum
AFM.....Atomic Force Microscopy
AZO .....Aluminum Doped Zinc Oxide

CB .....Conduction Band
CBD .....Chemical Bath Deposition
CIGS .....Copper Indium Gallium Sulfide/Selenide
C-AFM.....Conductive Atomic Force Microscopy
CSS .....Closed Space Sublimation
CV.....Capacitance Voltage

DC.....Direct Current
DFT.....Density Function Theory
DI .....Deionized

ETL .....Hole Transport Layer
EDS or EDX .....X-ray Energy Dispersive Spectroscopy
EQE.....External Quantum Efficiency

FTO.....Fluorine Doped Tin Oxide
FE-SEM .....Field Emission Scanning Electron Microscopy
FF .....Fill Factor

HTL.....Hole Transport Layer

IR.....Infrared

J-V.....Current Density Voltage

KPFM.....Kelvin Probe Force Microscopy

PCE .....Power Conversion Efficiency
PV .....Photovoltaic

RF.....Radio Frequency
RTE.....Rapid Thermal Evaporation

SEM .....Scanning Electron Microscopy
SRH.....Shockley-Read Hall

TAS.....Temperature-dependent Admittance Spectroscopy
TC .....Texture Coefficient
TCO.....Transparent Conducting Oxide
TRPL.....Time Resolved Photoluminescence

UV-VIS-NIR.....Ultraviolet-Visible-Near Infrared

VB.....Valance Band
VTD .....Vapor Transport Deposit

XRD .....X-ray Diffraction

List of Symbols

α .....Absorption coefficient
η .....Device efficiency
θ.....Angle
Ω.....Ohm
μ .....Micron
λ.....Photon wavelength
E_a.....Defect activation energy
E_t .....Energy distribution
E_g.....Band gap
F .....Fill factor
I .....Current or intensity
J_0.....Saturation current density
J_d.....Dark current density
J_L .....Light current density
J_{SC}.....Short circuit current density
K.....Boltzmann's constant
$N_t(E(w))$ .....Density of States
n.....Diode ideality factor
q.....Electron charge
R_S .....Series resistance
R_{SH}.....Shunt resistance
S .....Incident photon flux density
T .....Temperature
T_{sou} .....Source temperature
T_{sub} .....Substrate temperature
T .....Temperature
V.....Applied voltage
V_{bi}.....Built-in potential
V_{OC}.....Open circuit voltage
w_o .....Characteristics transition frequency

Chapter 1

Introduction

1.1 Background and Motivation

The world population exceeded 7.8 billion as of March 2022 [1] and continued to increase the energy demand. A growing population is directly correlated with energy consumption, and we know that fossil fuel is one of the limited energy sources and has harmful effects on the environment. The greenhouse effect and global warming are the consequences of the fossil fuels byproducts like carbon dioxide ($CO_{2)}$, which is the primary source, and other gases like sulfur oxide (SO_x), methane (CH_4), carbon mono oxide (CO), nitrous oxide (N_2O), and other hydrocarbons are responsible for this effect.[2] The emissions of the carbons due to the combustion of the fossil fuel resulted in an imbalance in the earth's radiative energy flux, which ultimately warmed the earth's atmosphere and the oceans.

The U.S. Department of energy projected the energy consumption will be around ~ 27 TW by 2050 for a population of 9.4 billion.[3] As we know, fossil energy is limited and unsustainable; therefore, scientists and researchers are looking for other alternatives, such as renewable and low-carbon energy sources, to replace fossil fuels. Renewable energy like

solar, wind, hydropower, and thermal can be used to reverse global warming and reduce the greenhouse effect. Figure 1- 1: Share of global electricity generation by source.[4]Figure 1- 1 shows the share of global electricity generation by source.[4] All the clean and renewable electricity occupied 38% of the world's electricity in 2021, more than the proportion of coal at 36%.[4] In this total renewable energy, solar and wind energy occupied 10.3% of global electricity for the first time in 2021, rising from 9.3% in 2020 and twice as compared with 4.6 % in 2015 when the Paris climate agreement was signed.[4] Solar energy only contributed 3.1% of global electricity generation, making it the third-largest renewable electricity technology after hydropower and onshore wind after overtaking bioenergy in 2019.[4]

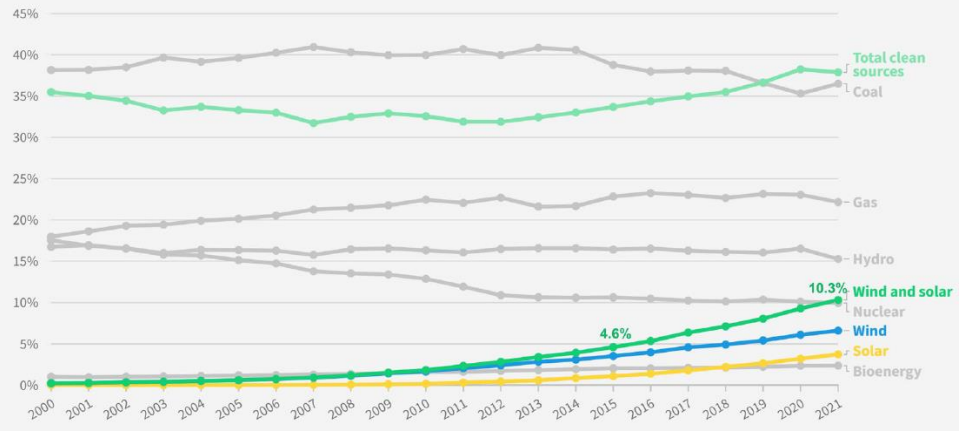

Figure 1- 1: Share of global electricity generation by source.[4]

Sunlight is the most abundant energy resource on the earth. Sun gives 15000 EJ of energy every day to the earth; however, human beings only require 1.3 EJ of energy for daily purposes.[5] This statistic shows solar energy could be one of the essential sources of energy that can fulfill the world's energy requirements. Solar energy can be harvested and converted into electricity using photovoltaic (PV) technologies.

1.2 Thin Film PV Technology

PV cells, also known as solar cells, convert sunlight (photons) to electricity by the PV effect. French scientist Edmond Becquerel discovered the PV effect in 1839 for the first time.[6, 7] Furthermore, for the first time, silicon solar cells were developed at Bell laboratories by Gerald Pearson in 1954.[7] Generally, solar cells are named after the semiconductor materials which are used as the light-absorbing layers. Silicon (Si) solar cells have a long history and are currently dominating the whole solar cell market.

Solar cells can be generally classified into three generations based on the time and materials used for the light-absorbing layer. First-generation solar cells are wafer-based and the most common solar cells available in the market. PV devices based on thin-film absorbers are second-generation solar cells. These thin-film absorbers are polycrystalline materials with a higher absorption coefficient which helps to reduce the production cost and energy payback time. The third-generation solar cells are emerging devices that can potentially overcome the Shockley-Queisser limit for a single-junction solar cell.

1.2.1 First Generation

The first generation of solar cells is the mature and one of the oldest commercially available photovoltaics technologies. Crystalline silicon (c-Si) is the absorber material for this generation of solar cells. The c-Si solar cell has a record efficiency of 26.7 %. [8] The advantage of using Si as an absorber layer is that they are one of the most abundant elements on the earth. However, these materials require high purification energy for processing. Also, Si has an indirect bandgap and poor light absorption properties, requiring a high thickness for the complete absorption of the solar spectrum.

1.2.2 Second Generation

The purpose of the second generation of solar cells is to reduce the cost of production by minimizing the material required for the complete absorption of the solar spectrum. This minimization of material during the fabrication of the second generation of solar cells would bring down the cost per watt under US$ 0.50/W (Figure 1- 3). Cadmium telluride (CdTe) and CIGS are low-cost thin-film PV technologies with power-conversion efficiencies (PCEs) of 22.1% and 22.6%, respectively. [9] Amorphous silicon (a-Si) is less efficient and has a PEC of 10.2% [10]; however, they still occupy some portion of the thin film market. In Figure 1- 2, we can see CdTe contributes much higher in comparison to a-Si and CIGS.[11]

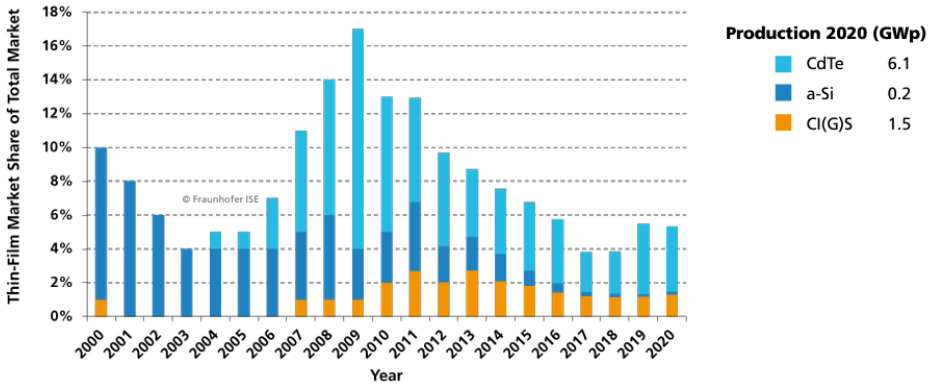

Figure 1- 2: Market share of thin-film technology in the years 2000-2020 for the main three thin-film technologies.[11]

1.2.3 Third Generation

The introduction of the third generation of solar cells is to achieve high-efficiency devices still using the second-generation thin-film technology. Since the third generation

is based on solution deposition, it has a low fabrication cost, and deposition can be done in a larger area. However, it has the problem of stability and commercialization. The third generation of solar cells includes dye-sensitized solar cells, perovskite, quantum dot sensitized solar cells, and organic solar cells.

The main goal of the third-generation solar cells is to decrease the cost of second-generation PVs from $1/W to $0.50/W, potentially to $0.20/W or better, by significantly increasing the efficiencies but maintaining the economic and environmental cost advantages of thin-film deposition techniques.[12] Figure 1- 3 describes how efficiency and cost are correlated. Here, we can see that when there is an efficiency improvement, the cost of energy per area gets reduced.

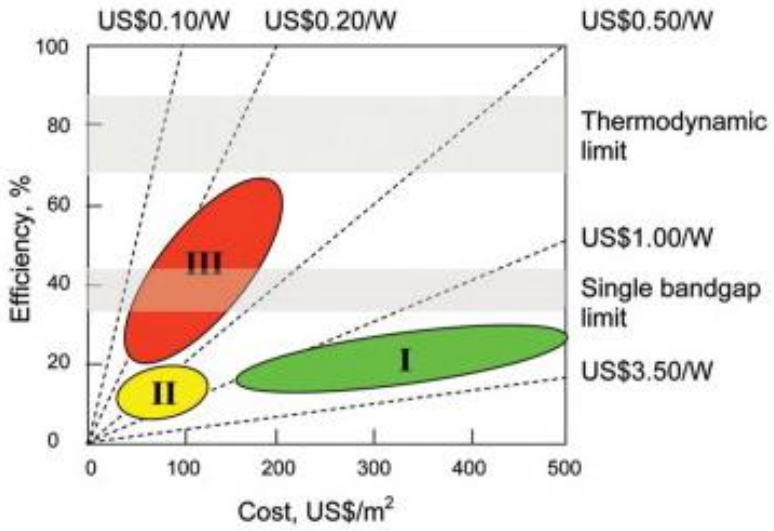

Figure 1- 3: Efficiency and cost projections for first, second, and third-generation PV technologies.[12](Tinted areas: 67-87% representing thermodynamic limit and 31-41% representing single bandgap limit).

Among the different solar cells in the third generation, perovskite has gotten remarkable attention from the PV community due to its high PCE of 25.5% [13] and excellent photovoltaic properties. Perovskite materials can absorb complete solar radiation because of their high absorption coefficient, which helps to reduce the material required during the fabrication process. Another important property of perovskite is its tunable bandgap. Its bandgap can be varied from 1.2 to 3 eV[14] by changing the composition, making this material the best candidate for single junction and multi-junction solar cells.

1.3 Motivation Beyond New Promising Absorber Materials

As discussed in section 1.2 the main aim of looking for new materials and technologies is to reduce production costs, make solar cells environmentally friendly, and make them more sustainable and stable. Whenever we consider any material as an absorber layer for PV application, it must satisfy some requirements like earth-abundant, low toxicity, and stability. If the materials satisfy all these requirements, then the materials are considered promising for PV applications.

Material properties are important things to be considered while looking for a new absorber material for PV. The band gap of the materials is an important property of the materials, which determines the two important parameters of the solar cells, i.e., open-circuit voltage (V_{OC}) and short circuit current density (J_{SC}). When the bandgap of the materials is too wide, then it cannot absorb enough photons from the solar spectrum, which ultimately reduces the photocurrent density of the devices. If the bandgap is too low, it can absorb most of the photons from the solar spectrum, resulting in a high photocurrent density but a low photovoltage of the device. Therefore, a material with the optimal band gap is

always in search of better solar cell applications. The Shockley-Queisser limit as a function of bandgap along with materials having optimal bandgap range (1.0-1.5 eV) is shown in Figure 1- 4[15]

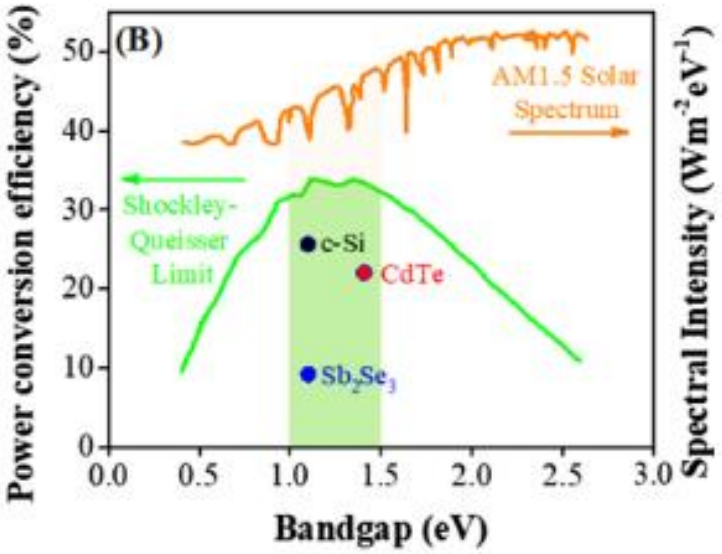

Figure 1- 4: Shockley-Queisser limit as a function of the band gap. Reprinted with permission [15]

1.4 Emerging PV Absorber Materials

The silicon solar cell and CdTe are considered matured, established, and commercialized solar cells. Over the years, different alternative cost-effective thin-film PV technologies have been developed, including Cu(In, Ga)(S, Se)$_2$(CIGSSe), CdTe, and lead halide perovskite solar cells. However, due to the scarcity of In, Ga, Te, and toxicity of Cd and Pb, new material is in search to get rid of those mentioned problems.[9] $Cu_2ZnSn(Se, S)_4$ was one of the promising materials with the properties of low-cost and nontoxic constituents; however, due to the complex chemistry and the carrier trapping defects, the

enhancement of the efficiency was not possible.[9] SnS, GeSe, Sb_2Se_3, and $Sb_2(S, Se)_3$ are simple binary emerging PV absorber materials where intense research is going on due to their characteristics like simple chemistry, low toxicity, and earth-abundant absorber. [9]

1.4.1 Antimony Chalcogenide

1.4.1.1 Antimony Selenide (Sb_2Se_3)

Sb_2Se_3 was first described in the 1950s [16], which occurs naturally in the mineral antimonselite. [17] Polycrystalline Sb_2Se_3 thin-film solar cells have recently gotten much attention from the PV community due to their properties like high absorption coefficient (10^5 cm^{-1}) and suitable bandgap (1-1.3 eV).[18] Moreover, due to its other properties like earth-abundant, low toxicity, and low-cost constituents (Sb and Se) this material could be one of the promising candidates to replace the CIGS and CdTe in coming years. Sb_2Se_3 is not listed as a highly toxic materials by American, European, or Chinese regulation authorities, nor in the lethal dose LD50 or lethal concentration LCt50 data.[15] The earth curst has Sb and Se in the amount of 0.2 and 0,05 ppm, respectively.[19] This material can be used for both configurations of solar cells, i.e., substrate and superstrate configurations. The schematic diagram of substrate and superstrate configuration of Sb_2Se_3 thin-film solar cells is shown in Figure 1- 6.

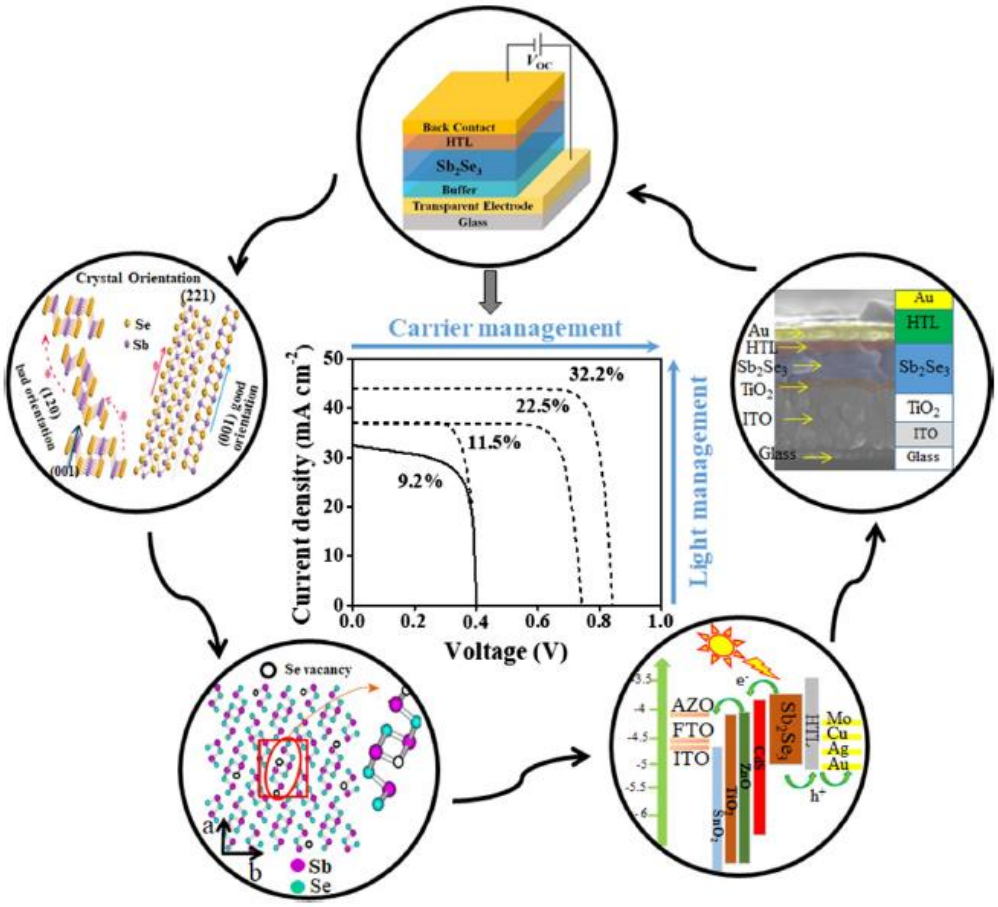

Figure 1- 5: Important features studies and future research areas of Sb_2Se_3-based thin-film solar cell. Reprinted with permission [15]

The figure starts with the schematic superstrate configuration of Sb_2Se_3 solar cells. When going to counterclockwise it shows the orientation of the ribbon in both good and bad orientation. Then, explains the defect control in the case of V_{se} after that the figure describe the different band alignment for different materials. Then, we can see the cross-sectional image of the complete device. In the middle of the figure, we can see the comparison between the absorption efficiency and collection efficiency of the incident light (light management) and photo-generated carriers (carrier management) respectively. [15]

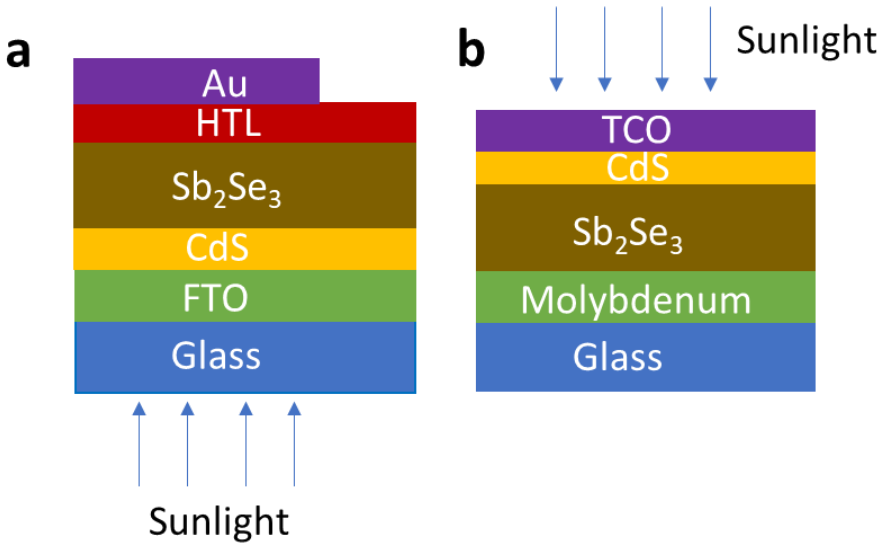

Figure 1- 6: Different configurations of Sb_2Se_3 solar cells: (a) superstrate and (b) substrate.

Sb_2Se_3 is a one-dimensional V-VI semiconductor material that has an orthorhombic *Pnma* crystal structure (Figure 1- 7).[20] The one-dimensional materials were considered to be unsuitable PV materials in the past because of their poor carrier mobility between the different atomic chains.[21]But, recent studies have shown that if the atomic chains are well controlled and perpendicular to the p-n junction interface in the solar cell, then the grain boundaries in these Q1D semiconductors can be intrinsically benign.[22] The Sb_2Se_3 is made up of an infinite chain of Sb_4Se_6 units where Sb-Se is bounded by the covalent bonds if they are stacked on the c-axis, whereas they are bounded by the weak van der Waals (vdW) force if they are aligned along a-axis and b-axis.[23] Sb_2Se_3 has an anisotropic crystal structure meaning carrier transport depends on the crystal orientations.[9, 24] When the nanoribbons are oriented on a or b-axis, then they are

bounded by the vdW force, due to which there will be a barrier for the transport of the photogenerated carriers. Whereas, when the ribbons are oriented vertically, i.e., c-axis, then there will be efficient transport of the photogenerated carriers which helps to improve the performance of the solar cell, and this orientation is the preferred orientation.[25]

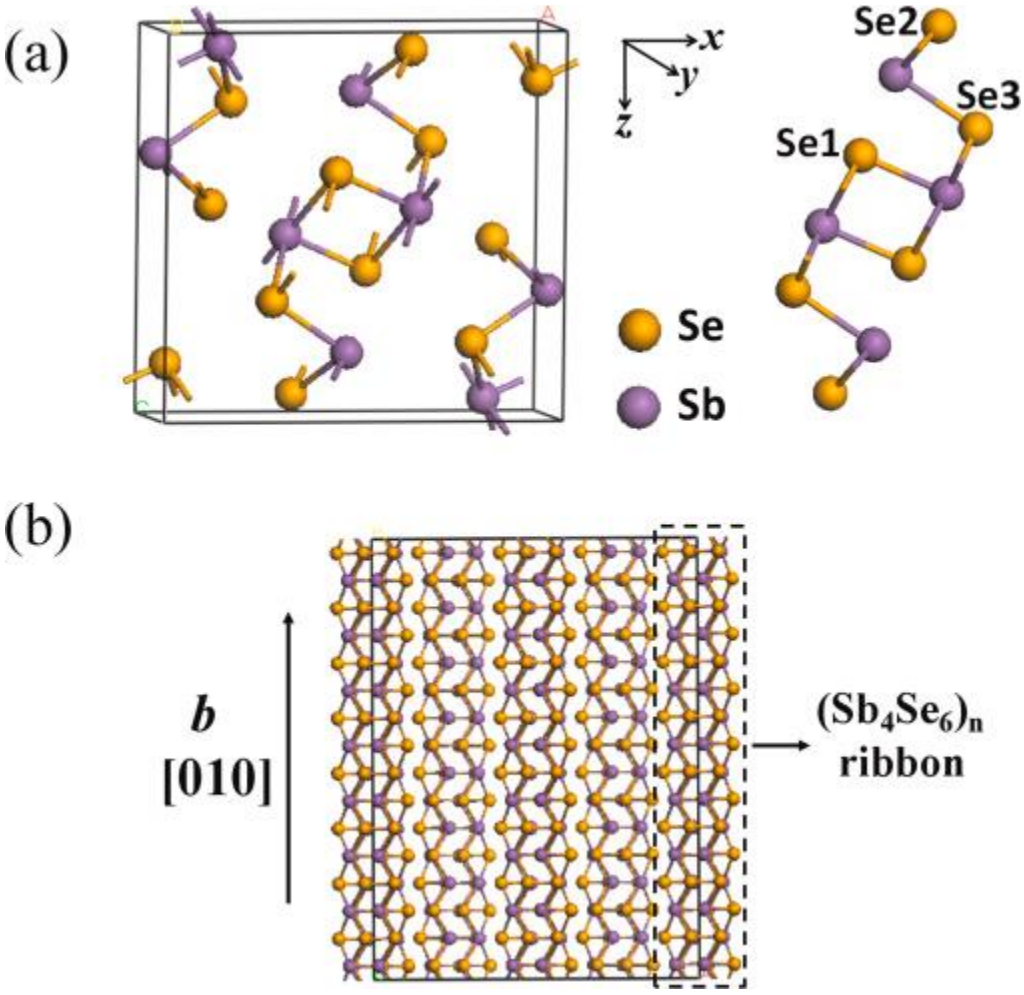

Figure 1- 7: (a) represents the orthorhombic unit cell of Sb_2Se_3 and right Sb_4Se_6 unit. (b) represents the cut parallel to the (010) direction. Reprinted with permission[20]

The several important properties of Sb_2Se_3 are summarized in Table 1- 1.

Table 1- 1: Physical properties of Sb_2Se_3. The label a indicates optical bandgap were calculated using density functional theory. Reprinted with permission[15]

Property of the Material	Symbol	Value
Lattice parameters (Å)	a	11.6330
	b	11.7800
	c	3.9850
Space group		*Pnma* 62
Density (g cm^{-3})	P	5.84
Melting point (K)	T_m	885
Bandgap (eV)	$E_{g,d}$ (direct)	1.17, 1.07[a] (300 K)
	$E_{g,i}$ (indirect)	1.03, 0.99[a] (300 K)
Absorption coefficient (cm^{-1})	A	$> 10^5$
Relative dielectric constant (ε_0)	ε_r	14.3–19.8
Exciton binding energy (eV)	E_{exc}	1.28
Minority-carrier lifetime (ns)	τ_e	60
Mobility ($cm^2 \cdot V^{-1} \cdot s^{-1}$)	μ_e	15
	μ_h	42
Diffusion length (μm)	$L_{e,c}$	1.7

First, the Sb_2Se_3 solar cell device was reported in 2009 with a PCE of 0.66%.[18] The record PCE increased from 2.1% in 2014[26] to 10.12% in 2022.[27] So, Sb_2Se_3 has a short history, but it has shown a promising learning curve. When we compare the record experimental PCE, i.e., 10.12% [27], and the maximum thermodynamic efficiency limit > 30%[28], we can say there is still plenty of room for improvement. Studies show that the

PV performance of the Sb_2Se_3 solar cells determines by the grains and intrinsic defects in the bulk and at the interfaces.[23, 29, 30]

In addition to the pure selenide Sb_2Se_3, sulfo-selenide $Sb_2(S, Se)_3$ also has gained attention from the PV community. Most of its properties resemble the Sb_2Se_3 and Sb_2S_3 possessing a one-dimensional crystal structure with a high absorption coefficient of > 10^5 cm^{-3}. Moreover, due to the identical crystal structure of the Sb_2Se_3 and Sb_2S_3 the bandgap of the $Sb_2(S, Se)_3$ can be tuned from 1.7 eV to 1.1 eV by changing the atomic ratio of Se/S.[31]

1.5 Dissertation Outline

This dissertation mainly focuses on the fabrication and characterization of antimony-based solar cells, i.e., Sb_2Se_3 and $Sb_2(S, Se)_3$ solar cells. This dissertation begins with an introduction and motivation in chapter 1.

Chapter 2 covers the various experimental methods for the fabrication of Sb_2Se_3 and $Sb_2(S, Se)_3$ solar cells. This is followed by the complete solar cell fabrication starting with the cleaning of a substrate to the grid deposition. In addition to the preparation methods, we will talk about the common material and device characterization techniques in this chapter.

Chapter 3 will focus on the optimization of selenization temperature on the performance of Sb_2Se_3 solar cells. The surface morphology, cross-section overview, and elemental composition are studied by using the SEM and EDS. Furthermore, we will discuss how the orientation of the grain changes with the selenization temperature, and XRD will be used to analyze the phase and the orientation of the grain. Furthermore,

capacitance-voltage (C-V) measurement carry out to find out the carrier concentration. Finally, the device is completed by depositing the transparent conducting oxide (TCO), followed by the deposition of silver (Ag) as a grid by thermal evaporation. After the optimization of selenization temperature, there is a significant improvement in the device performance from 1.85% to 6.43%.

Chapter 4 will discuss how the seed layer growing condition affects the orientation of the grain of the absorber layer. Also, we will discuss air annealing and its effects on the performance of solar cells. We will discuss in detail the characterization like SEM, EDS, XRD, temperature-dependent admittance spectroscopy, c-AFM, and KPFM to understand the surface morphology, elemental composition, grain orientation, absorber conductivity, and surface potential of the film. Furthermore, we will talk about the J-V and EQE measurements to discuss the performance of the solar cell. By orienting the seed layer in the preferred direction, we can improve our device's PCE to 7.47%, followed by the annealing in the air, which delivers a PCE of 8.5%.

Chapter 5 will discuss the fabrication and characterization of $Sb_2(S, Se)_3$ solar cells. We use SEM, and EDS to study the surface morphology and elemental composition. We also use XRD to find the phase and the orientation of the grain. We use temperature-dependent admittance spectroscopy to find the activation energy and density of defects. Further, we use the KPFM to study the surface potential of the film. Here, we study the effect of annealing temperature on the device performance. Finally, we will do J-V measurement and EQE measurements to find the performance of the solar cells. After proper optimization of the annealing temperature, we are able to get a PCE of 8.5%.

Finally, chapter 6 summarizes all the important results, discussion, and conclusion extracted from the previous chapter. Further, it discusses the probable future opportunities that can be applied to the device fabrication so that there will be an improvement in our baseline PCE of 8.5%.

Chapter 2

Experimental Techniques

2.1 Introduction

There are several deposition methods for the deposition of thin films. Generally, we can divide deposition techniques into groups, i.e., vacuum and solution-based methods. Common vacuum techniques used to fabricate thin films are physical vapor deposition (PVD) and chemical vapor deposition (CVD). The main difference between PVD and CVD is in the vapor that condenses in the substrate. In PVD, there is simply condensation of the vapor on the substrate, which is made of up atoms and molecules, whereas in CVD, there will be chemical reactions in the substrates, which result in a thin film.[32] Sputtering, evaporation, and electron beam method are some of the techniques that fall under the PVD methods. Atomic layer deposition (ALD) and plasma-enhanced chemical vapor deposition (PECVD) are CVD methods. Now, when we move toward the solution deposition methods, the general deposition methods are hydrothermal, sol-gel, hot-injection colloidal, Chemical bath deposition (CBD), and spin-coating.

Thin films grown by different deposition techniques can be characterized by using different instruments to study the structural, morphological, optical, and electronic

properties of the films. SEM, AFM, and EDS can check film morphology and elemental composition. Similarly, the phase, crystal structure, and orientation of the gain can be studied by using the XRD. Optical properties can be checked using UV-Vis-NIR spectrometer, photoluminescence, ellipsometry, and time-resolved photoluminescence (TRPL). Similarly, the electronic properties can be checked by using the C-V method and temperature-dependent admittance method.

In this chapter, I will discuss in detail how I fabricated the Sb_2Se_2 and $Sb_2(S, Se)_3$ thin-film solar cells. I will discuss the techniques that I used for the deposition of different layers of a solar cell. Also, I will include the instrument used during the characterization of the thin films.

2.2 Materials Preparation and Device Fabrication

2.1.1 Fabrication of Sb_2Se_3 Thin-Film Solar Cells

Sb_2Se_3 thin film can be deposited by different methods like CSS[9, 33], VTD[34], sputtering[35], evaporation[36], and hydrothermal[31]. The deposition technique affects the properties and quality of the thin film. Highly crystalline Sb_2Se_3 films are very helpful in reducing the bulk trap density and decreasing the non-radiative recombination loss.[33] Since CSS is widely used for the fabrication of efficient CdTe thin-film solar cells because of the scalability and efficient material utilization, we also decided to use the CSS method for the deposition of the absorber layer [33]. Figure 2- 1 shows the schematic diagram and

lab setting of the CSS system of our lab. The CSS system we are using in our lab is home-built.

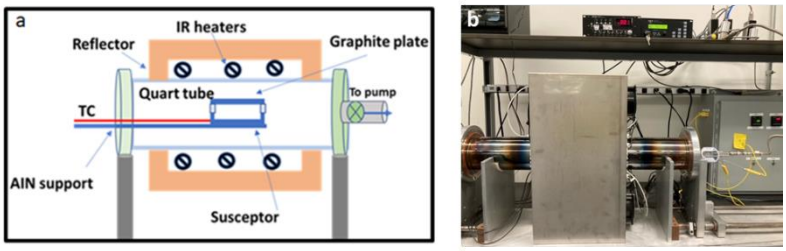

Figure 2- 1: Schematic diagram of CSS system and b) CSS setting in our lab.

The structure of the standard substrate configuration Sb_2Se_3 cell deposited on the soda-lime glass substrate is shown in Figure 2- 2.[9] The various steps that were involved during the fabrication of the complete solar cell are discussed in detail next.

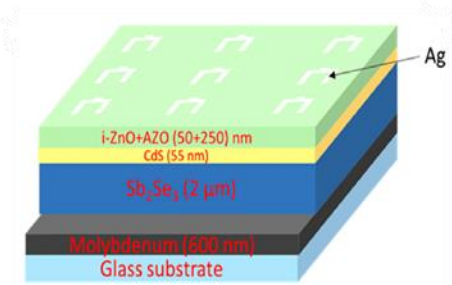

Figure 2- 2: Schematic diagram of Sb_2Se_3 complete solar cell.

I. Substrate cleaning: Glass substrates were subsequently cleaned by using an ultrasonic bath. Micro-90 detergent was used for cleaning purposes. Glasses were ultrasonically cleaned using deionized water (DI) for 30 minutes at a temperature of 150 ^{o}C. These glasses were rinsed 3 times with DI water. Finally, the substrates were cleaned with DI water and dried using nitrogen.

II. Back contact deposition: Molybdenum (Mo) was deposited on soda-lime glasses as a back contact during the fabrication of the solar cell. Mo layers were deposited by using a direct current (DC) magnetron sputtering system with a high purity Mo target (99%) from Kurt J. Lesker. There are certain advantages to using Mo as a back contact a) Mo is a good optical reflector that reflects the light to the absorber layers, b) Mo forms a low-resistivity ohmic contact to Sb_2Se_3, and the Mo doesn't degrade due to the deposition process of the absorber layer, c) Mo has high conductivity and is stable mechanically and chemically during Sb_2Se_3 growing.[37]We have to be very careful during the deposition of Mo. Mo deposited at high pressure has good adhesion to soda-lime glass; however, the conductivity is poor due to the high roughness of the film. Whereas at lower pressure, there is good conductivity, but adhesion is poor. So, to optimize the condition, we used a two steps process. First, we deposited Mo under high pressure at 15 mT for 15 minutes, then the rest of the deposition was done at 4 mT so that there is good adhesion as well as good conductivity. We used Argon (Ar) gas during the deposition, and the thickness of Mo is 600 nm. We used 150 W power for the deposition.

III. Preparation of thin film: This part "preparation of source material" is extracted from the supporting information which has been published in Rijal et al., 2021[9]. Printed with permission, from Rijal, S., et al., *Influence of Post-selenization Temperature on the Performance of Substrate-Type Sb_2Se_3 Solar Cells.* ACS Applied Energy Materials, 2021. **4**(5): p. 4313-4318.

For the Sb_2Se_3 deposition, we first prepared a source plate by depositing a several microns thick Sb_2Se_3 film on a graphite plate at a base pressure of 5 mTorr for half an hour using pure Sb_2Se_3 powders (99.99%, Jiangxi Ketai Advanced Materials Co. Ltd.). The source (T_{sou}) and substrate (T_{sub}) temperatures were kept at 560 and 350 ^oC, respectively. The distance between the source and substrate was ~6 mm. The main purpose of making a source plate is to control the sublimation rate. Then, a 200 nm Sb_2Se_3 seed layer was deposited on Mo-coated glass substrates using the source plate, with T_{sou} and T_{sub} at 500 and 315 ^oC, respectively, following our previous publication.[33] After that, a bulk Sb_2Se_3 absorber layer was deposited using the source plate with T_{sou} and T_{sub} at 480 and 400 ^oC, respectively. During the deposition, a pure nitrogen flow was supplied at a flow rate of 400 sccm to maintain a base pressure of 231 mTorr. The thickness of the absorber layers was ~2 μm for a 6 min deposition run

IV. Selenization: Selenization is the process in which the absorber layer is annealed in the Se atmosphere. The main aim of dong selenization is to compensate for the Se loss during the absorber layer deposition. The obtained absorber layers were selenized at temperatures from 350 to 450 ^oC (Figure 2- 4) in Ar at a base pressure of 10 Torr with 100 mg selenium for 30 min to promote the recrystallization of Sb_2Se_3. The schematic diagram of the selenization is shown in Figure 2- 3.

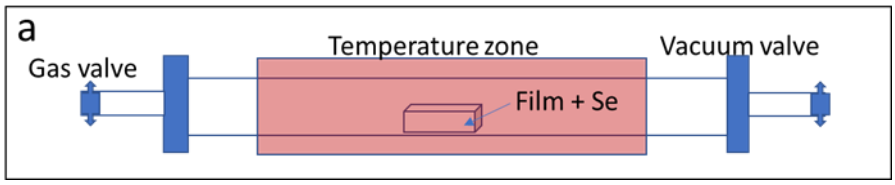

Figure 2- 3: Schematic diagram of Selenization furnace.

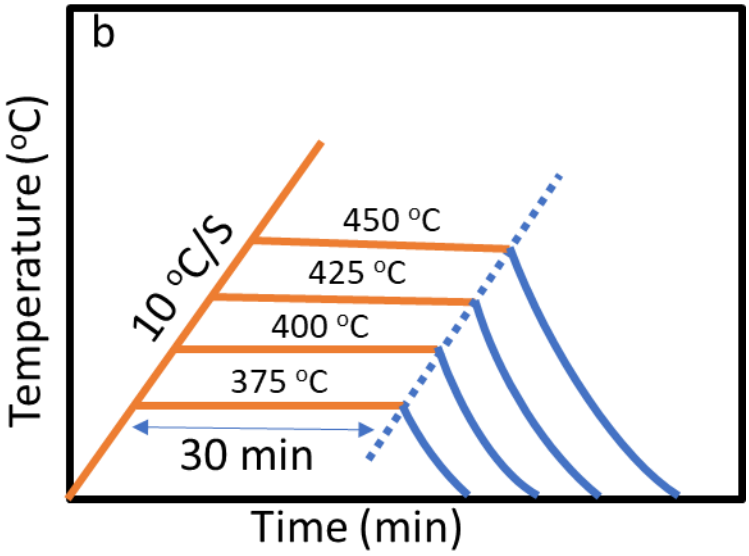

Figure 2- 4: Selenization temperature profile.

V. Window layer deposition: Solar cell is made up of a p-n junction. In our case, Sb_2Se_3 is a p-type material, so we deposit the CdS layer as an n-type material on the top of the absorber. We deposit 50 nm of CdS on the absorber layer by the CBD method. Cadmium acetate, ammonium acetate, thiourea, and ammonium hydroxide are used as a chemical. We dissolved 17.28 grams of ammonium acetate in 100 ml of DI water in a separate container. Similarly, we dissolved 12.74 and 7.88 grams of thiourea and cadmium acetate in 100 ml of DI water in a separate

container. After that for each batch of deposition of CdS, we used 10 ml of cadmium acetate, ammonium acetate, thiourea from the previously made solution, and 20 ml of ammonium hydroxide solution in 450 ml of DI water.

During the deposition process, cadmium acetate acts as a Cd^{2+} source, the source of S^{2-} is thiourea, and ammonium hydroxide acts as a catalyst. First, DI water was heated to 63^{o}C in a water bath (Figure 2- 5) and when the temperature is stable, we dipped the samples into the water. Magnetic stir was used to make the water temperature uniform and to dissolve the chemical. After that chemical were added to the DI water and waited for 10 minutes. The samples were taken out, rinsed with DI water, and dried with nitrogen. The thickness of the CdS is ~55 nm.

Figure 2- 5: Setup for Cadmium sulfide deposition.

VI. TCO layer deposition: A front contact with high resistive intrinsic zinc oxide (i-ZnO) and aluminum-doped zinc oxide (ZnO:Al) was deposited by radio frequency (RF) sputtering. 50 nm of i-ZnO was first deposited at a power of 90

W and a pressure of 4 mT whereas ZnO:Al was deposited on the top of ZnO:Al at power and pressure of 150 W and 2 mT, respectively. This bilayer was deposited without breaking the vacuum. The deposition was done for 50 min and 90 min for i-ZnO and ZnO:Al, respectively.

VII. Grid deposition: Lastly, the device was completed by depositing 200 nm of Ag via a thermal evaporator. Finally, the device was mechanically scribed into the individual cells with an active area of 0.2cm^2.

2.2.1 Fabrication of $Sb_2(S,Se)_3$ Thin-Film Solar Cells

The $Sb_2(S, Se)_3$ thin films were deposited onto the CdS coated FTO glass substrates by a hydrothermal method. The CdS layer was first deposited by a CBD approach, following the previously reported method.[38] Afterward, the obtained CdS film was annealed in ambient air at 400 ^oC for 10 min. For the $Sb_2(S, Se)_3$ deposition, potassium antimony tartrate ($C_8H_4K_2O_{12}Sb_2 \cdot 3H_2O$), sodium thiosulfate pentahydrate ($Na_2S_2O_3 \cdot 5H_2O$), and selenourea (CH_4N_2Se) were used as Sb, S, and Se sources, respectively. 20 mM of $C_8H_4K_2O_{12}Sb_2. \cdot 3H_2O$, 40 mM of $Na_2S_2O_3 \cdot 5H_2O$, and 35 mg of CH_4N_2Se were mixed in 50 ml of DI water.[39] The mixed solution was stirred until it turned clear and homogenous faint yellowish. Then, the solution was transferred into the cleaned inner Teflon tank of an autoclave. During the synthesis, the substrate was placed in such a way that the CdS layer faced downward. Finally, the tight autoclave with the solution was kept in an oven heated at 130 ^oC for 3 h.

.

The autoclave was taken out of the oven and allowed to cool to room temperature. Then, the films were taken out from the autoclave and dried by blowing N_2 gas. Afterward, the films were loaded inside the tube furnace on the graphite plate and the tube was vacuumed till we get the pressure of 3 mT. Then, we annealed the samples in two-step processes. First, we heated the graphite plate, which holds the samples, at 100 ^oC using the IR heater from the top and bottom side for one minute. This first step of heating is done to remove the water or any other solvent remaining on the film. Then finally, we fill the tube with 10 T of N_2 gas and heated the films at different temperatures i.e 300, 350, and 400 ^oC for 10 minutes. After 10 minutes of heating, the films were allowed to cool down to room temperature.

Finally, we prepared a device in a superstrate configuration: FTO/CdS/Sb_2(S, Se)$_3$/Spiro-OMeTAD/Au (Figure 2- 7). We used Tec-12D FTO glass substrate from Pilkington North America Inc. After that, a spiro-OMeTAD film was spin-coated on the Sb_2(S, Se)$_3$ film at a speed of 2500 rpm for 30 sec and was left overnight to get oxidized. Finally, Au was deposited on the top of Spiro as a back contact electrode using a thermal evaporator under a pressure of 5 x 10^{-6} Torr, where a mask of 0.08 cm^2 was used. The deposition process of Sb_2(S,Se)$_3$ solar cells is shown in Figure 2- 6.

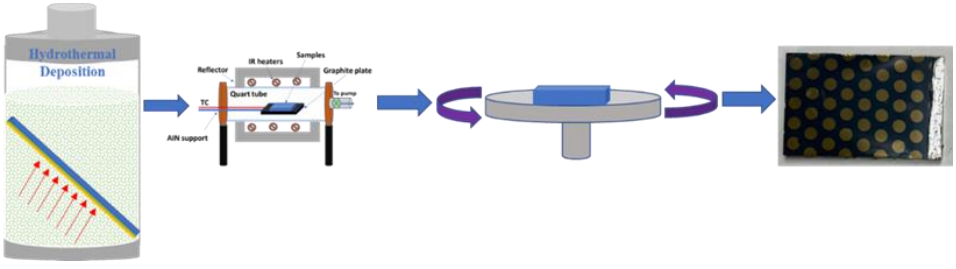

Figure 2- 6: Fabrication process of Sb_2(S,Se)$_3$ solar cells.

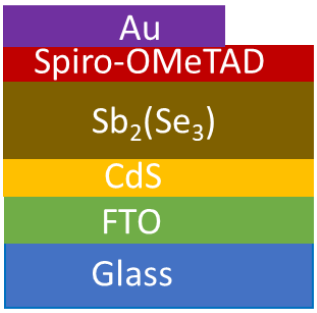

Figure 2- 7: Structure of $Sb_2(S,Se)_3$ solar cell in the superstrate configuration.

2.3 Materials and Device Characterization

2.3.1 Fabrication of $Sb_2(S, Se)_3$ Solar Cells

The thickness of the thin films was measured by the profilometer (Veeco Dektak 150). X-ray diffractometer (Rigaku Ultima III) with Cu Kα radiation was used to study the crystal structure and orientation of the films. The morphology and microscopic structure of the films were determined by using the high-resolution field emission SEM (FE-SEM Hitachi S-4800). The elemental composition of the films was determined by the EDS which is integrated with the SEM. The sheet resistance of the films was studied by the four-point probe (Pro4, Lucas Labs). The optical absorption spectra were measured by using a UV-vis-NIR spectrophotometer (Perkin Elmer Lambda 1050) in the range of 300 to 2000nm through transmission. Capacitance voltage (C-V) measurements were performed using the Solartron Modulab potentiostat equipped with a frequency response analyzer (Ametek Inc.). TAS and J-V-T measurements were done by using Modulab potentiostat equipped with a frequency response analyzer (Ametek Inc.). KPFM was performed on a home-built

KPFM system based on D3100 atomic force microscope (AFM) and C-AFM was performed on a Bruker Dimension Icons system

2.3.2 Device Characterization Methods

The performance of the thin-film solar cells was analyzed by the current density-voltage (J-V) measurement using Keithley 2440 source meter and a LED solar simulator (Newport) configured to simulate the AM1.5 illumination. J-V curves help determine quantitative and qualitative information associated with the overall solar cells.

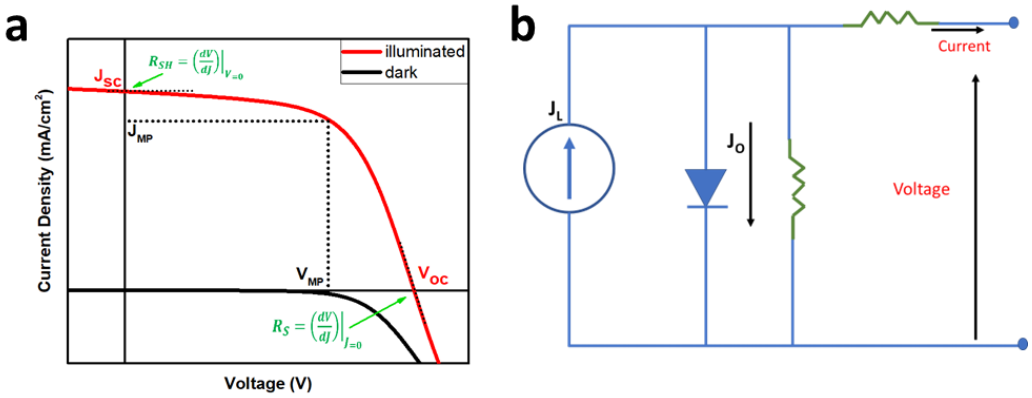

Figure 2- 8: (a) J-V curves and (b) the equivalent circuit of a general photovoltaic device.

The illuminated and the dark J-V curves of a photovoltaic device and the equivalent electric circuit diagram are shown in Figure 2- 8. Under the illumination, the J-V curve is given by :[40]

$$J = J_L - J_d = J_L - J_o\left(exp\left(\frac{q(V+JR_S)}{nkT}\right)\right) - \frac{V+JR_S}{R_{SH}} \quad \text{..... (2.1)}$$

Where J_L is the light-generated current density, J_d is the dark current, J_o is the dark leakage (or saturation current), V is the applied voltage, q is the electron charge, n is the

diode ideality factor, k is the Boltzman's constant, and T is the absolute temperature in Kelvins, R_S and R_{SH} are the series and shunt resistance.

There are mainly three different parameters that determine the performance of the solar cell. Those parameters are shorts circuit current (J_{SC}), open-circuit voltage (V_{OC}), and fill factor (FF). The J_{SC} is the maximum current that can flow through the solar cell when the applied voltage is zero. Light generates and collects the carriers in the device, which causes J_{SC}. J_{SC} depends on several factors. Some of them are the number of photons incident, the spectrum of the incident light, and the optical properties of the device.

The other parameter is V_{OC} which is the maximum voltage across the terminal of the solar cell under open-circuit conditions, which means when $_J$ is zero. V_{OC} generally depends on the bandgap of the absorber material, bulk, interface recombination, and defects at the interface. Neglecting the parasitic resistances (R_S and R_{SH}) and setting Equation 2.1 to zero, we can calculate the V_{OC} by

$$V_{OC} = \frac{nkT}{q} \ln \left(\frac{J_L}{J_O} + 1\right) \text{----------(2.2)}$$

From Equation 2.2 as the light current can be controlled, V_{OC} mostly depends upon the saturation current, which is determined by the amount of recombination in the solar cells. This means V_{OC} determines the overall quality of the thin film and the density of non-radiative recombination centers.

FF is another important parameter which is the ratio of the maximum power output of the solar cell to the product of J_{SC} and V_{OC} given by,

$$FF = \frac{J_{MP}V_{MP}}{J_{SC}V_{OC}} \text{……..…...……..(2.3)}$$

Where J_{MP} and V_{MP} are the current density and voltage values, respectively, at the maximum power point, as shown in Figure 2- 8. Generally, FF depends on the parasitic resistance, i.e., shunt and series resistance; also, it depends on the bulk and interface defect densities.

Lastly, the most important parameter that determines the performance of the solar cell is the power conversion efficiency (PCE). PCE is defined as the ratio of maximum electrical power output to the power of incident light, which can be mathematically written as:

$$\eta = \frac{V_{OC} J_{SC} FF}{P_{in}} \text{----------(2.4)}$$

Where P_{in} is the input power of illumination either from the sun or a solar simulator.

Along with the J-V measurement, external quantum efficiency (EQE) is another important means to find the J_{SC}. EQE is defined as the ratio of the number of carriers collected by the solar cell to the number of photons incident to the solar cell. Generally, the EQE is given as a function of wavelength. If all the given photons of a certain wavelength are absorbed, and the same number of carriers is generated, then we call the quantum efficiency at a particular wavelength unity. But, due to the presence of many optical and electrical losses we can never get the quantum efficiency to 100%. Ideally, the J_{SC} that we get from the J-V measurement should be equal to the J_{SC} that we get from the EQE measurement. During the EQE measurement, J_{SC} is measured as the integration of all the measured EQE over the wavelength range. Thus, the total current from QE is calculated by using the following equation:[40]

$$J_{SC} = q \int_{\lambda} F(\lambda) QE(\lambda) d\lambda \text{----------(2.5)}$$

Where $F(\lambda)$ is the photon flux density per unit wavelength.

The optical loss is mostly caused by the reflection of the incident light from the front surface. On the other hand, optical losses could also happen due to the incomplete absorption of the incident light due to the thickness of the absorber layer, window layer, and TCO layer. Figure 2- 9 illustrates the EQE spectrum of complete Sb_2Se_3 solar cell.[41]

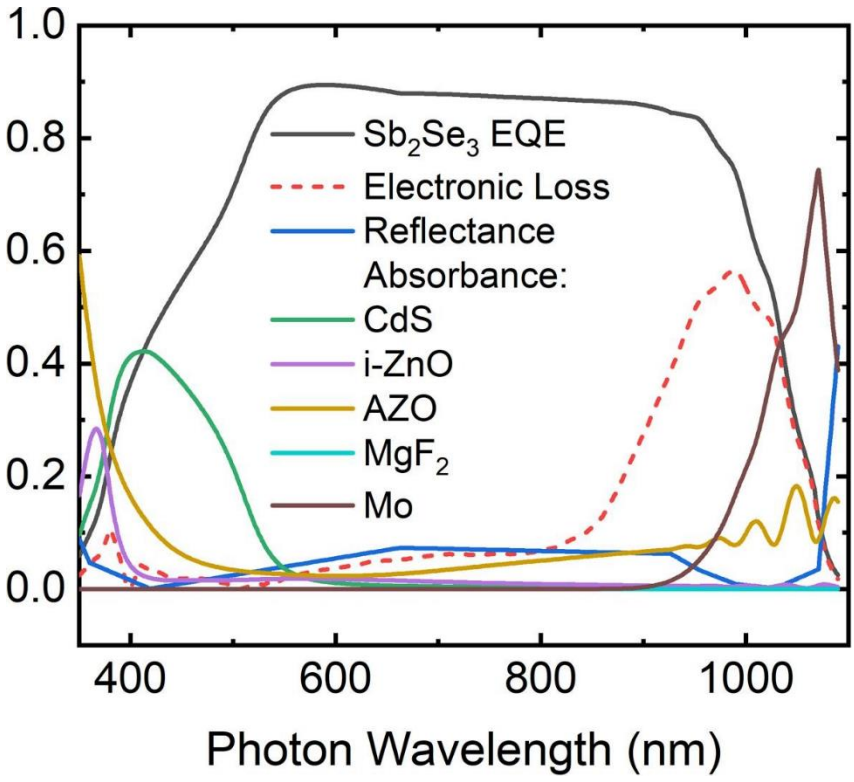

Figure 2- 9: EQE spectrum of a Sb_2Se_3 solar cell with the assumption of complete collection of all the photo-generated, electronic loss from incomplete carrier collection, and other optical absorbance form the component layers of the Sb_2Se_3 solar cell. Reprinted with permission[41]

Chapter 3

Influence of Post-Selenization Temperature on the Performance of Substrate-Type Sb2Se3 Solar Cells

The content of this chapter is published in ACS Applied Energy Materials (S. Rijal et al.,2021)[9] and reprinted with permission.

In this chapter, we systematically investigated the impact of post-deposition annealing temperature on the structural and morphological properties of Sb_2Se_3 thin films deposited on Mo-coated glass substrates by closed-space sublimation (CSS). We tried to understand the influence of selenization on the Sb_2Se_3 absorber layer by SEM, XRD, and absorption characterization. After the proper selenization, a significant device performance improvement from 1.85 to 6.43 % is achieved.

3.1 Introduction

The urgent need for high-efficiency, low-cost, low-toxicity, and stable solar cells drives the sustained research effort on thin-film photovoltaics (PVs) with new absorber materials. Crystalline Si-based solar cells are currently dominating the PV market. However, this first-generation PV technology has several drawbacks: a long energy

payback time, a low industrial production rate, and a high value of an initial investment for the production facility. Over the years, alternative low-cost thin-film PV technologies have been developed, including $Cu(In, Ga)(S, Se)_2$ (CIGSSe), CdTe, and lead halide perovskite solar cells, with power-conversion efficiencies (PCEs) of 22.6%,[42] 22.1%,[43] and 25.5%,[13] respectively, approaching the record efficiency of 26.5%[44] for crystalline Si solar cells. However, due to the concerns regarding the scarcity of Te, In, and Ga, and the toxicity of Cd and Pb, emerging photovoltaic materials with the merits of earth abundance, low cost, and low toxicity have been drawing intense attention in the past few decades.[19] $Cu_2ZnSn (Se, S)_4$ has been considered one of the most promising materials with these merits, such as low cost and non-toxicity constituents.[45] Unfortunately, further efficiency improvement is hindered by its complex phase composition and carrier trapping defects.[46] Recently, simple binary chalcogenides (e.g., SnS,[47] GeSe,[48] Sb_2Se_3,[49] and $Sb_2(S,Se)_3$[50]) appeared as new alternatives with less complex, low-toxicity, and earth-abundant absorbers.[19]

Among them, Sb_2Se_3 is one of the most promising candidates as either single-junction solar cells or the bottom subcells for dual-junction tandem devices due to its high absorption coefficient (10^5 cm^{-1}) and suitable bandgap (1- 1.3 eV).[19] Besides, the properties of the earth-abundant, low-toxicity and low-cost constituents (i.e., Sb and Se) make Sb_2Se_3 a very promising candidate to replace CIGS and CdTe for the long-term development of thin-film solar cells.[19]

Despite decent material properties, the record efficiency of Sb_2Se_3 solar cells is only 9.2%,[49] which is much lower than the theoretical limit exceeding 30%.[28] This is mainly due to the relatively high density of deep defects in the absorber, which accelerated

the recombination rate in Sb_2Se_3 films and at the interfaces.[51] To further improve device performance, the quality of Sb_2Se_3 absorbers should be improved through advancing deposition methods,[33, 34] doping engineering,[52, 53] and post-deposition annealing treatments.[54-56] Among them, the post-deposition annealing treatment has been demonstrated to be one of the most efficient methods for improving CdTe and CIGS solar cells. Typically, post-deposition annealing improves the absorber quality by increasing the crystallinity, tuning the crystal orientation, reducing the bulk trap density, and decreasing non-radiative recombination loss.[33] Some related studies have been done on the Sb_2Se_3 absorber layer. A selenization treatment at 200 ^oC for the thermal evaporated CdS/Sb_2Se_3 solar cells has demonstrated an efficiency improvement from 2.6% to 3.7%.[55] In another study, the selenization treatment of co-evaporated Sb_2Se_3 films was found to improve conversion efficiency from 3.07% to 4.25%.[54] Similarly, sputtered Sb_2Se_3 solar cells with an efficiency of 6.06% have been achieved by tuning the post-selenization parameters.[54] An open-circuit voltage (V_{OC}) exceeding 500 mV has been achieved after selenizing the sputtered Sb_2Se_3 thin-film solar cells.[56] As known from the previous work, the selenization treatment of Sb_2Se_3 films can benefit the film quality and device performance in two ways: 1) compensating the Se loss during the deposition, which helps reduce the V_{Se} related recombination;[55] 2) forming a thin $MoSe_2$ layer at the Sb_2Se_3/Mo interface, eliminating the Schottky barrier and reducing the recombination at the back interface.[54]

In this work, we systematically investigated the impact of post-deposition annealing temperature on the structural and morphological properties of Sb_2Se_3 thin films deposited on Mo-coated glass substrates by closed-space sublimation (CSS) (Figure 3- 1 a),

and the PV performance of corresponding solar cells. We found that at an optimal temperature of 425 °C, Sb_2Se_3 thin films exhibit larger crystal grains, uniform surface morphology, desired crystal orientations, proper stoichiometry, and increased carrier density, leading to a champion PCE of 6.43% in our substrate-type Sb_2Se_3 solar cells.

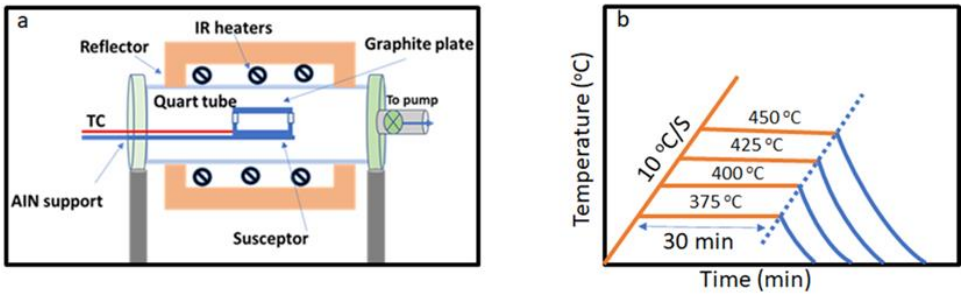

Figure 3- 1**:** (a) Schematic image of the closed space sublimation (CSS) system used in this study. (b) Temperature profile of the post-deposition selenization treatment.

3.2 Experimental Methods

3.2.1 Deposition of Sb_2Se_3 Thin Films

Sb_2Se_3 thin films were deposited on Mo coated soda-lime glass substrates using a closed space sublimation (CSS) system (Figure 3- 1a). First, glass substrates were subsequently cleaned in an ultrasonic bath using detergent and deionized water for 30 min each and then dried by nitrogen flow. A ~600 nm Mo layer was deposited by direct current (DC) sputtering at a power of 180 W in Ar in a two-step process consisting of high pressure of 15 mTorr for 15min and low pressure of 4 mTorr for 90 min. For the Sb_2Se_3 deposition, we first prepared a source plate by depositing a several microns thick Sb_2Se_3 film on a graphite plate at a base pressure of 5 mTorr for half an hour using pure Sb_2Se_3 powders

(99.99%, Jiangxi Ketai Advanced Materials Co. Ltd.). The source (T_{sou}) and substrate (T_{sub}) temperatures were kept at 560 and 350 ^{o}C, respectively. The distance between source and substrate was ~6 mm. The main purpose of making a source plate is to control the sublimation rate. Then, a 200 nm Sb_2Se_3 seed layer was deposited on Mo-coated glass substrates using the source plate, with T_{sou} and T_{sub} at 500 and 315 ^{o}C, respectively, following our previous publication.[38] After that, a bulk Sb_2Se_3 absorber layer was deposited using the source plate with T_{sou} and T_{sub} at 480 and 400 ^{o}C, respectively. During the deposition, a pure nitrogen flow was supplied at a flow rate of 400 sccm to maintain a base pressure of 231 mTorr. The thickness of the absorber layers was ~2 μm for a 6 min deposition run. The obtained absorber layers were then selenized at temperatures from 350 to 450 ^{o}C in Ar at a base pressure of 10 Torr with 100 mg selenium for 30 min to promote the recrystallization of Sb_2Se_3 (Figure 3- 1b).

3.2.2 Deposition of Sb_2Se_3 Thin Films

After the preparation of Sb_2Se_3 thin films, a 55 nm cadmium sulfide (CdS) buffer layer was deposited onto the Sb_2Se_3 absorber layer using chemical bath deposition following the method reported elsewhere.[57] A front contact layer consisting of a 50 nm high-resistive intrinsic zinc oxide (i-ZnO) layer and a 250 nm aluminum-doped zinc oxide (ZnO:Al) was deposited by radio frequency (RF) sputtering using 90 and 150 W powers, respectively, at a pressure of 2 mTorr. Lastly, a 200 nm Ag metal grid was deposited via thermal evaporation. The complete devices were mechanically scribed into individual cells with an active area of 0.2 cm^2.

3.2.3 Characterization

The crystal structure of Sb_2Se_3 films was studied by X-ray diffraction (XRD, Rigaku Ultima III, Cu Kα radiation under operation conditions of 40 kV and 44 mA). The morphology of the Sb_2Se_3 films was characterized by high-resolution field emission scanning electron microscopy (FE-SEM, Hitachi S-4800) equipped with X-ray energy dispersive spectroscopy (EDS). Solar cell performance was characterized by measuring current density-voltage (J−V) curves under AM1.5G illumination using a LED solar simulator (Newport) and a source meter (Keithley 2400) at a scanning speed of 1.17 V/s. External quantum efficiency (EQE) spectra were performed on a QE system (PV Measurements). Capacitance voltage (C-V) measurement is performed using a Solartron Modulab potentiostat equipped with a frequency response analyzer (Ametek Inc.). The capacitance-voltage (C–V) was performed under a constant AC modulation voltage of 45 mV and 10 kHz AC signal superimposed on a DC bias voltage varying from -0.5 to +4 V.

3.3 Results and Discussion

To investigate the impact of selenization temperature on the microstructure of Sb_2Se_3 films, we used scanning electron microscopy (SEM) to examine the surface morphology of Sb_2Se_3 films without annealing and annealed at various temperatures ranging from 375 to 450 ^oC. Figure 3- 2a-d shows that the grain size and compactness

increase, whereas the porosity decreases with the increasing selenization temperature. The average grain size of Sb_2Se_3 films increased from 0.87 μm for the unannealed film to 1.02, 1.16, and 1.72 μm after selenization at 375, 400, and 425 ^oC, respectively (Figure 3- 2g-j). Moreover, the grain size distribution becomes narrower, and grains become more compact at higher temperatures. When a Sb_2Se_3 film was selenized at 450 ^oC, the average grain size further increased to 2.68 μm, (Figure 3- 2k). However, large voids with micrometer sizes appeared, and the film became discontinuous and nonuniform (Figure 3- 2e). This deformation could be attributed to a combined effect of the loss of Se from the Sb_2Se_3 film at a high temperature,[26] the overgrowth of Sb_2Se_3 grains due to Ostwald ripening, and the thermal expansion coefficient mismatch among soda-lime glass ($> 8\times10^{-6}$ K^{-1}),[58] Mo (4.8×10^{-6} K^{-1}),[59] and Sb_2Se_3 (3.7×10^{-5} K^{-1}).[60] Additionally, Energy Dispersive X-ray Spectroscopy (EDS) results (Figure 3- 3) reveal that the Sb_2Se_3 films without selenization and overheated (450 ^oC) have a severe Se-deficient stoichiometry (Se/Sb=1.33 and 1.32, respectively), whereas the films annealed at temperatures of 400 and 425 ^oC have Se/Sb ratios (Se/Sb = 1.43, and 1.44, respectively) closer to the stoichiometric Sb_2Se_3 film (Se/Sb = 1.5). A higher Se/Sb ratio is critical for Sb_2Se_3 solar cells because it helps reduce the non-radiative recombination related to the V_{Se} defects, particularly at Sb_2Se_3 ribbon edges and grain boundaries.[56, 61-63] The optical transmittance measurement shows that all the annealed Sb_2Se_3 films have a bandgap of ~1.2 eV (Figure 3- 4). Overall, the film annealed at 425 ^oC exhibits large and densely packed grains, uniform and smooth film morphology, and appropriate stoichiometry, which are desired properties for Sb_2Se_3 thin-film solar cells.

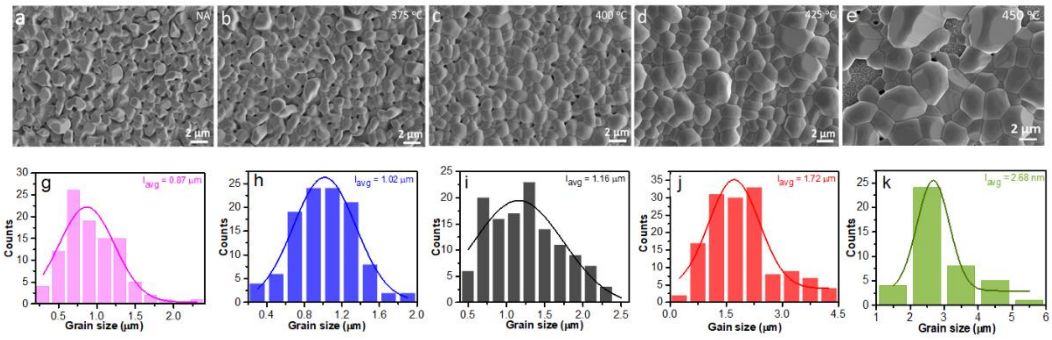

Figure 3- 2**:** Top-view SEM images of Sb_2Se_3 thin films (a) without post-deposition annealing and annealed at different selenization temperatures, including (b) 375, (c) 400, (d) 425, and (e) 450 °C. The corresponding histograms of grain size distribution for Sb_2Se_3 thin films (g) without annealing and annealed at (h) 375, (i) 400, (j) 425 and (k) 450 °C.

Sample	Se (%)	Sb (%)	Se:Sb
NA	57.12	42.88	1.33
375	57.84	42.16	1.37
400	58.92	41.08	1.43
425	59.06	40.96	1.44
450	56.97	43.03	1.32

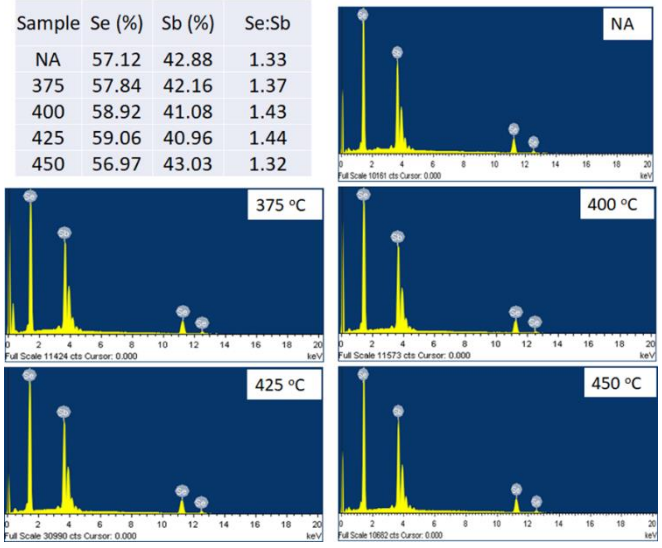

Figure 3- 3**:** EDS analysis of Sb_2Se_3 thin films without post-deposition annealing and annealed at different selenization temperatures.

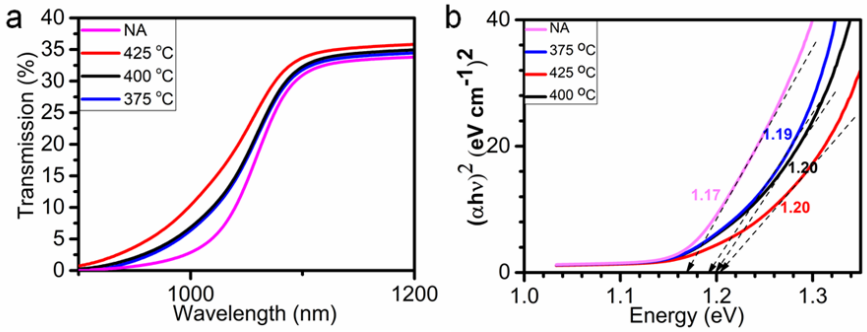

Figure 3- 4**:** (a) Transmittance spectra and the Tauc plot of the Sb_2Se_3 thin films annealed at different selenization temperatures.

X-Ray diffraction (XRD) was used to investigate the impact of selenization temperature on the structural properties of the Sb_2Se_3 thin films deposited on Mo-coated glass substrates. Figure 3- 5a shows the XRD patterns of the Sb_2Se_3 thin films without annealing and annealed at different temperatures of 375, 400, and 425 ^oC. All the diffraction peaks can be indexed to phase pure Sb_2Se_3 in an orthorhombic phase (JCPDS No. 97-008-5676) except the diffraction peak at 40.45^o, which belongs to the Mo substrate underneath. The overall diffraction peak intensity of the Sb_2Se_3 films increases upon increasing selenization temperature, indicating improved crystallinity.

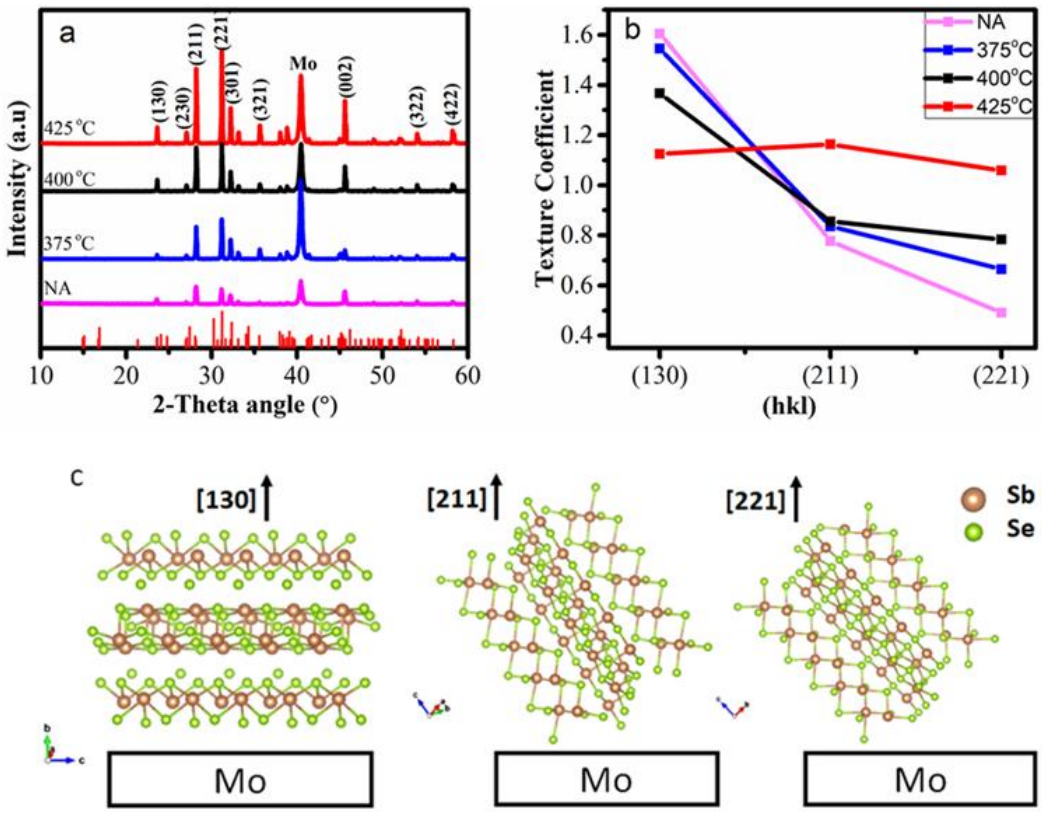

Figure 3- 5**:** (a) XRD patterns and (b) the calculated texture coefficients of Sb_2Se_3 thin films without annealing and annealed at various temperatures. (c) Atomic structures of Sb_2Se_3 in particular crystal orientations.

To study the impact of the annealing temperature on the crystal orientation qualitatively, texture coefficients (TC) for the (130), (211), and (221) diffraction peaks were calculated using the equation:

$$TC(hkl)= \frac{\frac{I(hkl)}{Io(hkl)}}{\sum_{i=1}^{N} \frac{I(h_i k_i l_i)}{Io(h_i k_i l_i)}} \quad \text{.....(1)}$$

where I(hkl) and I_O(hkl) are the diffraction peak intensities of the (hkl) planes in the measured and standard XRD patterns of Sb_2Se_3 (JCPDS 97-008-5676), respectively. A

high TC value of a diffraction peak indicates a preferred orientation along this particular direction.[54] It is worth noting that the CSS-deposited Sb_2Se_3 films on Mo show no XRD peaks below 20°, such as the (020) and (120) peaks, which are known to negatively correlated to the device performance.[61-63] Figure 3- 5b shows that the TC values of the (211) and (221) planes increase, whereas the TC of the (130) plane decreases with the increasing selenization temperature. Due to the unique one-dimensional crystal structure of Sb_2Se_3 (Figure 3- 5c), Sb_2Se_3 films with the (hkl, l≠0) orientations (e.g., oriented in the [211] and [221] directions) are preferred for better carrier transport and collection through the absorber layer. In contrast, (hkl, l = 0) orientated Sb_2Se_3 films (e.g., oriented in the [130] direction) consist of one-dimensional ribbons aligned in the direction parallel to the substrate (Figure 3- 5c), generally result in a high carrier transport barrier through the film thickness.[49, 63] The increased TC values of the (211) and (221) planes for the film annealed at 425 ^oC indicate that the more preferred Sb_2Se_3 film orientations can be obtained at a higher selenization temperature (425 ^oC), predicting better device performances.

To study the impact of selenization temperature on solar cell performance, we fabricated several batches of Sb_2Se_3 solar cells with a substrate-type structure, i.e., Ag grid/ZnO:Al/i-ZnO/CdS/Sb_2Se_3/Mo/glass, as shown in Figure 3- 6a. The cross-sectional SEM analysis of a typical device (annealed at 425 ^oC) shows a compact Sb_2Se_3 absorber layer comprising large grains with a size comparable with the film thickness (Figure 3- 6b and Figure 3- 7). The formation of large grains extended over the entire film thickness and free of horizontal grain boundaries is beneficial for the solar cell performance because of a low density of grain boundaries in the pathway of photoexcited charge carriers.

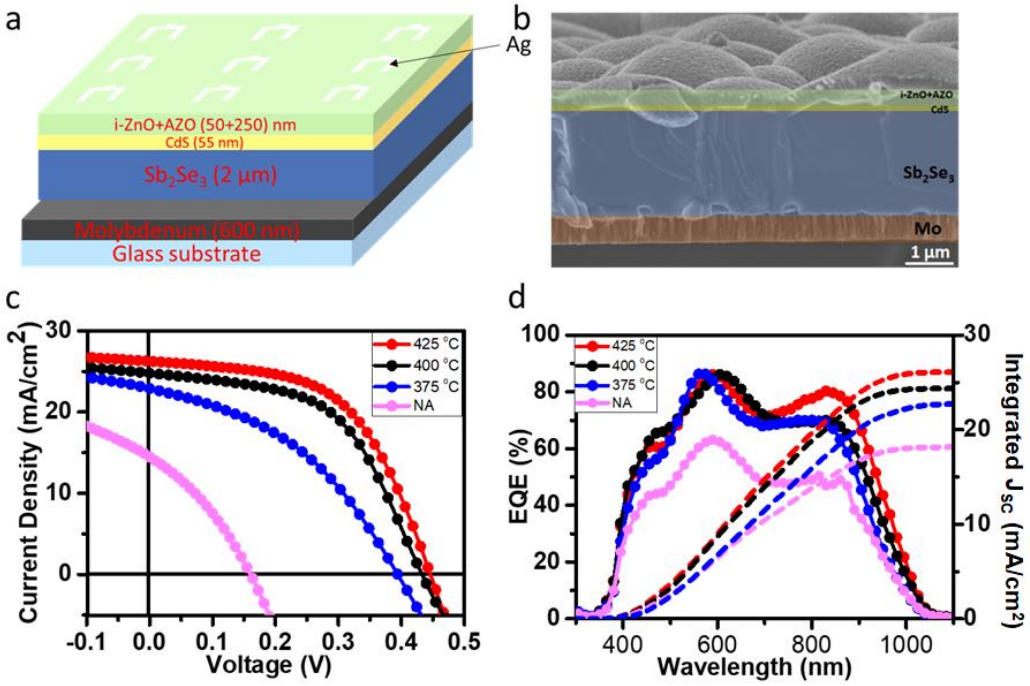

Figure 3- 6**:** (a) Schematic device architecture and (b) cross-sectional SEM image of Sb_2Se_3 solar cells. (c) Current density-voltage (J-V) and (d) external quantum efficiency (EQE) and integrated J_{SC} curves of the Sb_2Se_3 solar cells were prepared without annealing and annealed at different selenization temperatures.

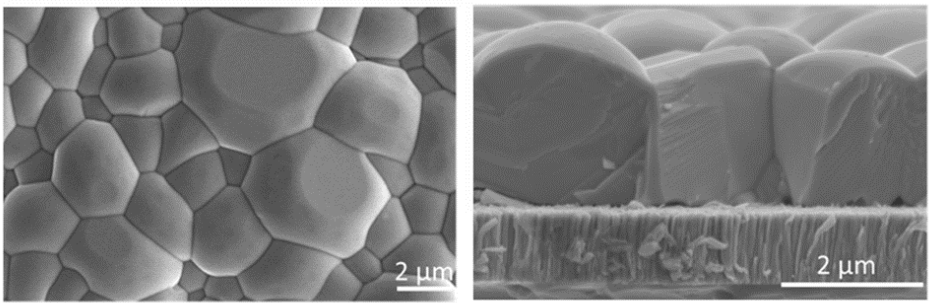

Figure 3- 7**:** Top-view and cross-sectional SEM images of a Sb_2Se_3 film annealed at 425 °C.

We measured the J-V performance of Sb_2Se_3 solar cells prepared under different selenization conditions and summarized the statistical distribution of the key device performance parameters from each annealing condition in Figure 3- 8. Figure 3- 6c shows the J-V curves of the best-performing solar cells using the Sb_2Se_3 absorber layers prepared without annealing and annealed at different temperatures of 375, 400, and 425 ^oC. The detailed PV parameters of these champion devices are tabulated in Table 3- 1. The unannealed Sb_2Se_3 cell shows very poor performance with a PCE of 1.85%, and a low V_{OC} of 285 mV, a low short circuit current density (J_{SC}) of 18.6 mA/cm^2, and a low fill factor (FF) of 34.9%. The inferior PV performance is mainly attributed to small grain sizes, a high defect density due to pinholes and Se-poor stoichiometry, and undesired grain orientations. Selenization at an appropriate elevated temperature (375 to 425 ^oC) significantly increases the device's performance. However, at a too high annealing temperature of 450 ^oC, the devices exhibit poor PV performance (Figure 3- 9) due to the porous Sb_2Se_3 film morphology (Figure 3- 2e). Overall, the annealing temperature of 425 ^oC leads to the best device performance. Comparing with the device annealed at 375 ^oC, the device annealed at 425 ^oC has improved V_{OC} from 394 to 446 mV, J_{SC} from 22.91 to 26.35 mA/cm^2, and FF from 40.51 to 54.90 %, respectively, yielding an overall PCE improvement from 3.6% to 6.43%. The improvements in V_{OC} and FF are attributed to the improved crystallinity, preferred orientation, larger grain size, more compact and uniform morphology, and better stoichiometry of the Sb_2Se_3 films. Particularly, the increasing the selenization temperature from 375 to 425 ^oC decreases the series resistance (R_S) from 7.6 to 4.3 $\Omega \cdot cm^2$ and increases shunt resistance (R_{SH}) from 78.7 to 227.3 $\Omega \cdot cm^2$ (Table 3- 1), likely due to the improved through-film charge transport and reduced pinhole density and

V_{Se} defects, which explain the increased FF. Besides, it is reported that a high selenization temperature can facilitate the formation of a compact $MoSe_2$ between the Mo and Sb_2Se_3, which can improve the back-interface quality and reduce the Schottky barrier height.[54, 64] The improved J_{SC} was further evaluated by external quantum efficiency (EQE) measurements (Figure 3- 6d). When the selenization temperature increases from 375 to 425 °C, EQE shows a significant improvement at longer wavelengths (700 to 1000 nm), suggesting improved absorber quality and a better back interface between Mo and Sb_2Se_3.

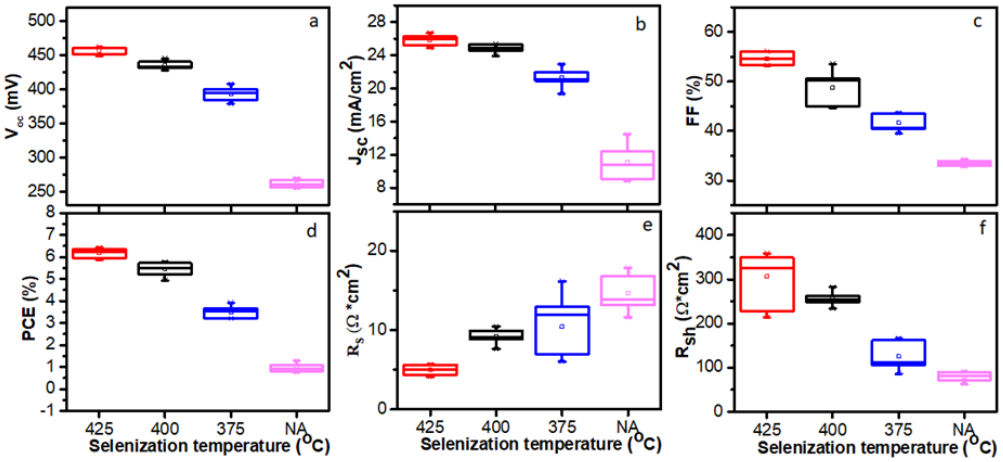

Figure 3- 8**:** Statistic distributions of PV parameters for Sb_2Se_3 solar cells with the Sb_2Se_3 absorber layers prepared without post-deposition annealing (NA) and annealed at different selenization temperatures of 375, 400, 425 °C.

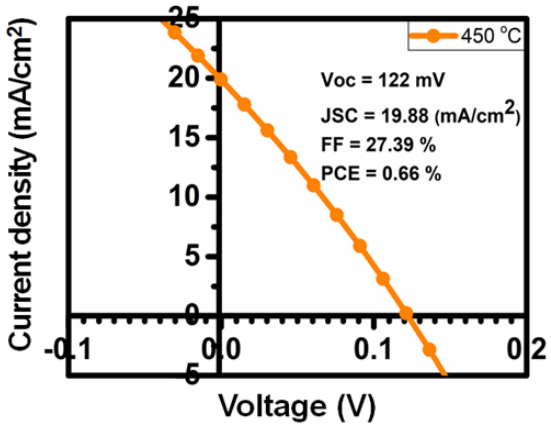

Figure 3- 9**:** J-V curve of a Sb_2Se_3 cell annealed at 450 °C.

Table 3- 1**:** J-V parameters of champion Sb_2Se_3 solar cells without annealing and annealed at different selenization temperatures.

Selenization Temp. (°C)	V_{OC} (mV)	J_{SC} (mA/cm²)	FF (%)	PCE (%)	R_S (Ω·cm²)	R_{SH} (Ω·cm²)
NA	285	18.6	34.9	1.85	8.7	34.2
375	394	22.9	40.5	3.66	7.6	78.7
400	433	24.9	53.6	5.77	6	158.4
425	446	26.4	54.9	6.43	4.3	227.3
450	122	19.9	27.4	0.67	5.5	8.1

Furthermore, capacitance-voltage (C-V) measurement was performed on the 375 and 425 °C annealed cells to understand the effect of selenization temperature on the V_{oc} and carrier concentration Sb_2Se_3 solar cells. Figure 3- 10a shows the Mott–Schottky plot ($1/C^2$ versus V) of cells prepared with these two devices. The built-in potential (V_{bi}) extracted from the Mott-Schottky plot at the intercepts with the x-axis were found to be

450 and 540 mV for the samples selenized at 375 and 425 ^{o}C, respectively, which are consistent with the trend in V_{OC} values obtained from the J-V measurement. The apparent net carrier concentration (N_{cv}) of the absorber layer was calculated by using the following equation [65]:

$$N_{cv} = \frac{2}{q\varepsilon\varepsilon_o}\left[\frac{dC^{-2}(V)}{dV}\right]^{-1} \quad \ldots\ldots\ldots\ldots\ldots\ldots\ldots\ldots\ldots\ldots\ldots\ldots \quad (2)$$

where ε and ε_o are the relative permittivity value of the Sb_2Se_3 films and the absolute permittivity of vacuum, respectively. The value of ε is considered to be 30 for Sb_2Se_3.[66] The distance from the front junction (χ) is calculated directly from $\chi = \varepsilon\varepsilon_o/C$, where C is the capacitance per unit area. The apparent net carrier densities of the Sb_2Se_3 films selenized at 375 and 425 ^{o}C are determined to be 5.69×10^{16} and 7.21×10^{16} cm^{-3}, respectively, as shown in Figure 3- 10b. The change in V_{OC} due to a change in carrier density can be calculated by using the following equation.[54]

$$\Delta V_{oc} = \frac{K_B T}{q}\ln\left(\frac{N_2}{N_1}\right) \quad \ldots\ldots\ldots\ldots\ldots\ldots\ldots\ldots\ldots\ldots\ldots\ldots \quad (3)$$

where N_1 and N_2 are the carrier densities of the film selenized at 325 and 425 ^{o}C, respectively, K_B is the Boltzmann's constant, and T is the temperature. By using Equation 3, we found a negligible change (~6 mV) in the V_{OC} due to this small difference in carrier concentration. Therefore, comparing the cells 425 and 375 ^{o}C annealed cells, the increased V_{OC} of 50-100 mV is mainly due to the reduced recombination in the Sb_2Se_3 layer and its interfaces rather than the increased carrier concentration.

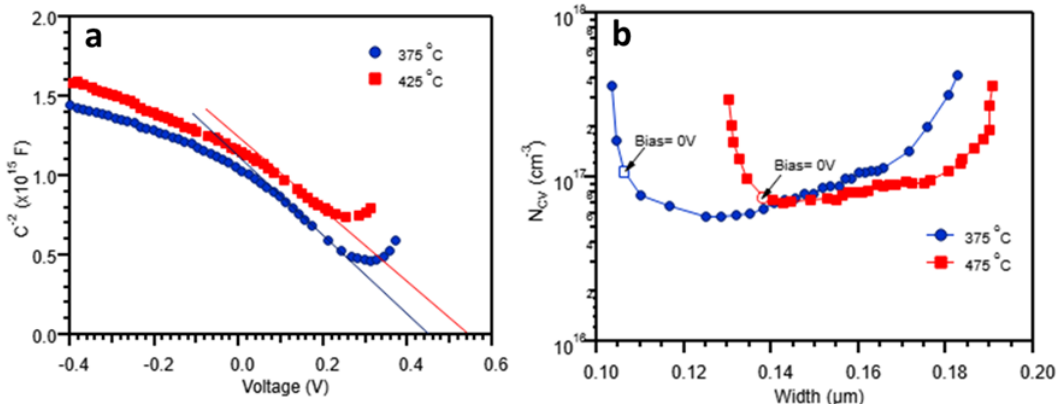

Figure 3- 10: (a) $1/C^2$ versus V curves and (b) carrier density profiles of the Sb_2Se_3 cells selenized at 375 and 425 ^oC.

3.4 Conclusion

In conclusion, we investigated the impact of selenization temperature on the PV performance of substrate-type Sb_2Se_3 solar cells. We identified that the selenization temperature of 425 ^oC was beneficial to increase the grain size and crystallinity and improve the orientation of the Sb_2Se_3 films. In addition, the Se loss during the CSS deposition can be compensated by the selenization process, which results in a reduced V_{Se} related recombination loss. Because of all of these benefits of proper selenization, a significant device performance improvement from 1.85 to 6.43 % is achieved. Further optimization on controlling the amount of Se during selenization could be the next step for improving the quality of the Sb_2Se_3 absorber layer and device performance.

Chapter 4

Templated Growth and Passivation of Vertically Oriented Antimony Selenide Thin Films for High-Efficiency Solar Cells

The content of this chapter is published in Advanced Functional Materials (S. Rijal *et al*., 2022) [25] and reprinted with permission.

Antimony Selenide (Sb_2Se_3) is a promising low-cost photovoltaic material with a one-dimensional crystal structure. The grain orientation and defect passivation play a critical role in determining the performance of polycrystalline Sb_2Se_3 thin-film solar cells. Here, we introduce a seed layer on a molybdenum (Mo) substrate to template the growth of a vertically oriented, columnar Sb_2Se_3 absorber layer by closed space sublimation. By controlling the grain orientation and compactness of the Sb_2Se_3 seeds, we obtain high-quality Sb_2Se_3 absorber layers with passive Sb_2Se_3/Mo interfaces, which in turn improve the transport of photoexcited charge carriers through the absorber layer and its interfaces. We further utilize post-deposition annealing of absorber layers in ambient air to passivate the defects in Sb_2Se_3 and enhance the quality of the front heterojunction. As a result of systematic processing optimization, we fabricate Sb_2Se_3 planar heterojunction solar cells in the substrate configuration with a champion power conversion efficiency of 8.5%.

4.1 Introduction

Antimony selenide (Sb_2Se_3) is emerging as a promising alternative photovoltaic (PV) absorber material to conventional semiconductors, such as silicon (Si), cadmium telluride (CdTe) and cooper indium gallium selenide ($Cu(In,Ga)Se_2$), because of its suitable bandgap of 1.1-1.3 eV, high absorption coefficients of ~10^5 cm^{-1}, low toxicity, low cost, and earth-abundant nature.[19, 41] It has a simple binary composition which provides for much simpler growth with reduced probability for secondary phase formation as is a common problem in $Cu_2ZnSn(S,Se)_4$ and any other ternary Cu chalcogenide compounds.[67, 68] As compared to other emerging PV devices, such as dye-sensitized solar cells, organic PVs, and metal halide perovskite solar cells, Sb_2Se_3 solar cells are robust and more stable in ambient air and may be more able to avoid the need for sophisticated encapsulation.[69]

In a short period, Sb_2Se_3 solar cells have shown a promising learning curve. The record power conversion efficiency (PCE) increased rapidly from 2.1% in 2014 to 9.2% in 2019.[26, 49] However, the PCE of Sb_2Se_3 solar cells is still very far below the corresponding thermodynamic efficiency limit of > 30%,[28] leaving plenty of room for improvement. Studies have shown that the one-dimensional (1D) crystal orientation of Sb_2Se_3 grains and the intrinsic defects in the bulk and at the interfaces dictate the PV performance of Sb_2Se_3 solar cells.[23, 29, 30] The grain orientation determines the charge transport and defect properties throughout the absorber layer. The 1D ribbon-like structures of Sb_2Se_3 can assist in efficient charge transport if the ribbons are aligned perpendicular to the substrate.[23] The bulk and interfacial defects act as recombination centers and limit

the open-circuit voltage (V_{OC}), fill factor (FF), and device performance.[70] Many research efforts have been directed toward improving the quality of Sb_2Se_3 absorber layers, by advancing deposition methods,[34, 38] doping engineering,[52, 53] and post-annealing treatments.[9, 24, 54-56] Meanwhile, a variety of interface engineering strategies were developed to reduce interface recombination and improve the V_{OC} and PCE, including surface treatment to induce grain boundary (GB) inversion,[71] introduction of tunable buffer layers,[72] and management of buffer/absorber band energy alignment.[73]

Improving the desired crystal orientation and bulk defect properties is essential for the improvement of the performance of Sb_2Se_3 solar cells. Introducing a seed layer between the substrate and Sb_2Se_3 is found to be an effective way to improve the absorber quality and interface. Huntter et al. first introduced a seed layer in the preparation of superstrate Sb_2Se_3 solar cells by two-step closed space sublimation (CSS).[74] Kondrotas et.al. further studied the growth mechanism of Sb_2Se_3 thin films by a vapor transport deposition method and found three growth regimes by varying the substrate and source temperatures on different substrates.[75] Li et.al. studied the impact of introducing a seed layer in between TiO_2 and Sb_2Se_3 and found that the seed layer improved the interface and promoted oriented crystal growth.[23] A 7.5% efficient Sb_2Se_3 solar cell was fabricated by introducing a seed layer in planar superstrate n-i-p structure devices.[76]

In addition to the grain orientation control, the passivation of the bulk and interfacial defects is essential to suppress the recombination in Sb_2Se_3 solar cells and to achieve high-efficiency devices. Oxygen passivation is found to be a ubiquitous and simple strategy for a variety of chalcogenide thin-film solar cells.[77-80] Various oxygen passivation strategies have been applied to Sb_2Se_3 solar cells.[69, 70, 81] For instance, Liu

et al. introduced controlled oxygen during the Sb_2Se_3 film growth and improved the PCE to over 4%.[70] Fleck et al. studied how exposure to air increased the efficiency of Sb_2Se_3 solar cells via a reduction in the back contact barrier height.[69]

Here, we fabricate substrate-type Sb_2Se_3 solar cells using a CSS setup built in house **(**Error! Reference source not found.**)**. We first introduce a seed layer on a molybdenum (Mo) substrate by rapid thermal evaporation (RTE) to enable the templated growth of vertically orientated Sb_2Se_3, which not only facilitates the growth of high-quality Sb_2Se_3 absorber layers with high crystallinity, large columnar grains, and preferred orientation but also avoids the void formation at the back interface. We further employ facile post-deposition annealing in ambient air to passivate the bulk defects in the Sb_2Se_3 absorber layers. The passivation effect is verified by admittance spectroscopy measurements, which show the removal of some defects and shallower defect activation energies after annealing in the air. Additionally, c-AFM and KPFM measurements show the slightly reduced conductivity and increased top surface potential of the films after air annealing, benefiting the charge extraction at the front heterojunction. As a result, we fabricate Sb_2Se_3 solar cells with a champion efficiency of 8.5%, which is the highest reported efficiency to date for Sb_2Se_3 planar heterojunction solar cells (Table 4- 1).

Table 4- 1: Comparison of planar heterojunction Sb_2Se_3 solar cells with different fabrication methods in a different configuration.

Method	Device configuration	Eff (%)	V_{OC} (mV)	J_{SC} (mA/cm^2)	FF (%)	Ref.
Sputtering	Glass/Mo/Sb_2Se_3/CdS/ZnO/AZO/Ag	3.35	437	15.93	48	[82]
Co-evaporation	Glass/Mo/Sb_2Se_3/CdS/ZnO/AZO/Ag	4.25	427	17.11	58.15	[54]
Sputtering	Glass/Mo/Sb_2Se_3/CdS/ITO/Ag	6.06	494	25.91	47.7	[63]
sputtering	Glass/Mo/Sb_2Se_3/CdS/ITO/Ag	6.15	455	22.75	59.5	[57]
Sputtering	Glass/Mo/Sb_2Se_3/CdS/ITO/Ag	6.84	504	24.91	54.47	[56]
VTD	FTO/ CdS/Sb2Se3/Al2O3/Au	7.35	405	31.02	58.52	[83]
VTD	(ITO)/CdS/Sb2(S,Se)3/Sb2Se3/Au	7.49	430	28.22	61.71	[84]
VTD	ITO/CdS/Sb2Se3/Au	7.60	420	29.90	60.40	[34]
RTE	FTO/TiO2/Sb2Se3/PbS CQD/Au	7.62	386	32.6	60.6	[23]
CSS	Glass/Mo/Sb_2Se_3/CdxZn1-xS/ZnO/ZnO:Al	6.71	403	25.69	64.78	[73]
CSS	Glass/Mo/Sb_2Se_3/Cds/i-ZnO/AZO/Ag	7.07	474	26.32	56.61	[24]
CSS	Glass/Mo/MoSe2/Sb_2Se_3/TiO2/Cds/i-ZnO/AZO/Ag **(Nano rod structure)**	9.20	400	32.58	70.3	[49]
CSS	FTO/SnO2/CdS/Sb_2Se_3/Se/Au	7.45	413	28.9	62.3	[30]
CSS	Glass/Mo/Sb_2Se_3/Cds/i-ZnO/AZO/Ag	8.5	505	27.74	60.7	**This work**

4.2 Experimental Details

4.2.1 Deposition of Sb_2Se_3 Thin Films

Sb_2Se_3 seed and bulk layers were prepared on Mo coated soda-lime glass substrate by rapid thermal evaporation (RTE) and closed space sublimation (CSS) methods, respectively. First, glass substrates were subsequently cleaned in an ultrasonic bath using detergent and deionized water and dried by nitrogen blowing. Then, a bilayer Mo film was deposited by direct current (DC) sputtering in an argon (Ar) environment in a two-step process, consisting of the high working pressure of 15 mT for the adhesion layer and a low working pressure of 4 mT for the bulk Mo film. The total thickness of Mo is ~ 900 nm.

To deposit Sb_2Se_3 films, we prepared a source plate by using high-purity Sb_2Se_3 powders (Jiangxi Ketai Advanced Materials Co. Ltd.). A several microns thick Sb_2Se_3 film was deposited on a graphite plate at a base pressure of 5 mT by keeping the substrate temperature (T_{sub}) at 350 °C and source temperature (T_{sou}) at 560 °C for half an hour in a CSS system.[9, 38] The main purpose of making a source plate is to control the sublimation rate. A spacer with a height of 6 mm was used between the source plate and the Mo coated glass substrates. Sb_2Se_3 absorber layers were deposited by a two-step process. The substrate and Sb_2Se_3 source plate were first preheated at 315 °C for 5 min using Infrared (IR) heaters. Sb_2Se_3 seed layers were deposited at different source temperatures ranging from 475 to 525 °C using a RTE approach **(**Error! Reference source not found.**)**, i.e., ramping up the s ource temperature to the set point and immediately cooling down to room temperature naturally while maintaining pressure at 230 mTorr. We placed a graphite plate on the top of Mo substrates to maintain uniform temperature on the Mo substrates during the

sublimation process. After absorbing the infrared light from the IR heaters, Sb_2Se_3 powders evaporated and formed a thin seed layer on the Mo substrates. During the deposition, T_{sub} was kept constant at 315 °C. Note that increasing T_{sou} also increases T_{sub} unintentionally. T_{sub} increased to 340, 370, and 400 °C when T_{sou} were set to 475, 500, and 525 °C, respectively. After that, a bulk Sb_2Se_3 layer was deposited on top of the seed layer by CSS method where T_{sou} was at 480 °C and T_{sub} was at 400 °C. The deposition was carried out under a nitrogen flow at 400 sccm and a base pressure of 230 mT. The total deposition time was 6 min, and the thickness of Sb_2Se_3 absorber layers was ~2 μm. The obtained absorber layers were selenized at 425 °C in Ar with 50 mg selenium powders to improve the crystallization of the Sb_2Se_3 films.

4.2.2 Device Fabrication

After the selenization, Sb_2Se_3 thin films were annealed on a hot plate in ambient air at different temperatures for 1 min. After the annealing of Sb_2Se_3 thin films, a 55 nm CdS buffer layer was deposited on the top of crystallized Sb_2Se_3 films using chemical bath deposition (CBD) following the method reported elsewhere.[38] A 50 nm ZnO high-resistive layer and a 250 nm aluminum doped zinc oxide (AZO) front contact layer were then deposited by radiofrequency (rf) sputtering at a power of 100 and 150 W, respectively. Lastly, a 200 nm Ag metal grid was deposited on the AZO layer via thermal evaporation. The completed film stacks were then mechanically scribed into individual cells with an active area of 0.2 cm^2. Devices were categorized into four groups: SL-475, SL-500, SL-525, and SL-NS according to the seed layer deposition conditions. Here, SL-475 denotes a device whose seed layer was deposited at T_{sou} of 475 ˚C. Similarly, SL-500, and SL-525,

represent devices with the seed layers deposited at 500 and 525 ˚C, respectively. SL-NS denotes the devices prepared without a seed layer. The structural schematic diagram of Sb_2Se_3 solar cells and the RTE equipment are shown in **Error! Reference source not found.**.

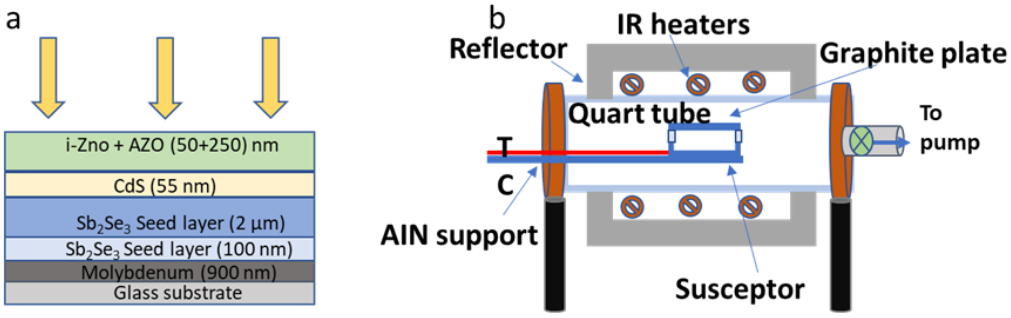

Figure 4- 1: Schematic diagram of (a) Sb_2Se_3 solar cell and (b) the closed space sublimation (CSS) system used in this study.

4.2.3 Measurement and Characterization

X-ray diffraction (XRD, Rigaku Ultima III, Cu Kα radiation under operation conditions of 40 kV and 44 mA) was used to analyze the crystal structure of Sb_2Se_3 films. The morphology of the Sb_2Se_3 films was characterized by using high-resolution field emission scanning electron microscopy (FE-SEM, Hitachi S-4800) equipped with X-ray energy dispersive spectroscopy (EDS). The performance of the solar cells was measured using density-voltage (J-V) curves under AM1.5 illumination by a LED solar simulator (Newport) and a source meter (Keithley 2400) at a scanning speed of 1.17 V/s. QE system (PV Measurement Beaverton, OR, USA) was used to measure the external quantum efficiency (EQE) spectra. Kelvin probe force microscopy (KPFM) was performed on a

home built KPFM system based on D3100 atomic force microscope (AFM). Conductive AFM was performed on a Bruker Dimension Icon system. Pt-Ir-coated silicon probes (Nano sensor PPP-EFM) were used in both measurements. The scan size is $5 \times 5\ \mu m^2$ that contains 1024 × 256 pixels. TAS and J-V-T measurements were done by Modulab potentiostat equipped with a frequency response analyzer (Ametek Inc.). A built in XM-studio software to the Modulabl system is used to set up, run experiments, and obtain the results. TAS was performed under a constant AC modulation voltage of 45 mV_{rms}. Frequency sweeping from 1.0 MHz to 0.1 Hz was used for the TAS measurement. During TAS measurement DC biases varying from -0.3 to 0.2 V at a step size of 0.1 V. J-V-T measurements were scanned with DC biases varying from 0.0 to 0.9 V. A liquid- nitrogen cooled cryogenic system (Janis VPF-100) was used to carry out all the temperature-dependent (110-310k with a temperature step size of 10K) measurements. A temperature controller (Lakeshore 330) was used to control the temperature. To make sure that the recorded temperature is from the samples, a temperature sensor was mounted directly on the top of the device.

4.3 Results and Discussion

4.3.1 Seeded Growth of Vertically Oriented Sb_2Se_3

The crystallinity and orientation of polycrystalline Sb_2Se_3 thin films is particularly important because of their anisotropic optical and electrical properties.[85] The seed layer plays a crucial role in controlling the crystalline quality and preferred orientation of Sb_2Se_3 thin films and their interface properties.[23] It is known that for Sb_2Se_3, the growth of 1D

$(Sb_4Se_6)_4$ ribbons can be oriented in mainly two groups of directions with respect to the substrate surface, i.e., the lying ribbons with their [hk0] directions being perpendicular to the substrate surface **(**Figure 4- 3**a)** and the standing ribbons with their [hkl, l≠0] directions being perpendicular to the substrate surface **(**Figure 4- 3**b)**, depending on growth conditions such as substrate temperature, source temperature, and pressure.[38, 54, 86] In the film growth direction, the lying ribbon crystals oriented in [hk0] are terminated with fully saturated Se atoms. Therefore, the ribbons are bonded by the weak Van der Waals force **(**Figure 4- 3**a)**, whereas standing crystals oriented in [hkl, l≠0] are terminated by atoms with unsaturated atoms (either Sb or Se atoms) that can potentially form strong chemical bonds with functional contact materials **(**Figure 4- 3**b)**.[23] When ribbons are orientated in the [hkl, l≠0] directions, charge carriers can be easily transported through the interface owing to the strong chemical bonds.[54] In contrast, charge transport along the [hk0] directions needs to overcome the interchain barriers, which is less efficient. Thus, the [hkl, l≠0] is the preferred orientation that benefits the transport of photoexcited carriers and, consequently, the device performance of Sb_2Se_3 solar cells.

To prepare Sb_2Se_3 films with the preferred crystal orientations, we introduce a template seed layer on Mo substrates by using RTE. The morphology and structural properties of Sb_2Se_3 seed layers deposited at different source temperatures (T_{sou}) were characterized by scanning electron microscopy (SEM) and X-ray diffraction (XRD). Figure 4- 2 shows a series of top-view and cross-sectional SEM images of Sb_2Se_3 seed layers grown on Mo substrates at different temperatures, exhibiting the morphological evolution of Sb_2Se_3 seed layers as a function of T_{sou}. At T_{sou} = 475 °C, loosely packed and randomly oriented grains with ribbon-like structures were formed. When T_{sou} was

increased to 500 ℃, the seed layer became more compact, and the ribbon grains were oriented mainly along the vertical direction. Further increasing T_{sou} to 525 ℃ led to the formation of a dense layer of randomly oriented ribbon grains. Energy-dispersive X-ray spectroscopy (EDS) measurements (Table 4- 2) show that all the seed layers are Se rich. Because the partial vapor pressure of Se is much lower than that of the Sb, it is critical to deposit the seed layer at a rapid temperate ramp rate to the desired temperature to preserve the Se-rich stoichiometry.

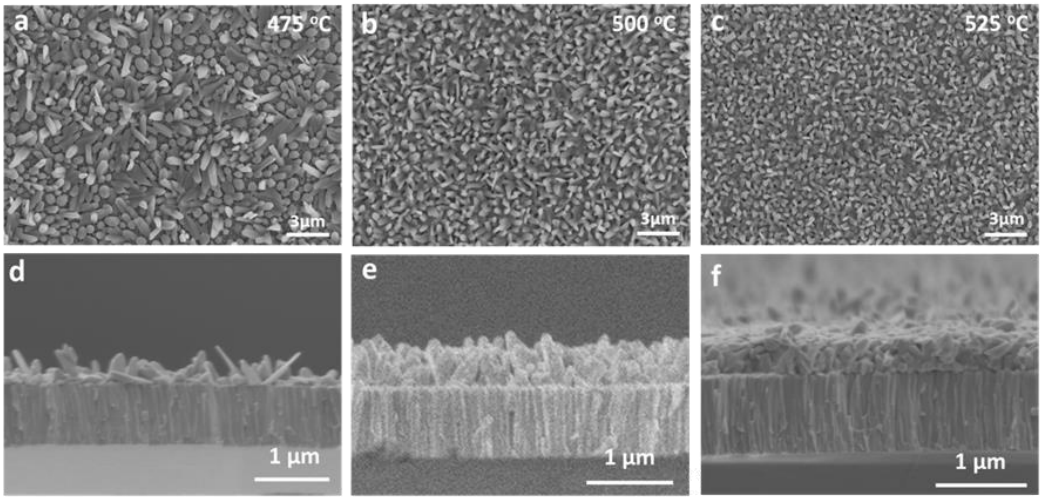

Figure 4- 2: Morphological evolution of Sb_2Se_3 seed layers: from nanorod array to thin film. (a-c) Top-view SEM images of Sb_2Se_3 seed layers prepared at different source temperatures: (a) 475 °C, (b) 500 °C, and (c) 525 °C. (d-f) Cross-sectional images of Sb_2Se_3 seed layers prepared at different source temperatures: (d) 475 °C, (e) 500 °C, and (f) 525 °C.

The changes in the crystal orientation of the Sb_2Se_3 seed layers with T_{sou} can be measured by analyzing the XRD data, as shown in Figure 4- 3**c**. Among the seed layers

grown at different temperatures of 475, 500, and 525 °C, the film deposited at 500 °C exhibits the lowest intensities for the undesired (020), (120), and (130) peaks and the highest intensities for the preferred (211), (221), and (002) peaks. We further quantified the crystal orientation changes by the texture coefficients (TC) for the (020), (120), (130), (221), (211), and (002) peaks using the following equation:

$$TC(hkl) = \frac{\frac{I(hkl)}{I_o(hkl)}}{\sum_{i=1}^{N} \frac{I(h_i k_i l_i)}{I_o(h_i k_i l_i)}} \qquad \ldots\ldots\ldots\ldots\ldots\ldots\ldots\ldots\ldots\ldots (1)$$

where $I(hkl)$ and $I_o(hkl)$ are the diffraction peak intensities of the (hkl) planes in the measured and standard XRD patterns of Sb_2Se_3 (JCPDS 97-008-5676), respectively. The texture coefficient analysis of the seed layers **(**Figure 4- 3**d)** confirms that the 500 °C deposited seed layer has preferred orientations in the [hkl, l≠0] directions. Increasing the [hkl, l≠0] orientation and reducing the [hk0] orientation can be explained by the adhesion force between the Sb_2Se_3 ribbon grains and the Mo substrate. Sb_2Se_3 grains in the [hk0] directions are bonded to the substrates via a weak Van der Waals force, while grains in the [hkl, l≠0] directions are bonded to the substrate via a stronger chemical bonding. At a low temperature (475 °C), the deposition rate is low, and the individual grains with all the orientations can randomly grow on the substrates. At a higher temperature (500 °C), the [hk0]-oriented grains are more easily to break down the adhesion and evaporate from the Mo substrate, leaving behind a seed layer with more strongly bonded [hkl, l≠0]-oriented grains. Further increasing the temperature to 525 °C leads to the rapid formation of a densely packed layers consisting of randomly oriented grains due to a higher deposition rate.

Table 4- 2: EDS analysis of Sb_2Se_3 seed layers grown at different source temperatures.

Seed layer at (°C)	Se (Atomic %)	Sb (Atomic %)	Se:Sb
475	67.7	32.3	2.1
500	67.98	32.02	2.12
525	69.21	30.79	2.25

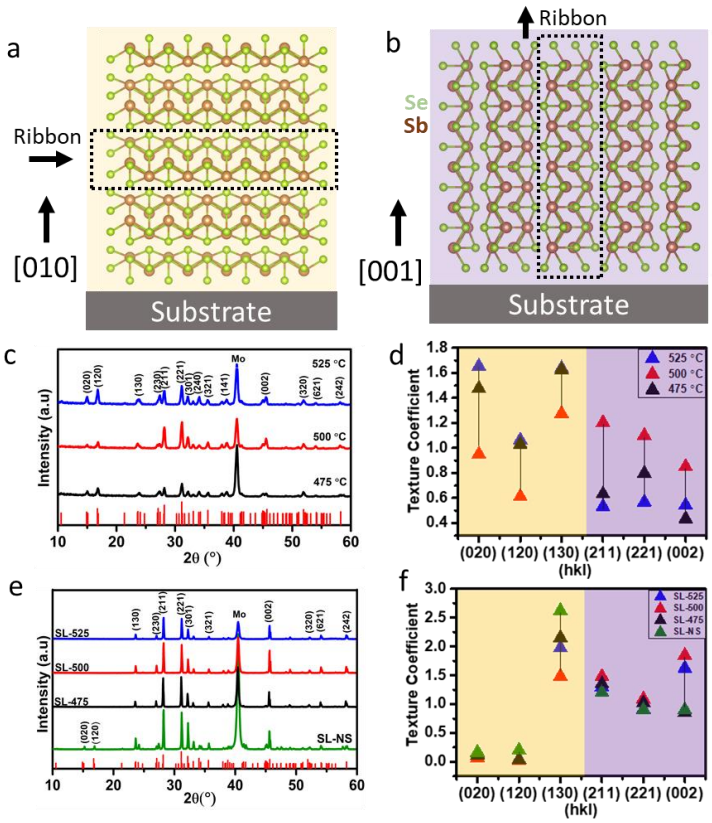

Figure 4- 3**:** Structural properties of Sb_2Se_3 thin films. Crystal structures of Sb_2Se_3 in the (a) [010] and (b) [001] orientations. (c) XRD patterns and (d) texture coefficients of Sb_2Se_3

seed layers grown on Mo at different source temperatures. (e) XRD patterns and (f) texture coefficients of Sb_2Se_3 absorber layers grown on different seed layers.

Figure 4- 3**e** compares the XRD patterns of the Sb_2Se_3 absorber layers prepared on the seed layers deposited at different temperatures and a Sb_2Se_3 absorber layer deposited without a seed layer as a reference. The Sb_2Se_3 film prepared without a seed layer (SL-NS) consists of the unfavorable (020) and (120) peaks, consistent with the seed layers directly grown on Mo substrates. Interestingly, Sb_2Se_3 films grown on top of the seed layer templates are absent of these undesired peaks. The results indicate that the weakly bonded [hk0] horizontal ribbons were not stabilized on the substrate and could reorient during the deposition of bulk Sb_2Se_3 films. A comparison of the XRD peaks among the Sb_2Se_3 films grown on different seed layers deposited at 475, 500, and 525 °C (referred to as SL-475, SL-500, and SL-525, respectively) reveals that the preferred peaks (211), (221), and (002) of the SL-500 sample has the highest intensity. Figure 4- 3**f** shows the TC analysis of these Sb_2Se_3 films. The SL-500 sample exhibits the highest TCs for the (211), (221), and (002) peaks and lowest values for the (hk0) peaks. The results confirm that the templated growth based on Sb_2Se_3 seed layers helps orient the grains in the preferred directions.

4- 4**a-h** displays the top-view and cross-sectional SEM images of the bulk Sb_2Se_3 absorber layers grown without a seed layer or on various seed layers deposited at different temperatures. 4- 4**a** shows that the Sb_2Se_3 absorber layer grown without a seed layer has a nonuniform morphology with a high degree of porosity. 4- 4**b-d** shows that Sb_2Se_3 absorber layers grown on a seed layer are more compact and uniform than that without a seed layer. Figure 4- 5 shows the histogram analysis of grain size under different seed layer conditions. The grain size increases, and void density decreases when the seed layer deposition

temperature increases from 475 to 500 °C, but the trend is reversed when the temperature increases to 525 °C. The 500 °C sample shows the largest average grain size of 1.56 µm **(**Figure 4- 5**3-c)**.

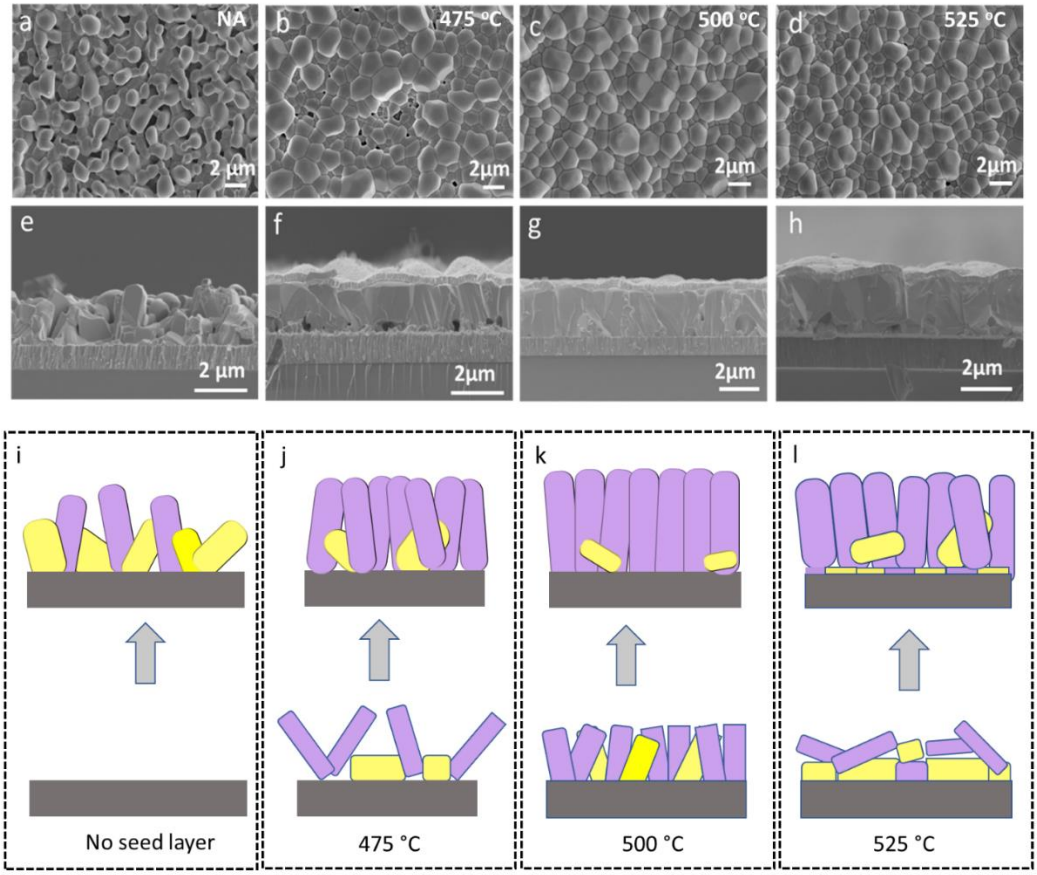

Figure 4- 4**:** Templated growth of Sb_2Se_3 thin films on different seed layers. (a-d) plane view SEM images of Sb_2Se_3 thin films grown (a) without seed layer and on seed layers deposited at (b) 475 °C, (c) 500 °C, and (d) 525 °C, respectively. (e-h) Corresponding cross-sectional images of Sb_2Se_3 films grown on different seed layers. (i-l) Schematic illustrations of templated growth of Sb_2Se_3 thin films.

The seed layer also significantly influences the interfacial adhesion between the Sb_2Se_3 absorber layer and Mo back electrode. The cross-sectional SEM images **(**4- 4**2e-h)**

show that the Sb_2Se_3/Mo interface became more compact and void-less after introducing the seed layer. The 475 °C sample still exhibits a high density of pores at the interface **(**4-4**f)**, whereas the 500 °C sample is completely void-free **(**4- 4**g)**. Unlike other films, the 525 °C sample shows a bi-layer structure consisting of a thin small-grained underlying layer and a thicker large-grained upper layer **(**4- 4**h)**. The growth process of the seed layer and absorber can simply be described by the schematics of the growth shown in 4- 4**i-l**. The direct deposition of Sb_2Se_3 on Mo results in randomly distributed and oriented grains **(**4-4**i)**, due to the relatively low free energies for the nucleation of all the crystal orientations. The seed layer grown at 475 °C is discontinuous, consisting of randomly and loosely distributed grains **(**4- 4**j)**. When the Sb_2Se_3 absorber layer is deposited, some traces of the seed layer are left over at the interface, while most of the seed grains recrystallize and merge with the absorber layer and are reoriented in the perpendicular direction. The seed layer deposited at 500 °C is compact and mainly oriented in the desired [hkl, l≠0] directions **(**4- 4**k)**. The seed grains grow to larger sizes after the deposition of the bulk absorber layer, retaining mostly in the [hkl, l≠0] orientations. The seed layer deposited at 525 °C comprises densely packed and randomly oriented seed grains **(**4- 4**i)**. Owing to the strong intralayer adhesion, the seed layer structure is preserved after growing the bulk absorber layer, resulting in a distinct bi-layer structure. The presence of a bi-layer structure in the absorber layer is typically detrimental to device performance because it may hinder the charge transport and introduce non-radiative recombination.

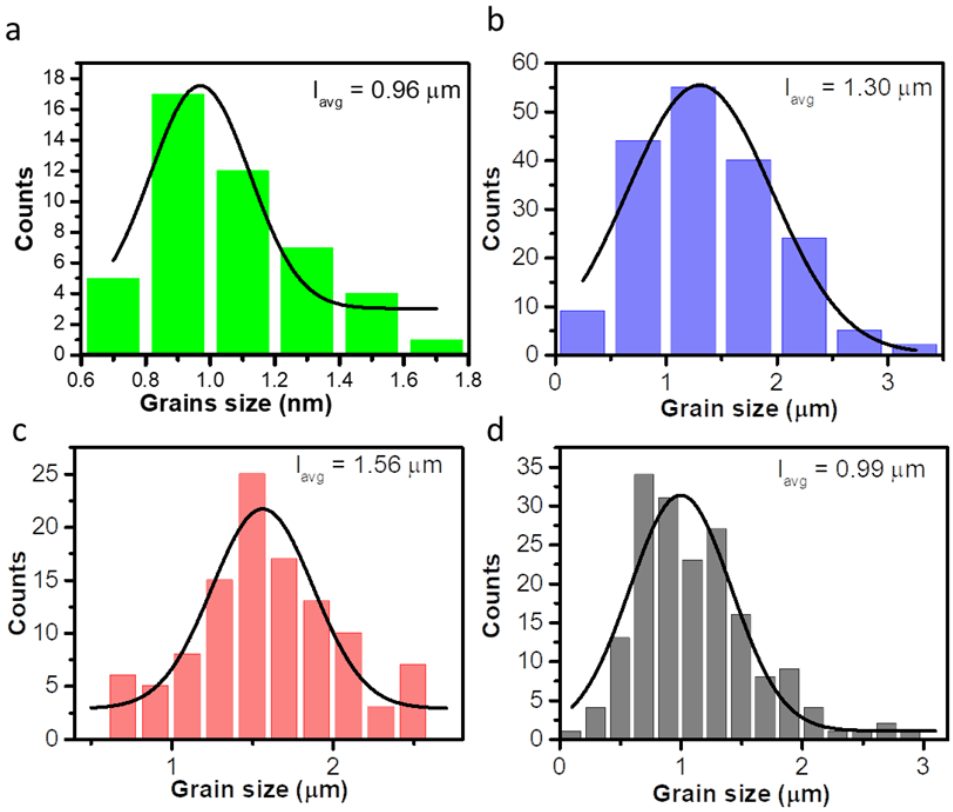

Figure 4- 5:Grain size distribution of the films at different seed layer conditions (a) without seed layer, (b) 475 °C, (c) 500 °C, and (d) 525 °C.

To investigate the impact of the seed layer growth condition on solar cell performance, we fabricated substrate-type Sb_2Se_3 solar cells with a structure of glass/Mo/Sb_2Se_3/CdS/i-ZnO/AZO/Ag grid. Figure 4- 6**a** shows the J-V curves of the best-performing cells from each group of devices. Their corresponding key PV parameters are summarized in Table 4- 3. The SL-500 device shows the highest PCE of 7.47%, with high open-circuit voltage (V_{OC}), short-circuit current density (J_{SC}), and fill factor (FF) of 459 mV, 26.54 mA cm^{-2}, and 61.39%, respectively. The other two devices, SL-475 and SL-525, show lower values for all the PV parameters. The SL-475 device suffers severely from

high series resistance (R_S) and low shunt resistance (R_{SH}), which are mainly attributed to a high proportion of the undesired [hk0] oriented grains and the voids at the Sb_2Se_3/Mo interface. The horizontal ribbon grains with the [hk0] orientations are more likely to introduce non-radiative recombination centers at the GBs, resulting in an overall low external quantum efficiency (EQE) for the SL-475 sample **(**Figure 4- 6**b)** and a low V_{OC} of 412 mV. The SL-525 device shows improved V_{OC} and J_{SC} compared with SL-475 but is adversely affected by the misaligned interface layer between the bulk Sb_2Se_3 and Mo, which hinders the charge transport and leads to a high R_S. The device performances of SL-500 are superior in every parameter to that of any other device. The highest performance of the SL-500 device is attributed to the more desired crystal orientation in the [hkl, l≠0] directions **(**Figure 4- 3**f)** because the grains in the [hkl, l≠0] favor charge transport throughout the film and lower recombination in the absorber layer. Particularly, an overall high EQE and an increase in the longer wavelength range (> 600 nm) indicate better absorber quality and improved back contact at the interface of Mo and Sb_2Se_3, compared with the other two devices. Figure 4- 6**c-f** compares the statistical distribution of the key PV parameters for these devices, showing the same trend as in the champion device comparison.

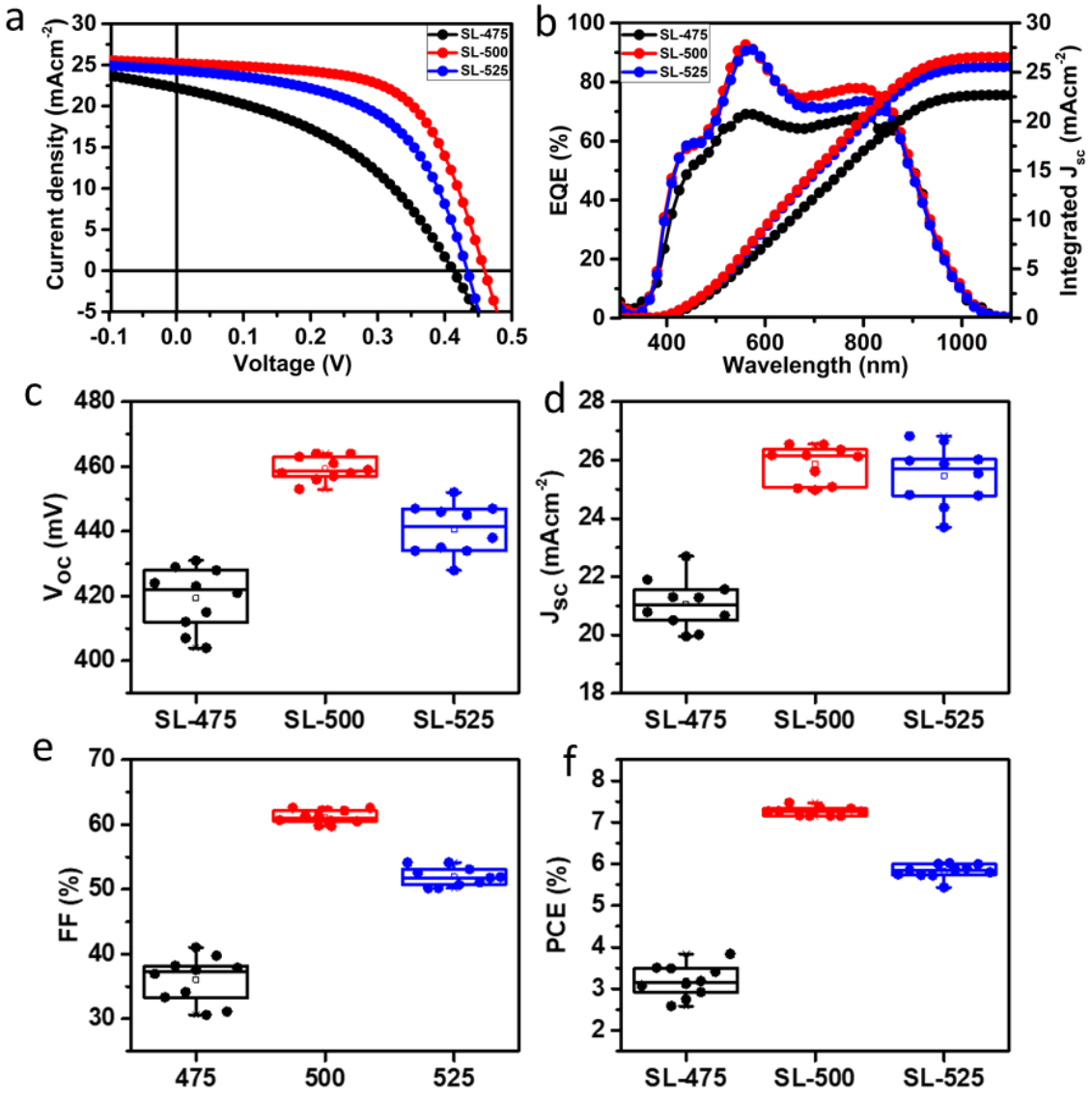

Figure 4- 6**:** (a**)** J-V and (b) EQE curves of the champion Sb_2Se_3 solar cells grown on different seed layer conditions. (c-f) Statistical distributions of (c) V_{OC}, (d) J_{SC}, (e) FF, and (f) PCE of Sb_2Se_3 solar cells grown on different seed layer conditions.

Table 4- 3**:** PV parameters of champion Sb_2Se_3 solar cells for different seed layer conditions

Samples	V_{OC} (mV)	J_{SC} ($mAcm^{-2}$)	FF (%)	PCE (%)	R_S (Ωcm^{-2})	R_{SH} (Ωcm^{-2})
SL-475	412	22.70	41.03	3.84	6.84	79.86
SL-500	459	26.54	61.39	7.47	3.81	310.74
SL-525	434	25.54	54.14	6.00	5.21	169.65

To better understand how the seed layer and grain orientation influence solar cell performance, we used a solar cell capacitance simulator (SCAPS)[87] to study the impact of bulk defect density, R_S, and R_{SH} on the PV performance of Sb_2Se_3 solar cells. [88, 89]Because of the 1D crystal structure, detrimental defects are mainly distributed at the ends of the $(Sb_4Se_6)_4$ ribbons, while the sides are mostly self-passivated. The horizontal grains in the [hk0] directions typically introduce more defects at GBs in the bulk Sb_2Se_3 film, whereas the vertical grains in the [hkl, l≠0] directions mainly have defects at the top and rear surfaces. Therefore, the bulk defect density in a Sb_2Se_3 film is determined by the grain orientation. We simulated the J-V and EQE curves of Sb_2Se_3 solar cells with different bulk defect densities from 10^{15} to 10^{18} cm^{-3} **(**Figure 4- 7**)** and found that bulk defect-induced Shockley-Read-Hall (SRH) recombination is the most critical factor limiting the performance of solar cells. Additionally, the seed layer condition also affects R_S and R_{SH}, which can lower the PV performance of Sb_2Se_3 solar cells. Based on the above results, we conclude that seed layers play a vital role in obtaining the desired orientation of the grains

and high crystallinity of the absorber layer and optimizing the Sb_2Se_3/Mo interface resistance, ultimately govern the performance of solar cells.

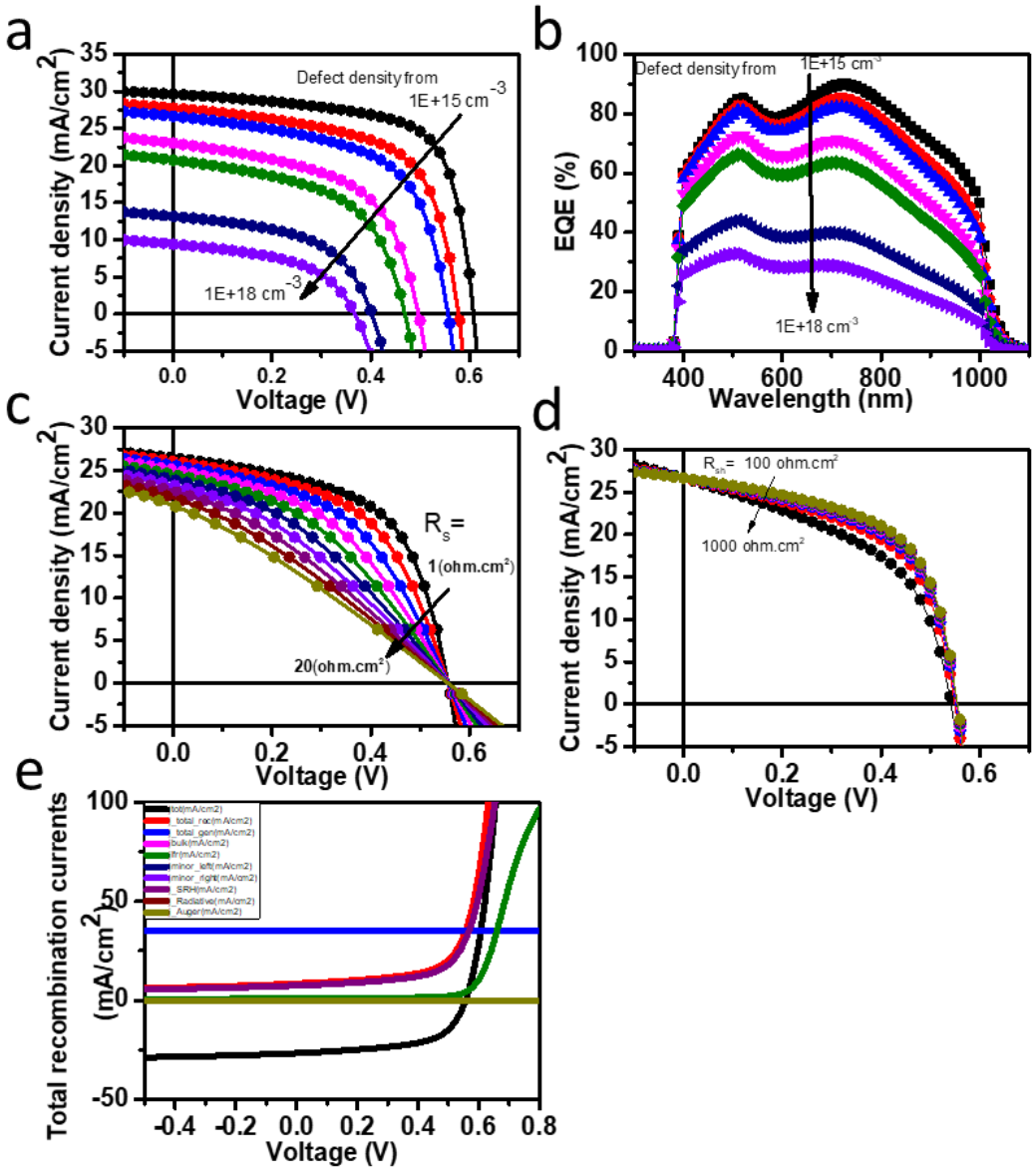

Figure 4- 7: SCAPS simulation results. Variation of (a) J-V curve/parameters, (b) EQE while changing the defect density from 1E+15 cm^{-3} to 1E+18 cm^{-3}. Variation of J-V curve while changing (c) series resistance from 1 to 20 $\Omega.cm^2$ (d) shunt resistance from 100 to 1000 $\Omega.cm^{2,}$ and (e) total recombination currents.

4.3.2 Defect Passivation of Vertically Oriented Sb_2Se_3 Films

Defect passivation is particularly important for the vertically oriented Sb_2Se_3 films prepared by the seed layer templated growth. We carried out a series of post-deposition annealing experiments in ambient air to study the impact of annealing temperature on the film properties and device performance. The SEM morphological analysis shows that increasing the annealing temperature can significantly modify the surface morphology of Sb_2Se_3 **(**Figure 4- 8**)**. High contrast white patches appeared on the surface of the Sb_2Se_3 films after annealing at above 325 °C in ambient air. Increasing annealing temperature leads to a higher density of the white patches and eventually the formation of many prism-shape grains at 375 °C. These structures are speculated to be associated with Sb_2O_3, which has a cubic crystal structure. Although the oxide phase was not resolved in the XRD measurement of the air-annealed films **(**Figure 4- 9**)**, likely due to the small quantity of oxides below the detection limit of the instrument, the formation of the oxide-rich surface is evidenced by the EDS results, where the O to Se ratio increases with increasing the annealing temperature **(**Table 4- 4**)**. The atomic percentage of O is much higher at the point of white patches than on the grain **(**Figure 4- 10**)**. Post-deposition annealing in the air significantly changes the electrical properties of the Sb_2Se_3 films. The conductive atomic force microscopic (C-AFM) analysis revealed that GBs of vertically orientated Sb_2Se_3 grains are generally more resistive than grain interiors **(**Figure 4- 12**a-d)**. The corresponding AFM morphological images are shown in Figure 4- 11. Such prominent characteristics are attributed to the lower charge carrier densities at the GBs, suggesting a self-passivation behavior on the sides of 1D $(Sb_4Se_6)_4$ ribbons. The film annealed at 350

°C in the air **(**Figure 4- 12**b)** exhibits more uniform and slightly lower electrical conductivity across the film than the as-prepared film **(**Figure 4- 12**a)**. The measurements were performed in the dark, a reduced conductivity indicates a lower leakage current. It is also noted that some selenium particle remains on the top of the as-prepared film (Figure 4- 12**a**, red circles), which hinder the local photocurrent generation and collection. The air annealing process removes the excess Se particle on the top of the film **(**Figure 4- 12**b)**, enabling a better heterojunction quality and a higher photocurrent. Additionally, the formation of oxides on the surface helps passivates the Sb_2Se_3 films.

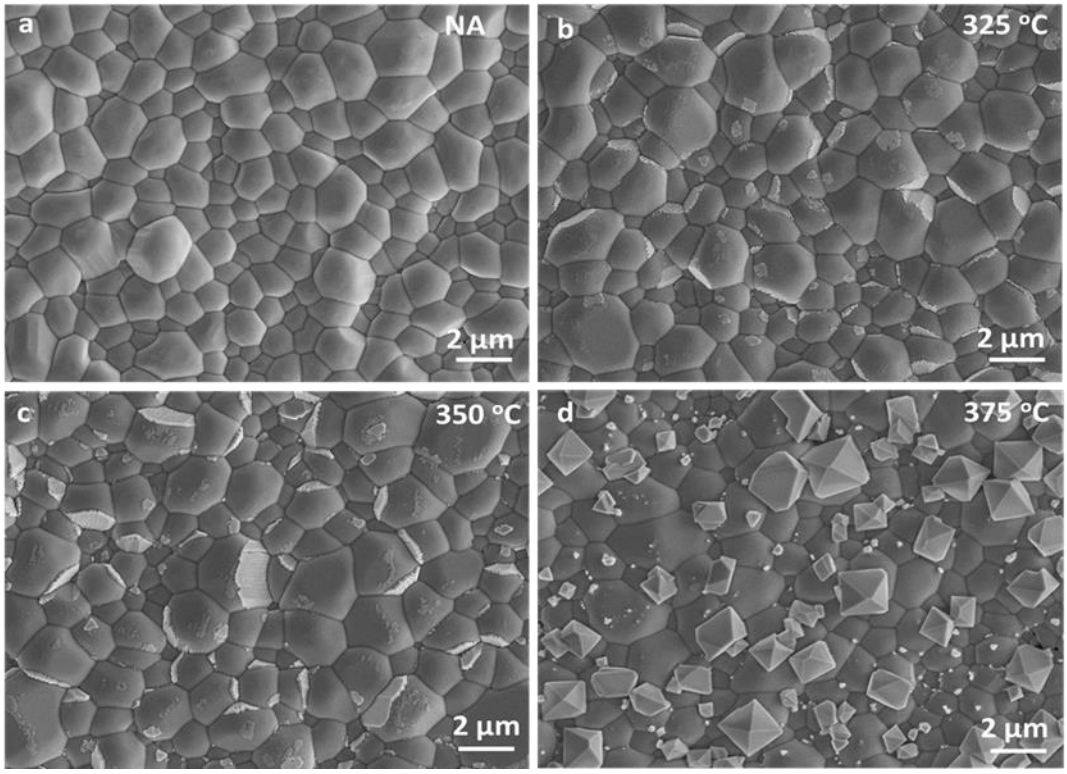

Figure 4- 8: Morphology of Sb_2Se_3 thin films without and with annealing in air at different temperatures. (a) without annealing (NA), (b) annealing at 325 °C, (c) annealing at 350 °C, and (d) annealing at 375 °C.

Table 4- 4:EDS analysis of Sb_2Se_3 absorber layer annealed at different temperatures in the ambient environment.

Annealing (°C)	O (Atomic %)	Sb (Atomic %)	Se (Atomic %)	Se:Sb
NA	3.46	40.25	56.29	1.39
325	4.54	39.75	55.71	1.4
350	6.64	39.23	54.13	1.38
375	16.66	36.45	46.89	1.29

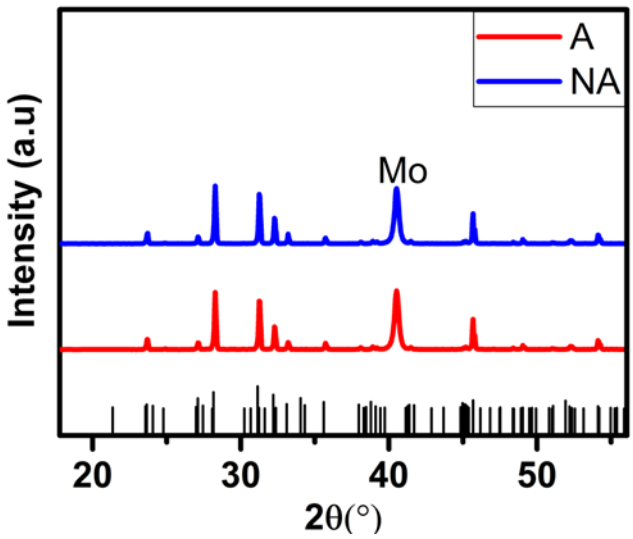

Figure 4- 9: XRD for annealing and non-annealing samples. No oxides' peaks are observed in the XRD patterns.

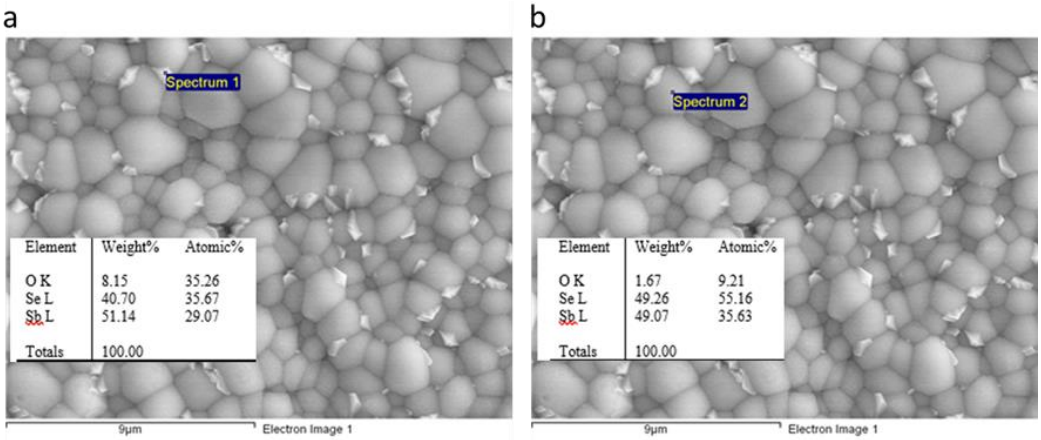

Figure 4- 10: EDS results at two different locations. (a) at the point of white patches and (b) at a grain.

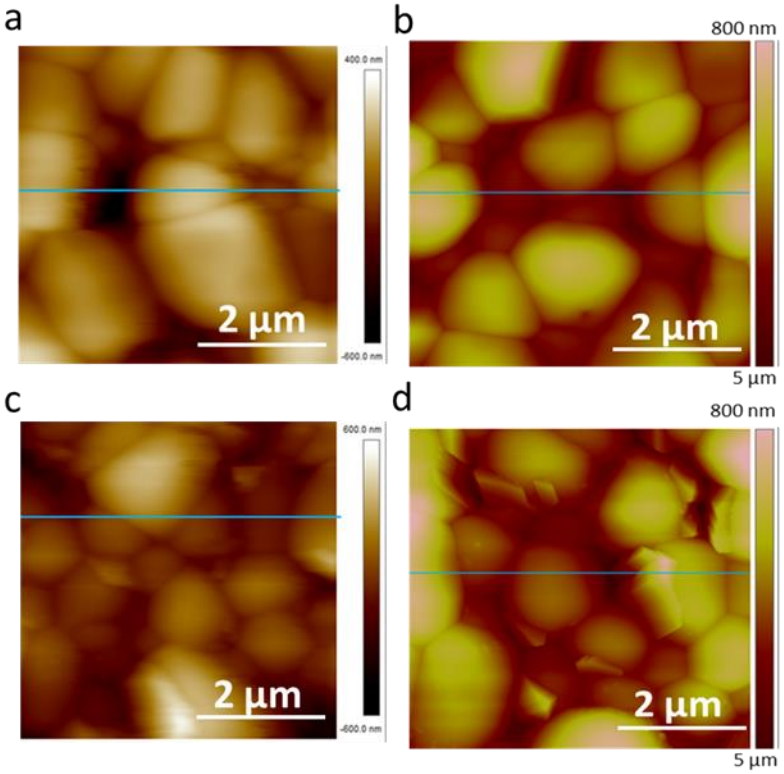

Figure 4- 11: AFM images of Sb_2Se_3 films at different conditions. (a,b) without annealing and (c-d) corresponding annealing films.

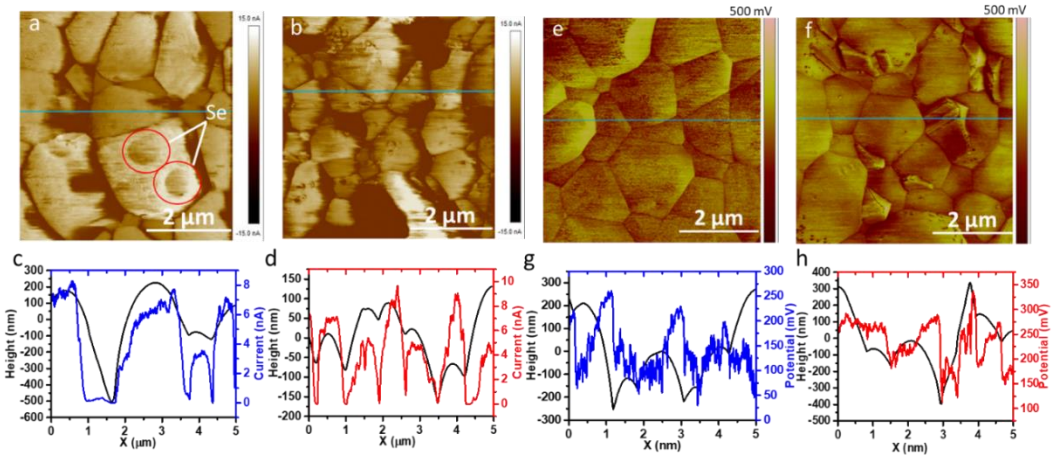

Figure 4- 12**:**c-AFM and KPFM analysis of the Sb_2Se_3 films (a, e) without and (b, f) with air annealing at 350 ^oC. (c, d, g, h) The corresponding height profile and current/ surface potential of the films without and with annealing.

We further used the KPFM characterization to study the surface potential change in the films with and without air annealing. KPFM is a non-contact atomic force microscopy (AFM) method used to measure the surface potential. When we compare the surface potential between the two films, we found that the annealed film exhibits an overall ~100 mV higher surface potential than the as-prepared film **(**Figure 4- 12**e-h)**. The increased surface potential corresponds to a lower work function (closer to the vacuum level), which can be contributed to both a larger downward band bending of the surface space charge region and a smaller electron affinity (χ_e) by the chemical and structural changes after annealing. If the increase in the surface band bending was solely responsible for the decrease in work function (W), the carrier concentration and electrical conduction would reduce to a factor of ~$\exp(-100\ mV/k_BT_r)$=0.02, assuming the mobility of charge carrier did not change significantly, where k_B is Boltzmann constant and T_r room

temperature, respectively. The slight decrease in conductance could not account for the ~100 mV decreases in W and the decrease in χ_e should attribute largely to the W change. This χ_e change could reduce significantly the conduction band offset (CBO) between Sb_2Se_3 and CdS (~360 mV in a spike shape),[90] and benefit the device performance. In addition, the annealing could passivate the defects in both the near-surface region (that would turn to the interface region upon device completion) and in the film bulk. These annealing effects could be beneficial to reducing recombination and enhancing junction quality of the Sb_2Se_3/CdS heterojunction, which plays an important role in improving the PCE of Sb_2Se_3 thin-film solar cells.

To validate the hypothesis that proper air-annealing is beneficial to solar cell performance, we fabricated a batch of devices using Sb_2Se_3 films prepared by the same optimal deposition procedures but post-annealed at different temperatures in air. The statistical comparison of PV parameters of the Sb_2Se_3 devices post-treated under different conditions is summarized in Figure 4- 13. The result shows that 350 °C is the optimal annealing temperature. Figure 4- 14**a** plots the J-V curves for the Sb_2Se_3 champion solar cells without and with air-annealing. The champion cell exhibits a PCE of 8.5%, with a high V_{OC} of 505 mV, a J_{SC} of 27.74 mA cm^{-2}, and a FF of 60.7, significantly outperforming the unannealed device. It is worth noting that the V_{OC} of 505 mV is among the highest reported value for Sb_2Se_3 solar cells **(**Table 4- 1**)**. A high V_{OC} is attributed to the desired Sb_2Se_3 crystal orientation, surface defect passivation, and better junction quality, consistent with the above-mentioned characterization results. Additionally, the EQE analysis **(**Figure 4- 14**b)** shows better spectral responses at the longer wavelengths (700 to 1000 nm) after annealing in air, indicating the reduced SRH recombination and a long carrier lifetime.

Despite the increased V_{OC} and $J_{SC,}$ we observed a slightly reduced FF, mainly due to the formation of oxides on the surface of the absorber layer. The formation of a resistive layer at the front interface leads to an increment in the R_S, although R_{SH} is slightly better due to the passivation of the absorber layer **(**Table 4- 5**)**. Further optimization of this air-annealing process to balance the passivation and increased resistance will boost the PCE of the solar cells.

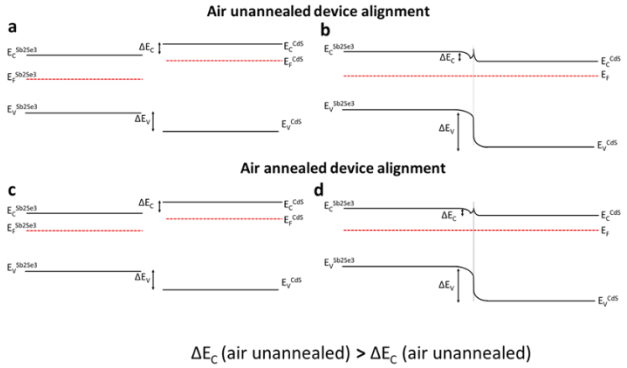

Figure 4- 13: Schematic diagram of Band alignment diagram at CdS/Sb_2Se_3 heterojunction interface before and after air annealing. (a,b) before air annealing and (c,d) after air annealing.

Note: E_v= Conduction band, E_f= Fermi energy level, E_v= Valance band, ΔE_c= Conduction band offset, ΔE_c= Valance band offset

Table 4- 5: Device performance parameters of champion Sb_2Se_3 solar cells with and without air annealing

Samples	V_{OC} (mV)	J_{SC} (mA/cm^2)	Fill Factor (%)	Efficiency (%)	R_S ($\Omega * cm^2$)	R_{SH} ($\Omega * cm^2$)
NA	459	26.54	61.39	7.47	3.813	310.74
A	505	27.74	60.7	8.5	4.09	315.4

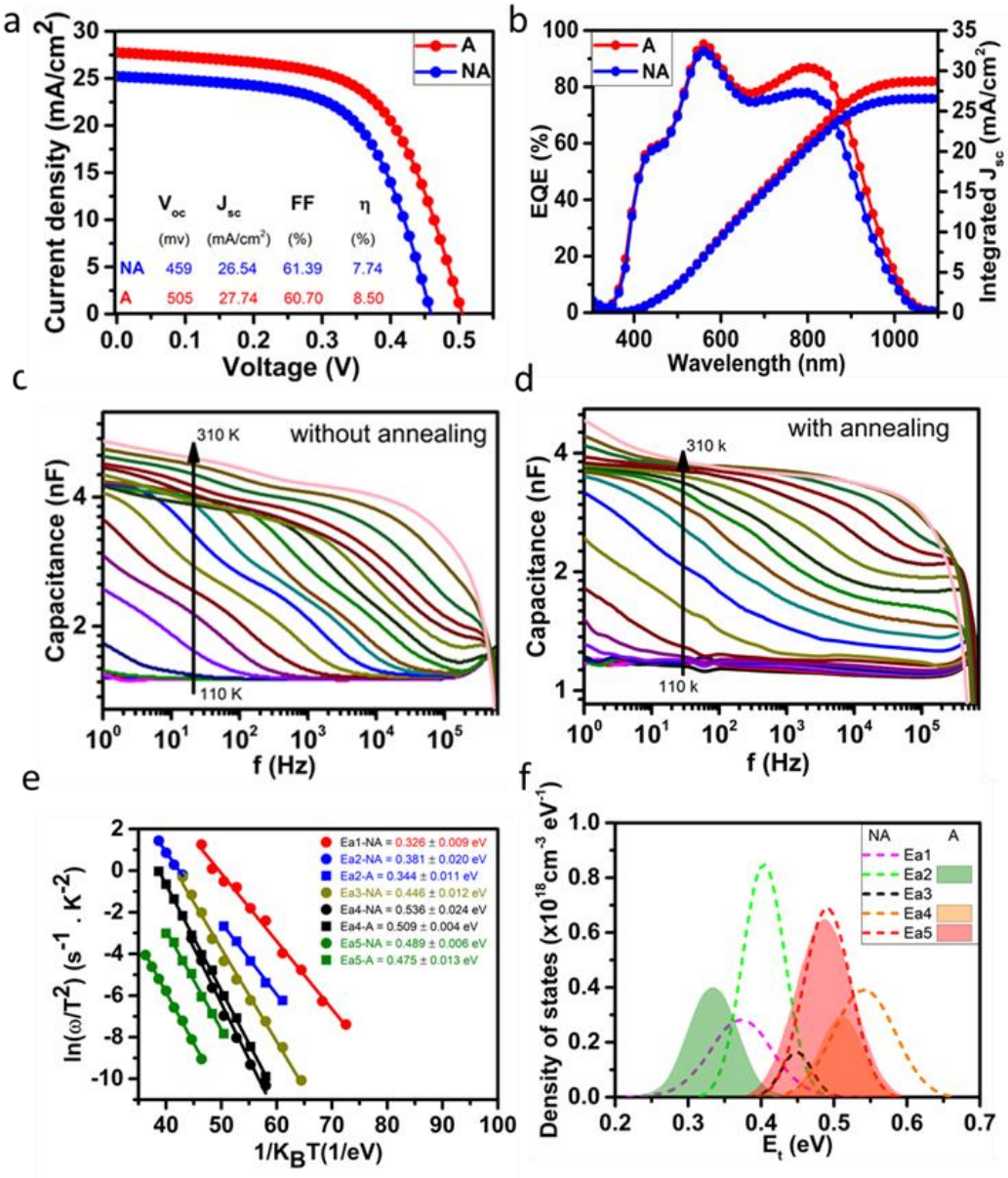

Figure 4- 14**:** (a) J-V and (b) EQE curves of Sb_2Se_3 solar cells, with (A) and without (NA) air annealing. Temperature-dependent admittance spectra measured under dark equilibrium and temperature from 110 – 300 K with 10K temperature step size of Sb_2Se_3 solar cells, (c) with and (d) without air annealing, their corresponding (e) Arrhenius plots, and (f) defect distribution of the two devices.

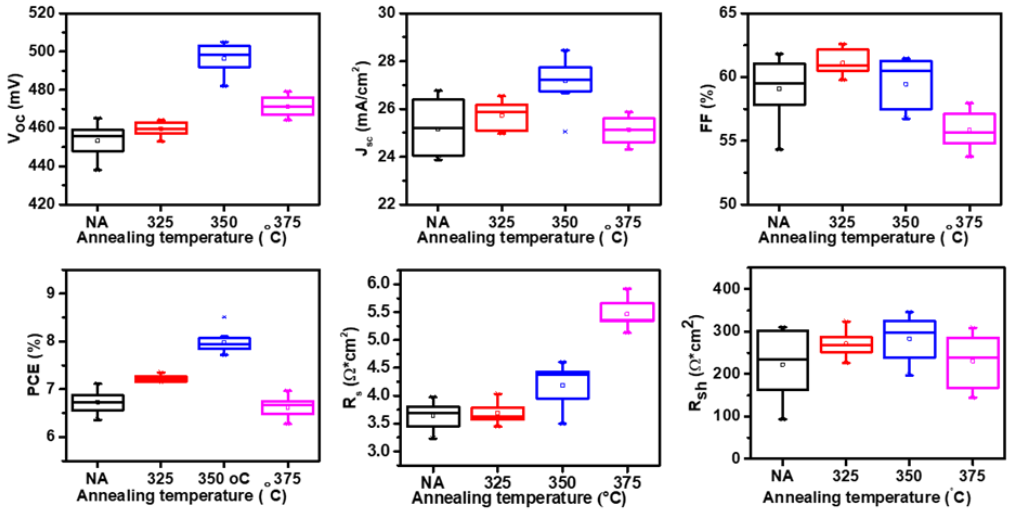

Figure 4- 15: Statistic distributions of PV parameters for Sb_2Se_3 solar cells with the Sb_2Se_3 absorber layers annealed at different temperatures of NA, 325, 350, 375 °C.

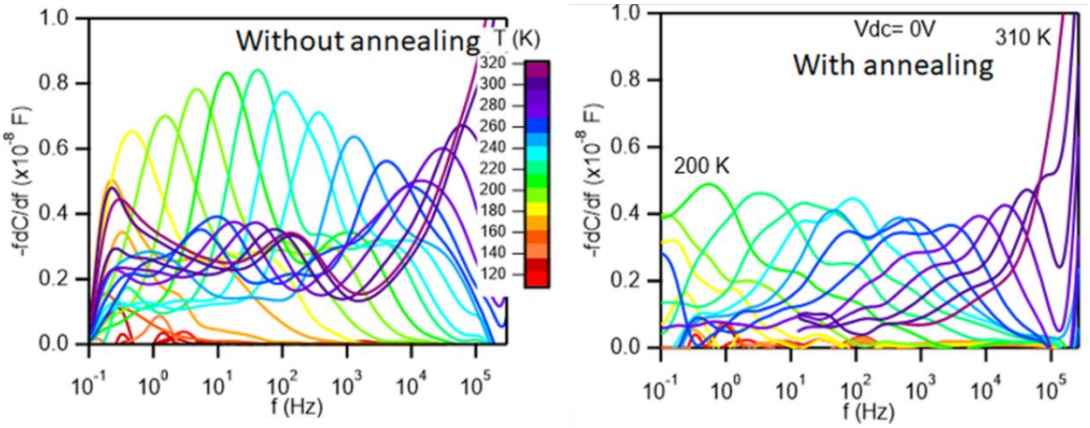

Figure 4- 16: Differential capacitance spectra (-fdc/df) extracted from the capacitance spectra Figure 5 (c,d) for (a) without annealing and (b) with annealing, Sb_2Se_3 devices.

To better understand the origins of improved device performance, we conducted temperature-dependent admittance spectroscopy (TAS) measurement to study the defect properties of Sb_2Se_3 in the solar cells **(**Figure 4- 14**c-f)**. Temperature-dependent admittance (C-f-T) spectroscopy measurements were done in the temperature ranging from 110 to 310

K on our champion devices to reveal the distribution of defects as well as the defect-induced carrier recombination mechanism. Figure 4- 14**c, d** shows the C-f-T spectra for our devices without and with annealing. Figure 4- 15 shows the differential capacitance spectra, in which the thermal activation energy is calculated by using the following equation[91]:

$$\omega_0 = A_0 T^2 \exp\left[-\frac{E_a}{k_B T}\right] \ldots\ldots\ldots\ldots\ldots\ldots\ldots\ldots\ldots\ldots\ldots\ldots\ldots\ldots (2)$$

where ω_0 is the characteristic transition frequency, T is the absolute temperature, k_B is the Boltzmann constant, A_0 is a pre-exponential factor independent of temperature, and E_a is the defect activation energy of the capacitance signature seen in admittance spectra. The characteristic transition frequency of each capacitance signature has been determined from the peak of the differential capacitance spectra **(**Figure 4- 16**a-b)** to construct Arrhenius plots **(**Figure 4- 14**e)**. Based on equation 2, the characteristic activation energy is calculated from the linear fit of Arrhenius plots. Five characteristic activation energies; Ea1-NA, Ea2-NA, Ea3-NA, Ea4-NA, and Ea5-NA, were obtained for the samples without annealing, whereas three characteristics activations energies; Ea2-A, Ea4-A, and Ea5-A, were obtained for the samples with annealing **(**Figure 4- 14**e)**. These activation energies are listed in Table 4- 6.

Table 4- 6: Activation energy and the integrated trap densities of non-annealed and annealed samples.

Activation energy (eV)			**tDOS (cm^{-3})**	
	NA	**A**	**NA**	**A**
Ea1	0.326	NA	3.04E+17	NA
Ea2	0.446	NA	8.57E+16	NA
Ea3	0.381	0.344	6.07E+17	03.54E+17
Ea4	0.536	0.475	4.09E+17	2.23E+17
Ea5	0.489	0.475	5.49E+17	6.28E+17

Figure 4- 14**f** shows the defect distribution of each defect type, in which the defect energy distribution ($E_t(\omega)$) with respect to the valence band and the defect density of states ($N_t(E(\omega))$) were obtained by the following equations [91] :

$$E_t(\omega) = E_a - k_B T \ln\left(\frac{\omega_0}{\omega}\right) \quad \text{.....(3)}$$

$$N_t(E(\omega)) = \frac{V_{bi}}{qWk_BT}\left(-\omega\frac{dC}{d\omega}\right) \quad \text{.....(4)}$$

where V_{bi} is the built-in potential of the p-n junction, ω is the angular frequency, and W is the depletion width that is extracted from the capacitance-voltage measurements using Mott-Schottky analysis. Then the energetic distribution of the defect density of states was obtained by the Gaussian fit. Table 4- 6 lists the calculated density of states for each defect.

Table 4- 7: Defects capture cross-section of non-annealed and annealed samples.

Activation energy	**Attempt-to-escape-frequency (Hz)**		**Capture cross section (cm^2)**	
	NA	**A**	**NA**	**A**
Ea1	1.482E+11	NA	1.482E-14	NA
Ea2	1.655E+12	NA	1.655E-13	NA
Ea3	21.452E+11	3.414 E+11	1.452E-14	3.410E-15
Ea4	1.062E+13	5.169E+12	1.062E-12	5.169E-13
Ea5	1.298E+11	1.421E+11	1.298E-15	1.421E-14

Sb_2Se_3 thin films can have different point defects based on two growing conditions: (i) Se-rich condition and (ii) Se-poor condition. Under the Se-poor condition, two detrimental donor defects Sb_{Se} and V_{Se} are easily formed, whereas Se_{Sb}, $Se_{i,}$ and V_{Sb} defects are formed under the Se-rich condition.[29] According to the EDS analysis **(**Table 4- 4**)**, our devices are slightly Se-poor. Therefore, we expect that Sb_{Se} and V_{Se} are major defects in our Sb_2Se_3 films. [22, 29, 92, 93]From the density functional theory (DFT) studies, the deep defects, Ea3 (0.446 eV), Ea4 (0.536 – 0.507 eV) and Ea5 (0.489 – 0.475 eV) are likely associated with Sb_{Se} and V_{Se} defects, respectively.[29] The two relatively shallow defects with activation energies of Ea1 (0.326 – 0.344 eV) and Ea2 (0.350eV) are likely related to the V_{Sb}, Se_i, and other acceptor defects with different oxidation states, which are formed due to the stoichiometric inhomogeneity in the polycrystalline film.[29, 92, 93]

Comparing the activation energy and defect distribution for unannealed and annealed Sb_2Se_3 devices, we found that the total number of defect levels was reduced from

five to three, the total defect density of all levels was decreased by ~ 38%, and defect activation energies were lower after air annealing, indicating that some of the defects are completely and partially passivated, and others become shallower. The reduced defect densities and lower defect energy levels are mainly attributed to the oxygen passivation on the defects because oxygen can fill V_{Se} and form bonding with both under coordinated Sb and Se atoms. We also compared the defect capture cross-section of the two samples **(**Table 4- 7**)**. The annealing device exhibits a lower capture cross-section valve compared with the unannealed one, indicating reduced recombination in the absorber layer. Such defect passivation is beneficial to the PV performance of the devices.

To determine if the defects are bulk or interface defects, TAS measurements were performed at various DC biases with a constant AC modulation. When the activation energy varies with DC bias, the defect is an interface defect. On the contrary, if the activation energy remains constant with changing the DC bias, the defect is a bulk defect. Figure 4- 17 shows that all the activation energies in both annealed and unannealed samples are bias-independent, suggesting that the charged defects contributing to the carrier transport are located in the bulk of the Sb_2Se_3 absorber. Overall, the TAS measurement results confirm the bulk defects in the Sb_2Se_3 absorber are passivated after the annealing in air.

We also measured the dark J-V curves of the Sb_2Se_3 cells without and with annealing at various temperatures. The annealed cell shows a dark saturation current density (J_0) of 3.14 x 10^{-7} mA cm^{-2} **(**Figure 4- 18**a-b)** which is lower than J_0 of 9.9 x 10^{-7} mA cm^{-2} for the unannealed cells. The reduced J_0 confirms the reduced SRH recombination measured by TAS, enabling a high V_{OC} exceeding 500 mV for the air-annealed device. The

Arrhenius plots of $\ln(J_0/T^2)$ as a function of the reciprocal of the thermal energy **(**Figure 4-18**c)** show the same activation energy ($q\phi$) for both annealed and unannealed devices, indicating no change in the interface barrier in these two devices. This result confirms that the oxygen-assisted defect passivation is mainly impacting the bulk defects while it does not alter the interfacial properties.

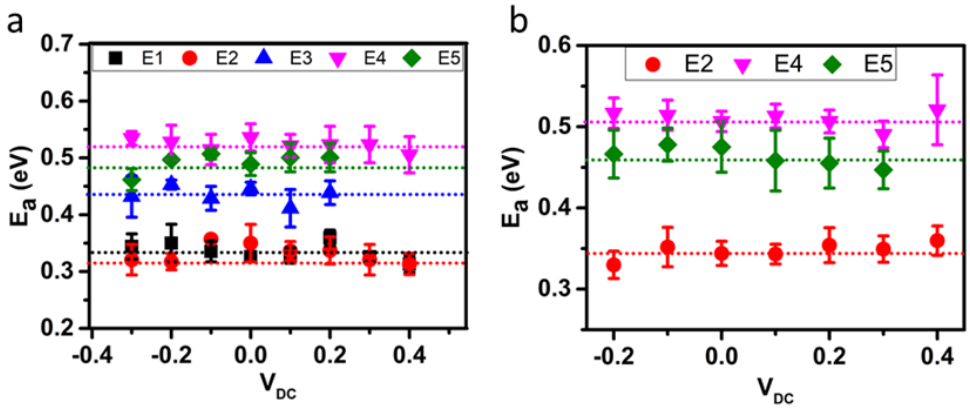

Figure 4- 17:Defect activation energies of Sb_2Se_3 solar cell (a) without, and (b) with annealing as a function of DC bias voltage.

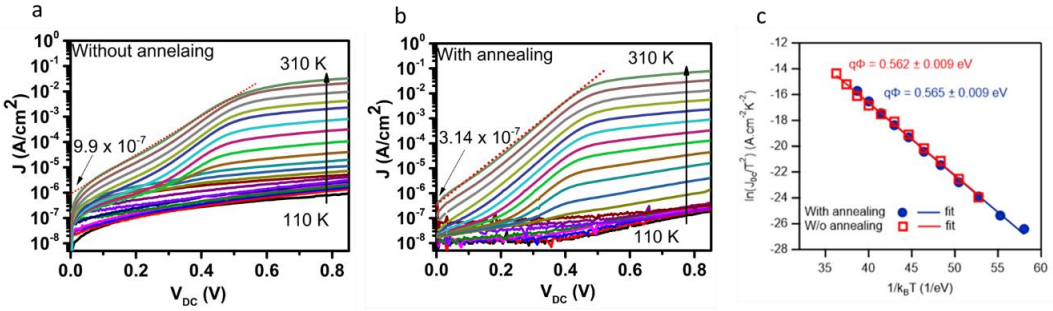

Figure 4- 18:Dark J-V-T curves of the Sb_2Se_3 solar cells (a) without annealing (b) with annealing, and (c) Arrhenius plots formed from the extracted back saturation current density at each temperature to calculate back-contact barrier heights.

4.4 Conclusion

In sum, we investigated the seed layer preparation condition to achieve the templated growth of vertically oriented Sb_2Se_3 films on Mo coated glass substrates. After the optimization of the grain orientation, crystallinity, and rear interface properties, we obtained a champion PCE of 7.47% for substrate-type Sb_2Se_3 solar cells. We then employed post-deposition annealing in the air to passivate bulk defects in the Sb_2Se_3 absorber layer. The air annealing effectively reduces the densities of the defects and lowers their activation energies, resulting in lower J_0 and higher PCE. As a result, our best-performing device after annealing in air delivers a PCE of 8.5%. This work demonstrates a facile and effective approach to preparing high-performance Sb_2Se_3 solar cells.

Chapter 5

Post-annealing Treatment on Hydrothermally Grown Sb2(S, Se)3 Thin Films for Efficient Solar Cells

In this work, we fabricate antimony selenosulfide ($Sb_2(S, Se)_3$) thin-film solar cells by a hydrothermal method followed by a post-deposition annealing process at different temperatures. The effects of the annealing temperature on the morphological and structural properties of the $Sb_2(S, Se)_3$ films are systematically investigated by scanning electron microscopy and X-ray diffraction analyses. We find that a proper annealing temperature leads to a high-quality $Sb_2(S, Se)_3$ film with large crystal grains, proper stoichiometry, and high crystallinity. After optimizing the process, we obtained $Sb_2(S, Se)_3$ solar cells with an improved power conversion efficiency from 2.04 to 8.48%.

5.1 Introduction

Recently, metal chalcogenide and metal halide perovskite thin-film solar cells have achieved significant improvements in power conversion efficiencies (PCEs). Chalcogenide solar cells based on CdTe, $Cu_2(In, Ga)Se_2$ (CIGS), and metal halide perovskite hold PCE records of more than 22.1%, [43] 23.35%, [94] and 25.2%, [13] respectively. However,

due to the scarcity of rare elements like Te, In, and Ga, and the toxicity of Cd and Pb, researchers are looking for other alternatives.[19] Thanks to appealing properties like environmental friendliness, low toxicity, and earth abundancy, antimony chalcogenides have come out as a promising absorber material for photovoltaic applications.[95] Binary compounds like antimony selenide (Sb_2Se_3), antimony sulfur (Sb_2S_3), and mixed chalcogenide antimony selenosulfide, $Sb_2(S, Se)_3$, have been a unique one-dimensional crystal structure featuring electrically benign grain boundaries if they are oriented in the proper directions.[9, 25] Additionally, $Sb_2(S, Se)_3$ has a tunable bandgap of 1.03-1.8 eV, depending on the S/Se ratio, outstanding absorption coefficients ($\sim 10^5\,cm^{-1}$), and excellent material stability.[31, 41]

The performance of the heterojunction antimony-based chalcogenide thin-film solar cells strongly depends on the quality of the absorber materials. The desired qualities of the absorber are high crystallinity, larger grain size, suitable bandgap, and preferable electrical transport properties. The deposition method and other treatments largely determine the quality of the absorber layer. Antimony-based solar cells can be fabricated through different routes, including solution process,[96, 97] physical vapor deposition (PVD),[98] sputtering,[63, 86] chemical bath deposition (CBD),[99] hydrothermal approach, [31, 39, 50] and closed space sublimation (CSS)[9, 24, 25] and they have their corresponding drawbacks like amorphous phase, non-uniformity, off stoichiometry, poor morphology with abundant pinholes and voids, and expensive fabrication costs. In this regard, a hydrothermal method could be useful to solve some of the above problems like the quality, homogeneity, and cost of fabrication. However, a hydrothermal approach is typically limited by low energy input during the film growth, resulting in low crystallinity

and relatively high defects density in the absorber and increasing the recombination in bulk and at the interfaces. Despite these drawbacks, $Sb_2(S, Se)_3$ solar cells have shown a promising efficiency of 10.7%,[100] though it is still much lower than the theoretical limit of >30%.[28] With the past experience with the Sb_2Se_3 and Sb_2S_3 materials, advancing deposition methods,[34, 38] doping engineering,[52, 53] and post-deposition annealing[9, 25] treatments under different environments could be helpful to improve the film quality of $Sb_2(S, Se)_3$ solar cells. Among them, post-annealing treatments are found to be one of the effective methods for improving Sb_2Se_3 and Sb_2S_3 solar cells.[9, 24] Post-annealing treatment is the first treatment we do after fabricating the absorber layer through any solution method. So, it is one of the important steps while fabricating the solar cell. Usually, post-annealing treatments release the internal stress of the film, reduce internal defects, and promote compactness and crystallization.[35] There are some studies on post-annealing treatments on $Sb_2(S, Se)_3$ thin-film solar cells. Wang et al. studied the post-selenization effect on $Sb_2(S, Se)_3$ solar cells fabricated by a hydrothermal method.[39] After optimizing the S/Se ratio and post-annealing temperature, Tang et al. realized a PCE of 10% for $Sb_2(S, Se)_3$ solar cells.[31] Further, Zhao et al. studied the effect of an alkaline metal fluoride treatment on $Sb_2(S, Se)_3$ films and an annealing process to regulate energy band alignment, which helps enhance the PCE of $Sb_2(S, Se)_3$ solar cells to 10.7%.[100]

In this work, we fabricate $Sb_2(S, Se)_3$ thin films using the hydrothermal method and systematically investigate the effect of post-annealing temperature on the composition, morphology, phase, defects, optical properties, and surface potential of the films. Additionally, we assess the device performances and the mechanism of the efficiency loss in detail. $Sb_2(S, Se)_3$ thin films were found to have uniform surface morphology, larger

crystal grains, and proper stoichiometry after annealing at an optimal annealing temperature of 350 ^{o}C, leading to a champion PCE of 8.48% in our superstrate type solar cells.

5.2 Experimental Details

The $Sb_2(S, Se)_3$ thin films were deposited onto the CdS coated FTO glass substrates by a hydrothermal method. The CdS layer was first deposited by a CBD approach, following the previously reported method.[38] Afterward, the obtained CdS film was annealed in ambient air at 400 ^{o}C for 10 min. For the $Sb_2(S, Se)_3$ deposition, potassium antimony tartrate ($C_8H_4K_2O_{12}Sb_2 \cdot 3H_2O$), sodium thiosulfate pentahydrate ($Na_2S_2O_3 \cdot 5H_2O$), and selenourea (CH_4N_2Se) were used as Sb, S, and Se sources, respectively. 20 mM of $C_8H_4K_2O_{12}Sb_2. \cdot 3H_2O$, 40 mM of $Na_2S_2O_3 \cdot 5H_2O$, and 35 mg of CH_4N_2Se were mixed in 50 ml of DI water.[39] The mixed solution was stirred until it turned clear and homogenous faint yellowish. Then, the solution was transferred into the cleaned inner Teflon tank of an autoclave. During the synthesis, the substrate was placed in such a way that the CdS layer faced downward. Finally, the tight autoclave with the solution was kept in an oven heated at 130 ^{o}C for 3 h.

The autoclave was taken out of the oven and allowed to cool to room temperature Then, the films were taken out from the autoclave and dried by blowing N_2 gas. Afterward, the films were loaded inside the tube furnace on the graphite plate and the tube was vacuumed till we get the pressure of 3 mT. Then, we annealed the samples in two-step processes. First, we heated the graphite plate, which holds the samples, at 100 ^{o}C using the IR heater from the top and bottom sides for one minute. This first step of heating is done

to remove the water or any other solvent remaining on the film. Then finally, we fill the tube with 10 T of N_2 gas and heated the films at different temperatures i.e 300, 350, and 400 ^oC for 10 minutes. After 10 minutes of heating, the films were allowed to cool down to room temperature.

Finally, we prepared a device in a superstrate configuration: FTO/CdS/$Sb_2(S, Se)_3$/Spiro-OMeTAD/Au. We used Tec-12D FTO glass substrate from Pilkington North America Inc. The Spiro-OMeTAD was used as a hole transport layer (HTL). HTL solution was made by a Spiro-OMeTAD (LUMTEC)/chlorobenzene (91 mg/ 1 ml) solution with an additive of 21 µl of Li-bis(trifluoromethanesulfonyl) imide (Li-TFSI)/acetonitrile (540 mg/ 1 ml), 35 µl of 4-tert-butylpyridine (TBP) and 9 µl of tris(2-(1H-pyrazol-1-yl)-4-tert-butylpyridine)-cobalt(III) tris(bis(trifluoromethylsulfonyl)imide (FK 209)/acetonitrile (376 mg/1 ml) . After that, a spiro-OMeTAD film was spin-coated on the $Sb_2(S, Se)_3$ film at a speed of 2500 rpm for 30 sec then the film was left overnight to get oxidized. Finally, Au was deposited on the top of Spiro as a back contact electrode using a thermal evaporator under a pressure of 5 x 10^{-6} Torr, where a mask of 0.08 cm^2 was used.

5.3 Results and Discussions

The microscopic surface images of the $Sb_2(S, Se)_3$ thin films post-annealed at different temperatures are shown in Figure 5- 1. The as-deposited film (Figure 5- 1) consists of small, rounded grains. After annealing the $Sb_2(S, Se)_3$ films, the grains merge and grow, and the crystalline facet or edge starts to appear clearly. However, increasing the annealing temperature leads to non-uniform morphology and the formation of microcracks at boundaries. At the annealing temperature of 400 ^oC, the number of cracks and pinholes

increases significantly. The cracks and pinholes in the films are likely due to the evaporation of the volatile elements from the films, which alters the composition. These cracks and pinholes can act as recombination centers and shunting paths in solar cells, which lower the performance of the devices. The SEM surface images show that the $Sb_2(S, Se)_3$ film annealed at 350 ^oC for 10 min has the highest quality with large grains and is free of cracks and pinholes.

X-ray diffraction (XRD) was used to study the influence of annealing temperature on the phase and structure of the $Sb_2(S, Se)_3$ thin film. The XRD pattern of the as-deposited thin film (Figure 5- 2) shows amorphous in nature, with no peaks belonging to $Sb_2(S, Se)_3$. However, annealing the films converted them from amorphous to the polycrystalline phase. It is known that the intensity of an XRD peak is directly proportional to the crystallinity of the crystal. The film annealed at 400 ^oC has the highest XRD peak intensity among the films annealed at 300, 325, 350, 375, and 400 ^oC, indicating the highest crystallinity. Though the crystallinity of the film can be increased with a higher annealing temperature, the quality of the PN junction is likely to deteriorate due to the cracks and pinholes in the film.

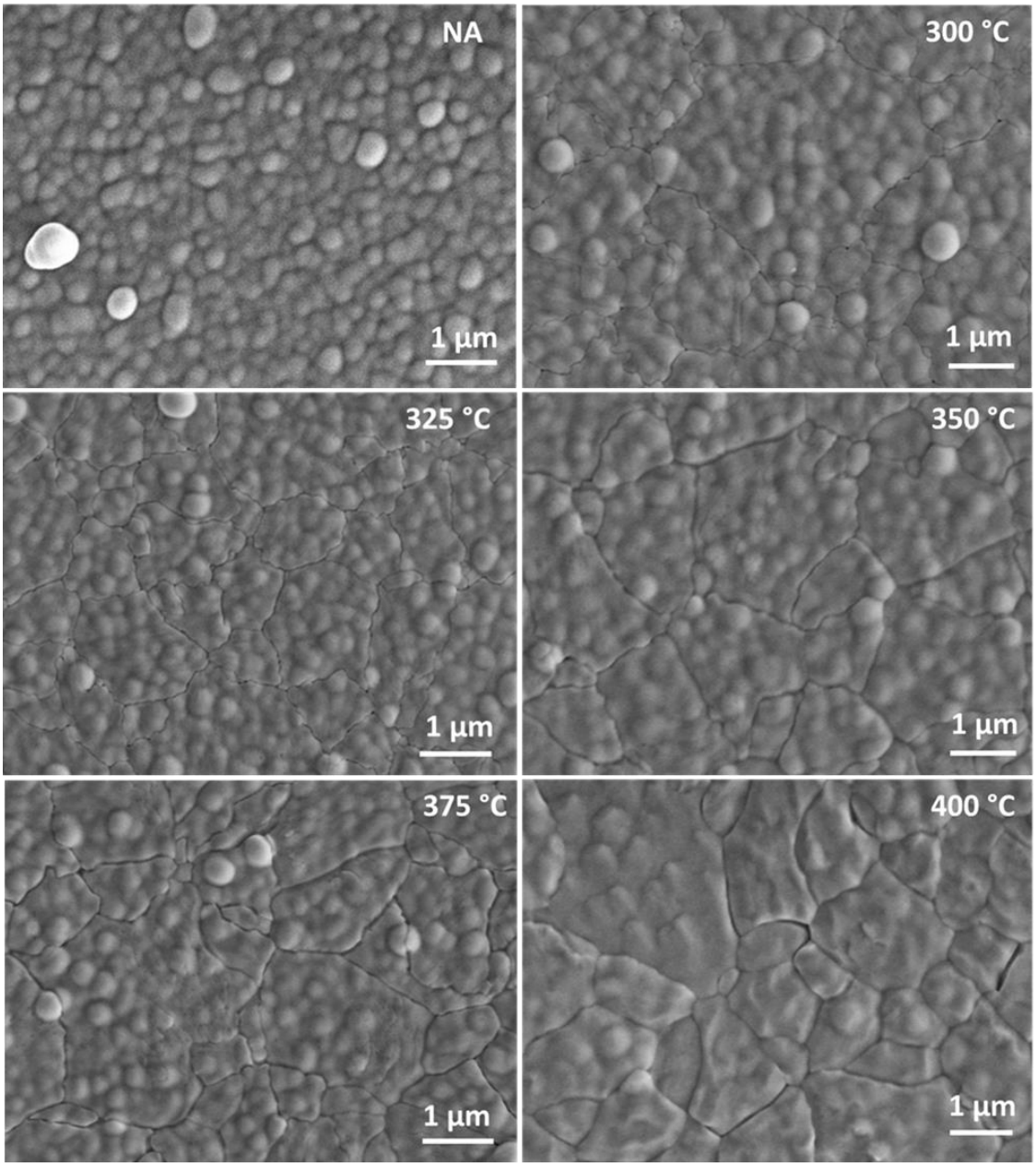

Figure 5- 1: Top-view SEM images of $Sb_2(S, Se)_3$ thin films (a) without annealing and annealed at different temperatures: 300 ^oC, 325 ^oC , 350 ^oC ,375 ^oC, and 400 ^oC .

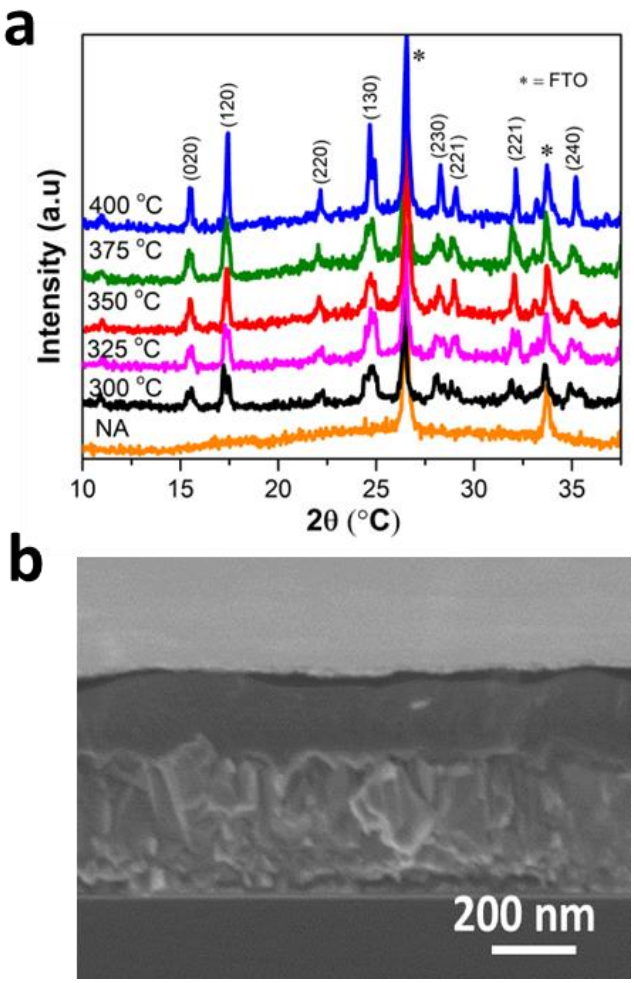

Figure 5- 2: XRD patterns of $Sb_2(S, Se)_3$ thin films annealed at various temperatures. (b) Cross-sectional SEM image of a $Sb_2(S, Se)_3$ film annealed at 350 ^oC.

Figure 5- 4 show the current density-voltage (J-V) and the external quantum efficiency (EQE) curves of the champion $Sb_2(S, Se)_3$ solar cells annealed at different temperature. The corresponding PV parameters are summarized in Table 5- 1. The best PCE of 8.48 % was obtained in the solar cell annealed at 350 ^oC. The values of J_{SC}, V_{OC}, FF, R_S, and R_{SH} are 20.44 mA/cm^2, 670 mV, 62.06 %, 3.72 Ω·cm^2, and 642 Ω·cm^2, respectively. All the device parameters of the device annealed at 350 ^oC are significantly

higher than those of the devices annealed at 300 and 400 °C, which is attributed to the higher film quality with better crystallinity and improved morphology, as verified by the XRD and SEM analyses. An increase in V_{OC} from 466 to 670 mV is solely due to the improvement in the film quality as there is no significant change in the bandgap energy (Figure 5- 3) among films annealed at three different temperatures. The inferior performance of the devices annealed at a lower temperature (300 °C) is likely caused by lower crystallinity, higher recombination, and poorer photoexcited charge collection. The devices annealed at a higher temperature (400 °C) suffer from more severe shunting, likely caused by the microcracks and pinholes. The EQE value of the device annealed at 350 °C is significantly higher in all wavelength ranges than that of the other two. It is noted that the EQE value of the device annealed at 300 °C is lower at the longer wavelengths after the peak at 400 nm, indicating very poor crystallinity and low diffusion length of the film.

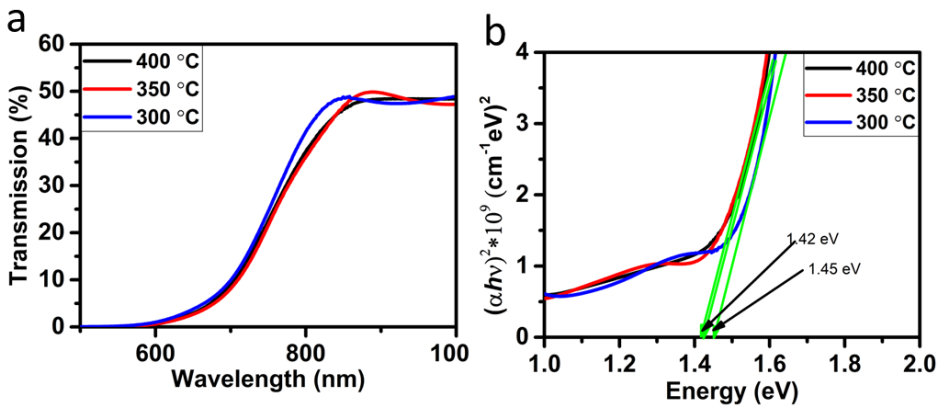

Figure 5- 3: (a) Transmittance spectra and the Tauc plot of the $Sb_2(S,Se)_3$ thin films annealed at different annealing temperatures.

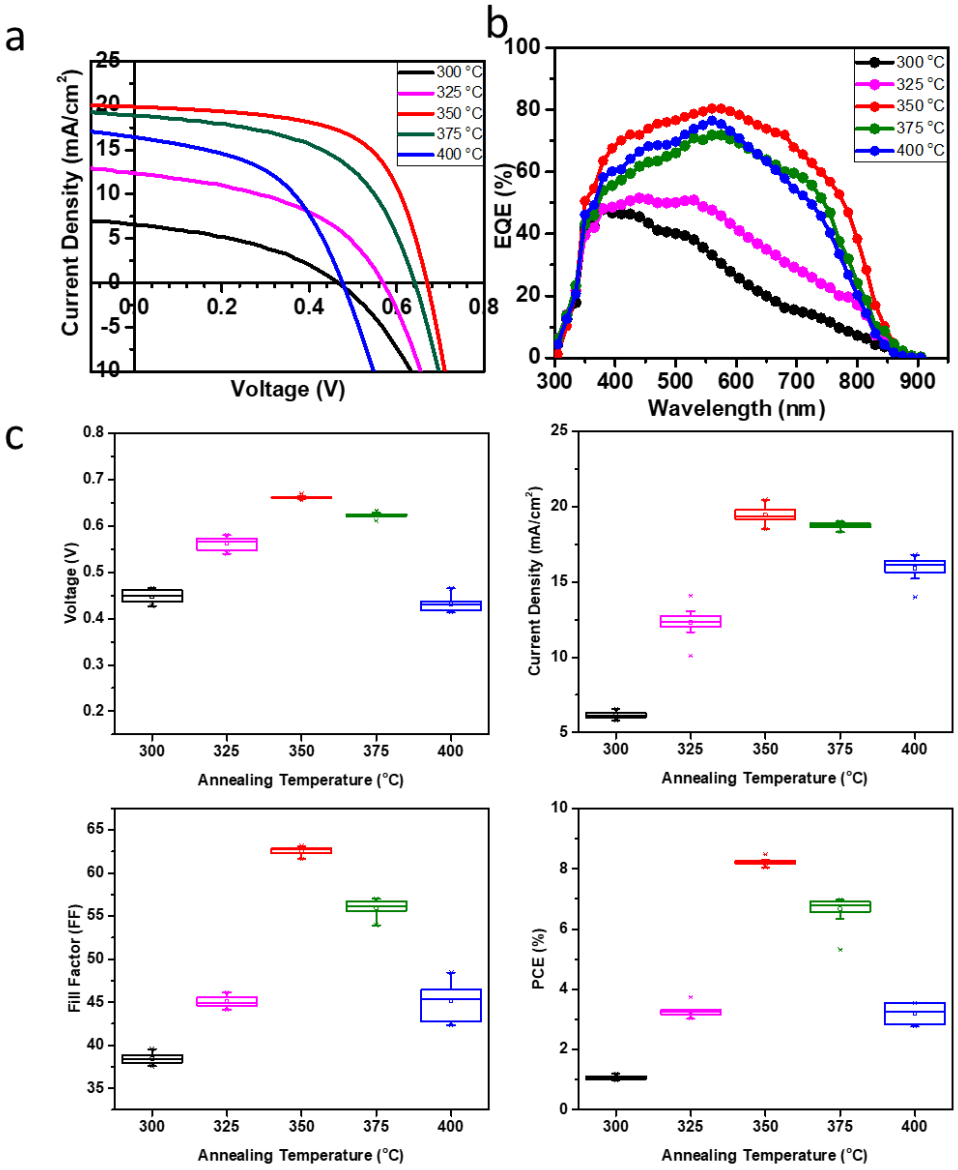

Figure 5- 4: (**a)** Current density-voltage (J-V), (**b)** external quantum efficiency (EQE) curves and (**c**) Statistical distributions of (c) V_{OC}, (d) J_{SC}, (e) FF, and (f) PCE of $Sb_2(S,Se)_3$ solar cells at different annealing temperatures.

Table 5- 1: J-V parameters of champion Sb_2Se_3 solar cells annealed at different temperatures.

Annealing Temp. (°C)	**V_{OC} (mV)**	**J_{SC} (mA/cm²)**	**FF (%)**	**PCE (%)**	**R_S (Ω·cm²)**	**R_{SH} (Ω·cm²)**
300	466	6.57	39.30	1.20	31.37	229.54
325	569	12.36	45.50	3.20	14.05	281.16
350	670	20.44	62.06	8.48	3.72	642.80
375	611	17.95	53.93	6.51	8.71	428.19
400	468	16.95	48.44	3.84	17.19	171.88

The defect properties of the $Sb_2(S, Se)_3$ solar cells were studied by using temperature-dependent admittance spectroscopy (TAS), which helps to understate how the post-annealing temperature improves the device performance. The temperature varied from 150 to 300 K on our champion devices while doing the temperature-dependent admittance (C-f-T) measurement. Figure 5- 5 shows the C-f-T spectra of our devices which were annealed at 300, 350, and 400 °C. The thermal activation energy is calculated by using the following equation:

$$\omega_0 = A_0 T^2 exp\left[\frac{E_a}{k_B T}\right] \text{.....(1)}$$

Where ω_0 is the characteristic transition frequency, T is the absolute temperature, k_B is the Boltzmann constant, A_0 is a pre-exponential factor independent of temperature, and E_a is the activation energy of a signature seen in admittance spectroscopy. We found

two activation energies Ea1(A), Ea2(A), and Ea1(C), Ea2(C) for the samples annealed at 300 ^{o}C and 400 ^{o}C, respectively whereas we got one activation energy Ea2(B) for the samples annealed at 350 ^{o}C while fitting the equation 1.

When we compare the defect activation energies for the samples annealed at different temperatures, we found that the number of defect levels was reduced from two to one when annealed at 350 ^{o}C by reducing all the defect density of all the levels by 50%. While going through the state of art, these calculated defect activation energies can be roughly assigned as antimony antisite (Sb_{Se} or Sb_{S}), sulfur vacancy (V_{S}), and selenium vacancy (V_{Se}). It is not an easy job to separate these defects, therefore, we roughly consider Sb_{Se}, $Sb_{S,}$ and V_{Se} as a controlling defect of our devices. As we know, the defect with higher activation energies has more chances to become a recombination center. The samples annealed at 350 ^{o}C has lower activation energies than samples annealed at the other two temperatures, this indicated some of the defects are completely or partially passivated, and others become shallower. Thus, the samples annealed at 350 ^{o}C has higher device performance due to the lower defect activation energy.

Table 5- 2: EDS results of absorber layers annealed at different temperatures.

Samples	S -Atomic (%)	Se-Atomic (%)	Sb-Atomic (%)
300 ^{o}C	53.94	6.39	39.67
350 ^{o}C	48.65	10.07	41.28
400 ^{o}C	46.11	13.15	40.74

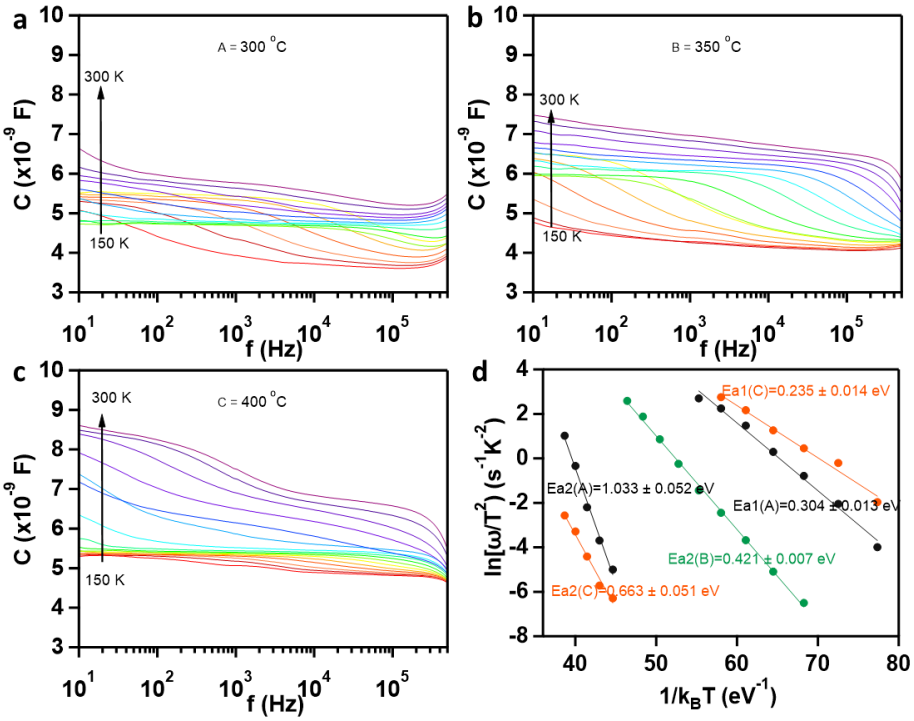

Figure 5- 5: Temperature-dependent admittance spectra measured under dark equilibrium and temperature from 150 – 300 K with 10K temperature step size of $Sb_2(S, Se)_3$ solar cells post at different temperatures. (a) 300 ^oC (b) 350 ^oC (c) 400 ^oC and (d) Arrhenius plot.

We further analyzed the surface potential of the films annealed at different temperatures by using a Kelvin probe force microscopy (KPFM), KPFM is a non-contact AFM method to determine a surface potential, as shown in Figure 5- 6. The surface potential of films annealed at 300, 350, and 400 ^oC are found to be around 1, 1.16, and .79 V respectively. The film annealed at 350 ^oC demonstrate an overall ~ 160 mV higher surface potential than films annealed at other temperature. As, we haven't done any chemical treatment, the change in the surface potential of the films is due to the change in the composition of the absorber while annealing at different temperatures. This change in

composition can be seen in energy dispersive spectroscopy (EDS) results (Table 5- 2). While increasing the temperature, the selenium amount increases while the sulfur goes down as we know the sulfur evaporates at a lower temperature than selenium. Due to the structural and chemical changes after post-annealing treatment, the work function gets lower (closer to the vacuum level) which ultimately increases the surface potential of the film. This lowering to the work function could be due to the larger downward band bending of the surface space charge region and a smaller electron affinity. A lower value of the surface potential indicates the presence of some kind of charged defects on the absorber layer.[101] Here, the films annealed at 350 ^{o}C have higher surface potential than when annealed at 300 and 400 ^{o}C. It means when the film is annealed at 350 ^{o}C, the defects on the absorber layer get neutralized or passivated improving the performance of the solar cell.

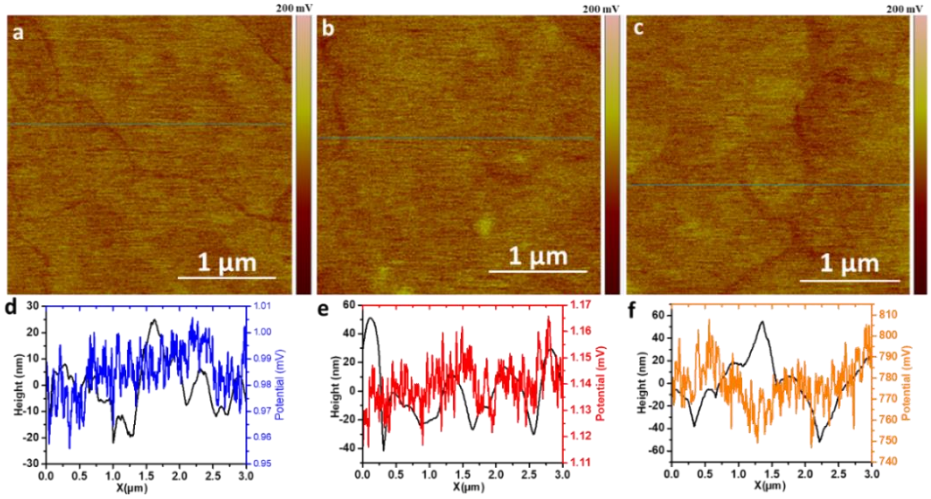

Figure 5- 6: KPFM analysis of the $Sb_2(S, Se)_3$ films annealed at different temperatures. (a) 300 ^{o}C, 350 ^{o}C, and (c) 400 ^{o}C. (d, e, f) The corresponding height profile and surface potential of the films at different temperatures.

5.4 Conclusion

In conclusion, the impact of post-annealing temperature on the PV performance of $Sb_2(S, Se)_3$ solar cells was investigated. We found that the annealing temperature of 350 ^oC was beneficial to increase the grain size, crystallinity, compactness of the films, and passivate the defects. After optimizing the annealing process, we obtained $Sb_2(S, Se)_3$ solar cells with an improved power conversion efficiency from 2.04 to 8.48%. However, there is still much room to improve the performance of the $Sb_2(S, Se)_3$ solar cells prepared by the hydrothermal method.

Chapter 6

Summary and Future Research

6.1 Summary

Antimony chalcogenides are getting much attention from the PV community due to their attractive excellent anisotropic optoelectronic properties. Research on antimony is on a way to be worthy to produce high-efficiency and low-cost production. Within a short period, antimony chalcogenides are showing a promising learning curve and it has a lot of room for improvement. With the new technology and treatment, this material could be one the important material in PV to beat the well-established material like Si and CdTe. Further research on this material to understand the chemistry, physics, device physics and better control over the fabrication and characterization could help to accomplish the goal to produce low-cost, high-efficiency thin-film solar cells with good stability.

This thesis mainly focused on two antimony materials i.e, Sb_2Se_3 and $Sb_2(S, Se)_3$. The thesis covers the fabrication techniques to the characterization in detail to understand the limitations and possibilities of these materials. The study started with the fabrication of the Sb_2Se_3 substrate type solar cell with the role of selenization on its performance. During

the study, we discuss in detail how selenization help to improve the performance of the solar cell. We found that selenization helps to obtain larger crystal grains, uniform surface morphology, desired crystal orientation, proper stoichiometry, and increased carrier density. In addition, we found selenization process helps to compensate for the Se loss during the film deposition, which results in reduced V_{se}-related recombination. With all these benefits we found a significant improvement in the device performance from 1.85% to 6.43%.

We further work on the back interface and front surface to improve the baseline efficiency of 6.43% efficiency. First, we studied the back interface between the Mo and Sb_2Se_3 interface and tried to optimize the orientation of the absorber layer in the preferred direction with the introduction of the seed layer. Here, a seed layer is introduced on a Mo substrate to template the growth of a vertically oriented, columnar Sb_2Se_3 absorber. We found after controlling the grain orientation and the compactness of the seed layer, we obtained the high-quality Sb_2Se_3 absorber layers with passivation of the Sb_2Se_3 interface. After controlling the gain orientation, we found a significant improvement in the device performance, and it could be due to the improvement in the transport of photoexcited charge carriers through the absorber layer and its interface. With the proper orientation of the absorber layer, we were able to enhance the efficiency from 6.4 to 7.4%. Post-annealing of absorber layers in ambient air is further utilized to passivate the defects in Sb_2Se_3 and enhance the quality of the front heterojunction. After the proper annealing and optimization, our device performance improved from 7.4 to 8.5%.

We also worked on the $Sb_2(S, Se)_3$ solar cell in superstrate configuration. As, the bandgap of these materials can be tuned from 1.03 to 1.8 eV, depending on the S/Se ratio,

this could be another promising material for the photovoltaic material. In this work, we fabricate $Sb_2(S, Se)_3$ thin-film solar cells by a hydrothermal method followed by a post-deposition annealing process at different temperatures. We found that a proper annealing temperature leads to a high-quality $Sb_2(S, Se)_3$ film with large crystal grains, proper stoichiometry, and high crystallinity. After optimizing the process, we obtained $Sb_2(S, Se)_3$ solar cells with an improved power conversion efficiency from 2.04 to 8.48%.

6.2 Future Research on Sb_2Se_3

Although there is intensive research going on in Sb_2Se_3, still the efficiency is far behind the traditional established solar cell like Si, CdTe, and CIGS. The main limiting factor is lower Voc and FF. In Sb_2Se_3, V_{OC} is limited by many factors some of them are short carrier lifetime, low hole density, and large Urbach energy. Also, the FF is limited by low carrier mobility, deep defects, high resistance, pinholes e.t.c. The future work to improve the performance of Sb2Se3 solar cells is summarized below:

6.2.1 Technologies to Enhance the Efficiency of Sb_2Se_3 Solar Cells

While going through the development history of Sb_2Se_3 solar cells, we can find that the improvement of the efficiency has come through innovation in fabrication methods such as solution process, thermal evaporation, RTE, VTD, and CSS. That's why we believe we need to explore the new deposition and different treatment methods which could lead the efficiency to a high level. Lowering the interfacial recombination loss, proper light management, and controlling the band alignment with the proper device configuration

could help to boost the efficiency of the solar cell. Selenization is found to be one of the important methods to improve the film morphology which reduces the Se deficiency. Thus, the proper selenization technique with optimized temperature and the amount of Se could be one of the solutions to improve the performance of the device.

6.2.2 Improvement of V_{OC} and FF

It has been more than 10 years since the research on the Sb_2Se_3 has been started but the performance of the device is far behind the traditional solar cell like Si, and CdTe, and the limiting factors are V_{OC} and FF. High defect density and SbSe deep defects lead to a short carrier lifetime which is one of the factors limiting the V_{OC}. Also, low built-in potential and low crystallinity are other factors limiting the V_{OC}. Proper P-type doping could be one of the important solutions to improve the V_{OC} of the device. Low FF is due to the high resistance, and low quality of the film, which is due to the pinholes and void, and due to the low carrier mobility. Proper controlling of the orientation of the grain, proper selenization, and passivation of the interface and the surface helps to improve the FF.

6.2.3 Passivation of the Interface and Surface Defects

The defects present in the interface and surface are due to the presence of uncoordinated dangling bonds, interdiffusion, or lattice mismatching. The quality of interface and surface determine the performance of the solar cell. Through the C-V measurement, it has been found that the interfacial defects density of the Sb_2Se_3 solar cell without proper passivation is found to be around 10^{16} cm^{-3}. [102] It has been found that if there is no treatment on the Sb_2Se_3 thin film, the surface recombination rate on Sb_2Se_3 is

three times greater than the CdTe. [103] Much research has been done to solve the problems of interface and surface defects. Some of them are suppressing the Cd interdiffusion in the interface of CdS/Sb_2Se_3 by introducing ZnO [104], TiO_2[105], and SnO_2[106], band alignment has been studied to remove the cliff-like conduction band off at the interface of CdS/Sb_2Se_3 by annealing the Sb_2Se_3 absorber layer in an ambient [25], introducing Zn into CdS [107], and reducing the leakage current by introducing the double buffer layer like TiO_2/CdS[97], and CdS/ZnS[108]. Similarly, we can work on other materials as a buffer or interfacial layer that could be a suitable partner material for Sb_2Se_3.

6.3 Future Research on $Sb_2(S, Se)_3$

The following suggestions help to improve the performance of $Sb_2(S, Se)_3$ solar cells:

6.3.1 Film Preparation Methods and Device Configuration

The quality of the absorber layer highly determines the performance of solar cells. To get the absorber layer with high quality the gain should be highly crystalline, large size, compact and smooth morphology. Also, the deposition method highly impacts the quality of the absorber layer. Optimizing the deposition and post-annealing are found to be promising techniques to improve the performance of $Sb_2(S, Se)_3$ solar cells. Though the hydrothermal method has already delivered the PCE of 10.5% the films from the hydrothermal method are low crystalline and have some impurities related to oxides and carbon. So, Vacuum depositions may play a significant role to improve the $Sb_2(S, Se)_3$ solar cell performance.

6.3.2 Passivation of Defects

Defects in bulk or in interface highly determine the performance of the solar cell because defects are responsible for degrading the optical and electrical properties of the material. It has been noted that $Sb_2(S, Se)_3$ has higher defects concentration, lower carrier concentration, and lower lifetime as compared to other traditional well established solar cells which is the main cause of open-circuit voltage deficit. In this context, doping elements like Cu, Pb, Cl, and Sn could be useful to solve the problem.

6.3.3 Exploration of New Transport Layer

The mostly used ETL layer for the thin-film solar cell is CdS, however, this material is parasitic in nature in a blue region so replacing this layer could be any milestone for the solar cell. The diffusion of the Cd also leads to the unstability so alternatives seem to be much more beneficial. So, research on other ETL layers could help to improve the performance of $Sb_2(S, Se)_3$ solar cells.

Also, HTL is another important layer to determine the performance of $Sb_2(S, Se)_3$ solar cells. Research can be done on different HTL layers like PbS, P3HT, P3CT, Spiro-OMeTAD, and CuSCN to improve the performance.

References

1. Sadigov, R., *Rapid Growth of the World Population and Its Socioeconomic Results.* TheScientificWorldJournal, 2022. **2022**: p. 8110229-8110229.
2. EPA, *Global Greenhouse Gas Emissions Data*. 2022.
3. Lewis, N.S. and D.G. Nocera, *Powering the planet: Chemical challenges in solar energy utilization.* Proceedings of the National Academy of Sciences, 2006. **103**(43): p. 15729-15735.
4. Jones, D. *Global Electricity Review 2022*. 2022.
5. King, R.R., et al., *Solar cell generations over 40% efficiency.* Progress in Photovoltaics: Research and Applications, 2012. **20**(6): p. 801-815.
6. Becquerel, E., *On Electron Effects under the Influence of Solar Radiation.* Comptes Rendus de 'l' Academie Sciences Paris, 1839. **9**: p. 561.
7. Fraas, L.M., *History of Solar Cell Development*, in *Low-Cost Solar Electric Power*, L.M. Fraas, Editor. 2014, Springer International Publishing: Cham. p. 1-12.
8. Andreani, L.C., et al., *Silicon solar cells: toward the efficiency limits.* Advances in Physics: X, 2019. **4**(1): p. 1548305.
9. Rijal, S., et al., *Influence of Post-selenization Temperature on the Performance of Substrate-Type Sb2Se3 Solar Cells.* ACS Applied Energy Materials, 2021. **4**(5): p. 4313-4318.

10. Qarony, W., et al., *Efficient amorphous silicon solar cells: characterization, optimization, and optical loss analysis.* Results in Physics, 2017. **7**: p. 4287-4293.

11. Hart, D. and October, *The Impact of China's Production Surge on Innovation in the Global Solar Photovoltaics Industry*. 2020.

12. Conibeer, G., *Third-generation photovoltaics.* Materials Today, 2007. **10**(11): p. 42-50.

13. Yoo, J.J., et al., *Efficient perovskite solar cells via improved carrier management.* Nature, 2021. **590**(7847): p. 587-593.

14. Song, Z., et al., *Wide-bandgap, low-bandgap, and tandem perovskite solar cells.* Semiconductor Science and Technology, 2019. **34**(9): p. 093001.

15. Mavlonov, A., et al., *A review of Sb2Se3 photovoltaic absorber materials and thin-film solar cells.* Solar Energy, 2020. **201**: p. 227-246.

16. Dönges, E., *Über Chalkogenohalogenide des dreiwertigen Antimons und Wismuts. II. Über Selenohalogenide des dreiwertigen Antimons und Wismuts und über Antimon(III)-selenid Mit 2 Abbildungen.* Zeitschrift für anorganische und allgemeine Chemie, 1950. **263**(5-6): p. 280-291.

17. Jiajun, L., et al., *Mineralogy of the Stibnite-Antimonselite Series.* International Geology Review, 1999. **41**(11): p. 1042-1050.

18. Messina, S., M. Nair, and P. Nair, *Antimony selenide absorber thin films in all-chemically deposited solar cells.* Journal of The Electrochemical Society, 2009. **156**(5): p. H327-H332.

19. Zeng, K., D.-J. Xue, and J. Tang, *Antimony selenide thin-film solar cells.* Semiconductor Science and Technology, 2016. **31**(6): p. 063001.

20. Qiu, W., et al., *The crystal structure, electronic structure and photoelectric properties of a novel solar cells absorber material Sb2Se3−xSx.* Journal of Solid State Chemistry, 2019. **271**: p. 339-345.

21. Deringer, V.L., et al., *Vibrational properties and bonding nature of Sb 2 Se 3 and their implications for chalcogenide materials.* Chemical science, 2015. **6**(9): p. 5255-5262.

22. Huang, M., et al., *Complicated and Unconventional Defect Properties of the Quasi-One-Dimensional Photovoltaic Semiconductor Sb2Se3.* ACS Applied Materials & Interfaces, 2019. **11**(17): p. 15564-15572.

23. Li, K., et al., *Orientation Engineering in Low-Dimensional Crystal-Structural Materials via Seed Screening.* Advanced Materials, 2019. **31**(44): p. 1903914.

24. Rijal, S., et al. *Optimizing the Selenization of Sb2Se3 Absorbers to Improve the Film Quality and Solar Cell Performances*. in *2021 IEEE 48th Photovoltaic Specialists Conference (PVSC)*. 2021.

25. Rijal, S., et al., *Templated Growth and Passivation of Vertically Oriented Antimony Selenide Thin Films for High-Efficiency Solar Cells in Substrate Configuration.* Advanced Functional Materials, 2021. **32**(10): p. 2110032.

26. Liu, X., et al., *Thermal evaporation and characterization of Sb2Se3 thin film for substrate Sb2Se3/CdS solar cells.* ACS applied materials & interfaces, 2014. **6**(13): p. 10687-10695.

27. Duan, Z., et al., *Sb2Se3 Thin Film Solar Cells Exceeding 10% Power Conversion Efficiency Enabled by Injection Vapor Deposition (IVD) Technology.* Advanced Materials. **n/a**(n/a): p. 2202969.

28. Shockley, W. and H.J. Queisser, *Detailed Balance Limit of Efficiency of p-n Junction Solar Cells.* Journal of Applied Physics, 1961. **32**(3): p. 510-519.

29. Liu, X., et al., *Enhanced Sb2Se3 solar cell performance through theory-guided defect control.* Progress in Photovoltaics: Research and Applications, 2017. **25**(10): p. 861-870.

30. Shen, K., et al., *Efficient and Stable Planar n–i–p Sb2Se3 Solar Cells Enabled by Oriented 1D Trigonal Selenium Structures.* Advanced Science, 2020. **7**(16): p. 2001013.

31. Tang, R., et al., *Hydrothermal deposition of antimony selenosulfide thin films enables solar cells with 10% efficiency.* Nature Energy, 2020. **5**(8): p. 587-595.

32. Abegunde, O.O., et al., *Overview of thin film deposition techniques.* AIMS Materials Science, 2019. **6**(2): p. 174-199.

33. Li, D.-B., et al., *Stable and efficient CdS/Sb2Se3 solar cells prepared by scalable close space sublimation.* Nano Energy, 2018. **49**: p. 346-353.

34. Wen, X., et al., *Vapor transport deposition of antimony selenide thin film solar cells with 7.6% efficiency.* Nature communications, 2018. **9**(1): p. 2179.

35. Gao, C., et al., *Fabrication of Sb2S3 thin films by sputtering and post-annealing for solar cells.* Ceramics International, 2019. **45**(3): p. 3044-3051.

36. Chen, C., et al., *Optical properties of amorphous and polycrystalline Sb2Se3 thin films prepared by thermal evaporation.* Applied Physics Letters, 2015. **107**(4): p. 043905.

37. Ong, K.H., et al., *Review on Substrate and Molybdenum Back Contact in CIGS Thin Film Solar Cell.* International Journal of Photoenergy, 2018. **2018**: p. 9106269.

38. Li, D.-B., et al., *Stable and efficient CdS/Sb2Se3 solar cells prepared by scalable close space sublimation.* Nano Energy, 2018. **49**: p. 346-353.

39. Wang, W., et al., *Over 6% Certified Sb2(S,Se)3 Solar Cells Fabricated via In Situ Hydrothermal Growth and Postselenization.* Advanced Electronic Materials, 2019. **5**(2): p. 1800683.

40. Lindholm, F.A., J.G. Fossum, and E.L. Burgess, *Application of the superposition principle to solar-cell analysis.* IEEE Transactions on Electron Devices, 1979. **26**(3): p. 165-171.

41. Jayswal, N.K., et al., *Optical properties of thin film Sb2Se3 and identification of its electronic losses in photovoltaic devices.* Solar Energy, 2021. **228**: p. 38-44.

42. Jackson, P., et al., *Effects of heavy alkali elements in Cu (In, Ga) Se2 solar cells with efficiencies up to 22.6%.* physica status solidi (RRL)–Rapid Research Letters, 2016. **10**(8): p. 583-586.

43. NREL, N., *Best Research-Cell Efficiency Chart*. 2019, US Department of Energy.

44. Green, M., et al., *Solar cell efficiency tables (version 57).* Progress in Photovoltaics: Research and Applications, 2021. **29**(1): p. 3-15.

45. Zhang, C., J. Zhong, and J. Tang, *Cu2ZnSn(S,Se)4 thin film solar cells fabricated with benign solvents.* Frontiers of Optoelectronics, 2015. **8**(3): p. 252-268.

46. Kumar, M., et al., *Strategic review of secondary phases, defects and defect-complexes in kesterite CZTS–Se solar cells.* Energy & Environmental Science, 2015. **8**(11): p. 3134-3159.

47. Yun, H.-S., et al., *Efficient Nanostructured TiO2/SnS Heterojunction Solar Cells.* Advanced Energy Materials, 2019. **9**(35): p. 1901343.

48. Xue, D.-J., et al., *GeSe Thin-Film Solar Cells Fabricated by Self-Regulated Rapid Thermal Sublimation.* Journal of the American Chemical Society, 2017. **139**(2): p. 958-965.

49. Li, Z., et al., *9.2%-efficient core-shell structured antimony selenide nanorod array solar cells.* Nature Communications, 2019. **10**(1): p. 125.

50. Wang, X., et al., *Manipulating the Electrical Properties of Sb2(S,Se)3 Film for High-Efficiency Solar Cell.* Advanced Energy Materials, 2020. **10**(40): p. 2002341.

51. Lei, H.W., et al., *Review of Recent Progress in Antimony Chalcogenide-Based Solar Cells: Materials and Devices.* Solar Rrl, 2019. **3**(6): p. 1900026.

52. Liang, G., et al., *Ion doping simultaneously increased the carrier density and modified the conduction type of Sb2Se3 thin films towards quasi-homojunction solar cell.* Journal of Materiomics, 2021.

53. Ma, Y., et al., *Efficient defect passivation of Sb2Se3 film by tellurium doping for high performance solar cells.* Journal of Materials Chemistry A, 2020. **8**(14): p. 6510-6516.

54. Li, Z., et al., *Sb2Se3 thin film solar cells in substrate configuration and the back contact selenization.* Solar Energy Materials and Solar Cells, 2017. **161**: p. 190-196.

55. Leng, M., et al., *Selenization of Sb2Se3 absorber layer: an efficient step to improve device performance of CdS/Sb2Se3 solar cells.* Applied Physics Letters, 2014. **105**(8): p. 083905.

56. Liang, G.-X., et al., *Sputtered and selenized Sb2Se3 thin-film solar cells with open-circuit voltage exceeding 500 mV.* Nano Energy, 2020. **73**: p. 104806.

57. Luo, Y.-D., et al., *An effective combination reaction involved with sputtered and selenized Sb precursors for efficient Sb2Se3 thin film solar cells.* Chemical Engineering Jor., 2020. **393**.

58. Hultqvist, A., et al., *Performance of Cu(In,Ga)Se2 solar cells using nominally alkali free glass substrates with varying coefficient of thermal expansion.* Journal of Applied Physics, 2013. **114**(9): p. 094501.

59. Lide, D.R., *CRC handbook of chemistry and physics, 2003-2004*. 2003, Boca Raton: CRC Press.

60. Herrmann, M.G., et al., *Lattice Dynamics of Sb2Se3 from Inelastic Neutron and X-Ray Scattering.* physica status solidi (b), 2020. **257**(6): p. 2000063.

61. Guo, H., et al., *Enhancement in the Efficiency of Sb2Se3 Thin-Film Solar Cells by Increasing Carrier Concertation and Inducing Columnar Growth of the Grains (Solar RRL 3/2019).* Solar RRL, 2019. **3**(3): p. 1970033.

62. Zhou, Y., et al., *Thin-film Sb2Se3 photovoltaics with oriented one-dimensional ribbons and benign grain boundaries.* Nature Photonics, 2015. **9**(6): p. 409-415.

63. Tang, R., et al., *Highly efficient and stable planar heterojunction solar cell based on sputtered and post-selenized Sb2Se3 thin film.* Nano Energy, 2019. **64**: p. 103929.

64. Tang, R., et al., *Magnetron sputtering deposition and selenization of Sb2Se3 thin film for substrate Sb2Se3/CdS solar cells.* Surface and Coatings Technology, 2019. **360**: p. 68-72.

65. Sze, S.M., Y. Li, and K.K. Ng, *Physics of semiconductor devices*. 2021: John wiley & sons.

66. Luo, M., et al., *Thermal evaporation and characterization of superstrate CdS/Sb2Se3 solar cells.* Applied Physics Letters, 2014. **104**(17): p. 173904.

67. Tanaka, T., et al., *Existence and removal of Cu2Se second phase in coevaporated Cu2ZnSnSe4 thin films.* Journal of Applied Physics, 2012. **111**(5): p. 053522.

68. Xie, H., et al., *Formation and impact of secondary phases in Cu-poor Zn-rich Cu2ZnSn(S1−ySey)4 (0≤y≤1) based solar cells.* Solar Energy Materials and Solar Cells, 2015. **140**: p. 289-298.

69. Fleck, N., et al., *How Oxygen Exposure Improves the Back Contact and Performance of Antimony Selenide Solar Cells.* ACS Applied Materials & Interfaces, 2020. **12**(47): p. 52595-52602.

70. Liu, X., et al., *Improving the performance of Sb2Se3 thin film solar cells over 4% by controlled addition of oxygen during film deposition.* Progress in Photovoltaics: Research and Applications, 2015. **23**(12): p. 1828-1836.

71. Chen, C., et al., *Efficiency Improvement of Sb2Se3 Solar Cells via Grain Boundary Inversion.* ACS Energy Letters, 2018. **3**(10): p. 2335-2341.

72. Ou, C., et al., *Bandgap tunable CdS:O as efficient electron buffer layer for high-performance Sb2Se3 thin film solar cells.* Solar Energy Materials and Solar Cells, 2019. **194**: p. 47-53.

73. Li, G., et al., *Improvement in Sb2Se3 Solar Cell Efficiency through Band Alignment Engineering at the Buffer/Absorber Interface.* ACS Applied Materials & Interfaces, 2019. **11**(1): p. 828-834.

74. Hutter, O.S., et al., *6.6% efficient antimony selenide solar cells using grain structure control and an organic contact layer.* Solar Energy Materials and Solar Cells, 2018. **188**: p. 177-181.

75. Kondrotas, R., et al., *Growth mechanism of Sb2Se3 thin films for photovoltaic application by vapor transport deposition.* Solar Energy Materials and Solar Cells, 2019. **199**: p. 16-23.

76. Guo, L., et al., *Tunable Quasi-One-Dimensional Ribbon Enhanced Light Absorption in Sb2Se3 Thin-film Solar Cells Grown by Close-Space Sublimation.* Solar RRL, 2018. **2**(10): p. 1800128.

77. Tong, C.-J. and K.P. McKenna, *Passivating Grain Boundaries in Polycrystalline CdTe.* The Journal of Physical Chemistry C, 2019. **123**(39): p. 23882-23889.

78. Korevaar, B.A., et al., *Role of oxygen during CdTe growth for CdTe photovoltaic devices.* Progress in Photovoltaics: Research and Applications, 2014. **22**(10): p. 1040-1049.

79. Werner, F., et al., *Oxidation as Key Mechanism for Efficient Interface Passivation in $\mathrm{Cu}(\mathrm{In},\mathrm{Ga}){\mathrm{Se}}_{2}$ Thin-Film Solar Cells.* Physical Review Applied, 2020. **13**(5): p. 054004.

80. Cui, X., et al., *Cd-Free Cu2ZnSnS4 solar cell with an efficiency greater than 10% enabled by Al2O3 passivation layers.* Energy & Environmental Science, 2019. **12**(9): p. 2751-2764.

81. Guo, L., et al., *Interfacial engineering of oxygenated chemical bath–deposited CdS window layer for highly efficient Sb2Se3 thin-film solar cells.* Materials Today Physics, 2019. **10**: p. 100125.

82. Liang, G.-X., et al., *Thermally induced structural evolution and performance of Sb2Se3 films and nanorods prepared by an easy sputtering method.* Solar Energy Materials and Solar Cells, 2018. **174**: p. 263-270.

83. Guo, H., et al., *Highly efficient and thermally stable Sb2Se3 solar cells based on a hexagonal CdS buffer layer by environmentally friendly interface optimization.* Journal of Materials Chemistry C, 2020. **8**(48): p. 17194-17201.

84. Chen, S., et al., *Improved Open-Circuit Voltage of Sb2Se3 Thin-Film Solar Cells Via Interfacial Sulfur Diffusion-Induced Gradient Bandgap Engineering.* Solar RRL. **n/a**(n/a): p. 2100419.

85. Chen, C., et al., *Characterization of basic physical properties of Sb2Se3 and its relevance for photovoltaics.* Frontiers of Optoelectronics, 2017. **10**(1): p. 18-30.

86. Liang, X., et al., *Effect of deposition pressure on the properties of magnetron sputtering-deposited Sb2Se3 thin-film solar cells.* Applied Physics A, 2019. **125**(6): p. 381.

87. Burgelman, M., P. Nollet, and S. Degrave, *Modelling polycrystalline semiconductor solar cells.* Thin Solid Films, 2000. **361–362**: p. 527-532.

88. Basak, A. and U.P. Singh, *Numerical modelling and analysis of earth abundant Sb2S3 and Sb2Se3 based solar cells using SCAPS-1D.* Solar Energy Materials and Solar Cells, 2021. **230**: p. 111184.

89. Li, Z.-Q., M. Ni, and X.-D. Feng, *Simulation of the Sb2Se3 solar cell with a hole transport layer.* Materials Research Express, 2020. **7**(1): p. 016416.

90. Shiel, H., et al., *Natural Band Alignments and Band Offsets of Sb2Se3 Solar Cells.* ACS Applied Energy Materials, 2020. **3**(12): p. 11617-11626.

91. Li, J.V. and G. Ferrari. *Capacitance spectroscopy of semiconductors*. 2018.

92. Hobson, T.D.C., et al., *Defect properties of Sb2Se3 thin film solar cells and bulk crystals.* Applied Physics Letters, 2020. **116**(26): p. 261101.

93. Savory, Christopher N. and D.O. Scanlon, *The complex defect chemistry of antimony selenide*. Journal of Materials Chemistry A, 2019. **7**(17): p. 10739-10744.

94. Nakamura, M., et al., *Cd-free Cu (In, Ga)(Se, S) 2 thin-film solar cell with record efficiency of 23.35%.* IEEE Journal of Photovoltaics, 2019. **9**(6): p. 1863-1867.

95. Nkuissi, H.J.T., et al., *Toxic Materials used in thin film photovoltaics and their impacts on environment*, in *Reliability and Ecological Aspects of Photovoltaic Modules*. 2020, IntechOpen.

96. Zhou, Y., et al., *Solution-Processed Antimony Selenide Heterojunction Solar Cells.* Advanced Energy Materials, 2014. **4**(8): p. 1301846.

97. Wang, X., et al., *Interfacial engineering for high efficiency solution processed Sb2Se3 solar cells.* Solar Energy Materials and Solar Cells, 2019. **189**: p. 5-10.

98. Pan, Y., et al., *Vapor Transport Deposition of Highly Efficient Sb2 (S, Se) 3 Solar Cells via Controllable Orientation Growth.* Advanced Functional Materials, 2021: p. 2101476.

99. Calixto-Rodriguez, M., et al., *Antimony Chalcogenide/Lead Selenide Thin Film Solar Cell with 2.5% Conversion Efficiency Prepared by Chemical Deposition.* ECS Journal of Solid State Science and Technology, 2013. **2**(4): p. Q69-Q73.

100. Zhao, Y., et al., *Regulating Energy Band Alignment via Alkaline Metal Fluoride Assisted Solution Post-Treatment Enabling Sb2(S,Se)3 Solar Cells with 10.7% Efficiency*. Advanced Energy Materials. **n/a**(n/a): p. 2103015.

101. Sadewasser, S., *Surface potential of chalcopyrite films measured by KPFM.* physica status solidi (a), 2006. **203**(11): p. 2571-2580.

102. Liu, X., et al., *Thermal Evaporation and Characterization of Sb2Se3 Thin Film for Substrate Sb2Se3/CdS Solar Cells.* ACS Applied Materials & Interfaces, 2014. **6**(13): p. 10687-10695.

103. Chen, C. and J. Tang, *Open-Circuit Voltage Loss of Antimony Chalcogenide Solar Cells: Status, Origin, and Possible Solutions.* ACS Energy Letters, 2020. **5**(7): p. 2294-2304.

104. Wang, L., et al., *Stable 6%-efficient Sb 2 Se 3 solar cells with a ZnO buffer layer.* Nature Energy, 2017. **2**(4): p. 1-9.

105. Chen, C., et al., *Accelerated Optimization of TiO2/Sb2Se3 Thin Film Solar Cells by High-Throughput Combinatorial Approach.* Advanced Energy Materials, 2017. **7**(20): p. 1700866.

106. Lu, S., et al., *Sb2Se3 Thin-Film Photovoltaics Using Aqueous Solution Sprayed SnO2 as the Buffer Layer.* Advanced Electronic Materials, 2018. **4**(1): p. 1700329.

107. Chen, C., et al., *High-efficient Sb2Se3 solar cell using ZnxCd1-xS n-type layer.* Applied Physics Letters, 2021. **118**(17): p. 172103.

108. Mamta, K.K. Maurya, and V.N. Singh, *Enhancing the Performance of an Sb2Se3-Based Solar Cell by Dual Buffer Layer.* Sustainability, 2021. **13**(21): p. 12320.

Appendix A

Publication List

1. Rijal, S., et al., Influence of Post-selenization Temperature on the Performance of Substrate-Type Sb2Se3 Solar Cells. ACS Applied Energy Materials, 2021. 4(5): p. 4313-4318.
2. Rijal, S., et al., Templated Growth and Passivation of Vertically Oriented Antimony Selenide Thin Films for High-Efficiency Solar Cells in Substrate Configuration. Advanced Functional Materials, 2021. 32(10): p. 2110032.
3. Jayswal, N.K., et al., Optical properties of thin film Sb2Se3 and identification of its electronic losses in photovoltaic devices. Solar Energy, 2021. 228: p. 38-44.
4. Pokhrel, D., et al., Copper iodide nanoparticles as a hole transport layer to CdTe photovoltaics: 5.5 % efficient back-illuminated bifacial CdTe solar cells. Solar Energy Materials and Solar Cells, 2022. 235: p. 111451.
5. Bista, S.S., et al., Effects of Cu Precursor on the Performance of Efficient CdTe Solar Cells. ACS Applied Materials & Interfaces, 2021. 13(32): p. 38432-38440.
6. Subedi, K.K., et al., Semi-transparent p-type barium copper sulfide as a back contact interface layer for cadmium telluride solar cells. Solar Energy Materials and Solar Cells, 2020. 218: p. 110764.

7. Song, Z., et al., Assessing the true power of bifacial perovskite solar cells under concurrent bifacial illumination. Sustainable Energy & Fuels, 2021. 5(11): p. 2865-2870.

8. Bista, S.S., et al. Solution Processed CuCl treatment for efficient CdS/CdTe Solar Cells. in 2020 47th IEEE Photovoltaic Specialists Conference (PVSC). 2020.

9. Jamarkattel, M.K., et al., Improving CdSeTe Devices With a Back Buffer Layer of CuxAlOy. IEEE Journal of Photovoltaics, 2022. 12(1): p. 16-21.

10. Rijal, S., et al. Optimizing the Selenization of Sb2Se3 Absorbers to Improve the Film Quality and Solar Cell Performances. in 2021 IEEE 48th Photovoltaic Specialists Conference (PVSC). 2021.